DIFFERENTIAL TELLURICS

with applications to mineral exploration and crustal resistivity monitoring

by

Gerald Alan LaTorraca

S.B. Northeastern University (1965)
S.M. Massachusetts Institute of Technology (1972)

SUBMITTED TO THE DEPARTMENT OF
EARTH AND PLANETARY SCIENCES
IN PARTIAL FULFILLMENT
OF THE REQUIREMENTS
FOR THE DEGREE OF

DOCTOR OF PHILOSOPHY

at the

MASSACHUSETTS INSTITUTE OF TECHNOLOGY

September 1981

Signature of Author ______________________
Department of Earth and Planetary Sciences
September 25, 1981

Certified by ______________________
Theodore R. Madden
Thesis Supervisor

Accepted by ______________________
Theodore R. Madden
Chairman, Departmental Committee on Graduate Students

DIFFERENTIAL TELLURICS

with applications to mineral exploration and crustal resistivity monitoring

by

Gerald Alan LaTorraca

Submitted to the Department of Earth and
Planetary Sciences on September 25, 1981
in partial fulfillment of the requirements
for the degree of Doctor of Philosophy
in Geophysics

ABSTRACT

The intent of this thesis is to infer the fine structure of the telluric field from differential telluric measurements. From the frequency dependence of small scale differential measurements, we can infer the presence of induced polarization targets. From the stability of differential measurements, we can infer variations in the state of stress and strain in the crust and from the frequency dependence of large scale differential telluric measurements, we can infer the spatial variation of the thickness and apparent conductivity of the upper crust.

Tellurics are the electric fields induced in the earth by the large scale motions of charged particles outside the earth's atmosphere. The fine structure of the telluric field is contained in the tensor relationships between vector electric field measurements. To gain insights into the properties of these tensor relationships, we apply the shifted eigenvalue analysis of Lanczos(1961) to not only the telluric tensor but also to the associated impedance tensor relating magnetotelluric fields.

For the telluric tensor, the products of the eigenvalues and one set of electric field eigenvectors represent the maximum and minimum electric fields that can be produced by unit electric fields aligned with the second set of electric eigenvectors. Similarly, for the impedance tensor, the products of the eigenvalues and electric field eigenvectors represent the maximum and minimum electric fields that can be produced by unit magnetic fields. The magnetic eigenvectors represent the magnetic field geometry that yields the electric field extrema. The conventional skew is shown to be the tangent of the angular deviation of the electric and magnetic eigenvectors from perpendicular.

The sensitivity of differential telluric measurements to stress induced variations in crustal conductivity is studied. The stability of the telluric tensor parameters, eigenvalues and skew, are found, respectively, to be sensitive measures of the stability of the crustal conductivity and the effective anisotropy of the crustal conductivity. Additionally, the degree of telluric current saturation within the upper crust is found to be the most important factor in determining the sensitivities of differential telluric measurements.

The conductivity of an induced polarization target (ore body) varies with frequency relative to its surroundings. Low frequency (<10 second periods) differential telluric measurements are used to infer the relative frequency dependence of the telluric field outside and within the effective boundaries of the ore body. This relative frequency dependence is expressed in terms of telluric tensor eigenstates.

Thesis Supervisor: Prof. Theodore R. Madden

Title: Professor of Geophysics

ACKNOWLEDGEMENTS

During the past eleven years, I have been fortunate to make many friends in the Dept. of Earth and Planetary Sciences and I shall miss them all. I came to EPS to work for Gene Simmons. Gene has given me a great deal of trust and responsibility and has encouraged me to get my Phd. I thank him for his friendship, assistance and advice.

I worked for many years with Frank Miller. Frank has been a close and loyal friend as well as a continuing source of technical advice. I thank him for all the kindness and support he has shown me.

I wish to thank Larry Bannister, Bill Fairing, Dan Calileo, and Dick Baker of the Center for Space Research for their friendship and technical advice. Bob Stevens, Joe Walsh, George Keough, Dave Riach, Jock Hirst, and Jimmy Byrne have all been helpful and friendly to me and I thank them.

I wish to thank Debby Gillett for all her help over the past years and wish her well in her upcoming marriage to Steve Roecker.

I wish to thank the following professors in the department who have contributed greatly to my education in the geosciences: K. Aki, W. Brace, C. Burchfiel, J. Dickey, H. Fairbairn, S. Hart, W. Pinson, S. Solomon, and N. Toksoz.

My officemates and their spouses have taught me a great deal and I shall miss the give and take of ideas (plus the occasional argument) which have contributed so much to my education. My officemates in the order in which they left are: Rambabu Ranganayaki, Adolfo Figueroa-Vinas, Olu Agunloye, Dale Morgan, Frances Bagenal, and Earle Williams. Steve Park and John Williams are still here. To you all, my most heartfelt thanks. A special thank you goes to Earle Williams, Dale Morgan, Steve Park and Frances Bagenal for their assistance in my field studies in California and Massachusetts.

Many other graduate students have contributed to my education and the enjoyment of my stay at MIT. I wish to thank Steve Roecker, Mike Fehler , Brian Evans, Shamita Das, George Zandt, Tony Shakal, Gerardo Suarez, Karl Coyner, John Bartley, Alan Zindler, Hubert Staudigel, and Julie Morris.

I wish to thank Judy Stein, Shelley Rosenstein, Sara Brydges and Judy Roos for all their help and friendship through the years.

Pam and Stan Hart have been very kind to my wife Ana and me. Thanks to you both. I have spent many a Friday evening with Lynn and John Dickey at their home in Beacon Hill and I wish to thank them for their hospitality and friendship.

Ted Madden has been my advisor and friend since I returned to graduate school. Ted, his wife Halima and their children have extended their warm hospitality to me through the years and I shall miss them. Ted's influence on this thesis is considerable and I have used the editorial "we" throughout the thesis to reflect this influence. Ted has extended me further than I thought possible and I am very grateful for the education he has given me.

I wish to thank my parents, Beatrice and John LaTorraca, for their loyal support and encouragement. I wish to dedicate this thesis to them for all they have done for me.

I wish to thank my dearest friend and wife, Ana Silfer, for her support and encouragement during the writing of this thesis. Her patience and selflessness are deeply appreciated.

Financial aid from NASA the USGS and the department of Earth and Planetary Sciences has been accorded to me as a graduate student and I gratefully acknowledge this assistance.

TABLE OF CONTENTS

List of Figures

List of Tables

GLOSSARY OF TERMS AND ABBREVIATIONS

1D, 2D, 3D	the number of model dimensions along which the conductivity can vary
ρ	resistivity (ohm-meters)
σ	conductivity (ohm-meters)$^{-1}$
δ	can be either the skin depth or a variational depending upon context
λ	eigenvalue or, in the ellipsoid analysis, a dummy variable
Λ	eigenvalue matrix
e_i	electric field eigenvectors
h_i	magnetic field eigenvectors
U_i	eigenvector matrix
V_i	eigenvector matrix
$(\sim)$	complex conjugate transpose
$(*)$	conjugate
$(\ )^T$	transpose
J	current density (amps/m^2)
E	electric (telluric) field (volts/m)
H	magnetic field (amps/meter)
σ_{ij}	elements of conductivity tensor (ohm-meters)$^{-1}$
Z	impedance (ohms) or (mv/km/γ)
T	telluric tensor (mv/mv)
MT	magnetotellurics
H	time derivative of the magnetic field (amps/meter/sec)
Z	modified impedance (mv/km/γ/sec)
IP	induced polarization
DC	Direct Current (electrostatic)

CHAPTER 1

Introduction

1.0 History and development of magnetotellurics pertinent to this study

Cagniard (1953) initiated the study of magnetotellurics to the western world by showing that for the fluctuating component of the earth's electromagnetic field, ratios of the electric (telluric) to magnetic fields could be used to infer the electrical conductivity structure beneath the measurement system. Improvements in the understanding of the nature of the source-earth interaction along with the development of computational schemes necessary for the making magnetotellurics (MT) a practical geophysical tool have been published by Cantwell (1960), Madden and Nelson (1964), Sims and Bostick(1962), and Swift (1967) to name a few. With these studies, the earth's conductivity structure can be modelled as two dimensional, the impedance is recognized as requiring a tensor description and the calculation of the impedance elements is defined in terms of the coherencies between the electric and magnetic field measurements. Additionally, the tensor principal axis directions are defined in terms of a coordinate rotation which minimizes the diagonal terms of the impedance tensor.

Berdichevskii (1960) introduced to the geophysical literature the idea of using low frequency differential telluric measurements to infer the spatial variation of the conductivity thickness product or conductance of the upper crust. He modelled the telluric field as the response of the earth to a constant current source implicitly assuming that no resistive coupling of current exists between the upper crust and mantle.

Two more recent papers by Ranganayaki and Madden (1979) and Eggers(1981) have, respectively, extended our understanding of the effects of three dimensional structure on the magnetotelluric field and established the need for an eigenstate analysis of the impedance and telluric tensors. Ranganayaki and Madden (1979) have introduced a generalized thin sheet approach to model the earth's crust. In their studies they point out the effects of regional structure on the local, low frequency magnetotelluric field. They find that telluric currents leaking to and from the mantle at lateral changes in crustal conductivity cause distortions in the telluric field. The distance required for these distortions to diminish by 1/e is called the adjustment distance and is equal to the square root of the conductance of the upper crust times the resistivity thickness product of the lower crust. Two consequences of this result are that the telluric current system is not a constant current source on a large scale as Berdichevskii (1960) assumed and that to analyze low frequency MT data, the crustal model must be of dimensions much larger than the adjustment distance. As part of this thesis we seek to infer the sensitivity of differential telluric measurements to stress induced crustal conductivity variations. Accordingly, we need to use a realistic model of the magnetotelluric response which the generalized thin sheet analysis provides. The second recent paper pertinent to our studies involves a computational approach which improves our ability to discern fine structure in the telluric field.

Eggers (1981), in a paper submitted to Geophysics, has pointed out the incompleteness of the rotational approach to determine the principal axis directions of the impedance tensor and has suggested the use of a conventional eigenvalue approach to analyze the properties of the impedance tensor. Implicit in the conventional eigenvalue approach is the requirement that the tensor to be analyzed be Hermitian or symmetric for real tensors. Because the impedance and telluric tensors are only fortuitously Hermitian, we have elected to use the completely general approach of Lanczos (1961) to determine the eigenstates of both tensors. We feel that our eigenstate analysis is the next logical step in the computational development of the magnetotelluric and differential telluric techniques and should find widespread use. The eigenstate scheme is useful also for the inference of buried induced polarization (IP) targets from the fine structure of the telluric field.

1.1 Induced Polarization (IP) techniques

Induced Polarization is an electrical prospecting technique which uses the frequency dependence of the resistivity of rocks as an indicator of the presence of ore bearing minerals. The IP technique was first used extensively by the geophysical group of Newmont Exploration, Ltd. (Cantwell and Madden,1967) in the early 1950s. Presently, IP is an important tool in the prospecting for copper sulfide mineralization. In the application of the IP technique, active sources are used to measure the frequency dependence associated with the presence of ore bodies. The active source technique is limited by inductive coupling at frequencies greater than 10 Hz and by telluric noise for frequencies less than 0.1 Hertz. In order to find ore bodies deeper than tens of meters, attempts have been made to reduce the telluric noise (Halverson,1981) in the active measurements. Instead of removing the telluric fields, Madden (1979) suggested using the telluric field directly to infer the presence of buried IP targets. In this thesis, we consider the feasibility of Madden's hypothesis and develop techniques to implement IP prospecting with tellurics. We feel that the inference of IP targets with differential tellurics shows considerable promise for detecting deeper targets than can be inferred with active measurements and may also lead to the discrimination between minerals because of the extension of the frequency bandwidth to much lower periods than can be used with active measurements (Morgan ,1981).

1.2 Thesis content by chapter

In Chapter 2, we apply the shifted eigenvalue analysis of Lanczos (1961) to the impedance and telluric tensors. In Chapter 3, we present our analyses of the sensitivity of differential telluric measurements to stress induced variations in crustal conductivity. In Chapter 4, we present our studies of the use of differential telluric measurements to infer the presence of ore bodies and in Chapter 5, we describe our progress in determining large scale structure from differential telluric measurements, summarize our results and make suggestions for further study.

In Appendix A, we describe the field equipment and procedures used in our field studies. In Appendix B, we present a numerical example of the eigenstate procedures and establish the relationship between the conventional skew and the angle between the electric and magnetic eigenvectors. In Appendix C, we present an approximate technique for determining the low frequency impedance tensor and describe noise suppression techniques used in the analysis of bandlimited MT data. In Appendix D, we present our three dimensional model of an embedded IP target and in Appendix E, we describe procedures used to model the effective conductivity and stress sensitivity of crustal blocks used in the thin sheet analysis of Chapter 3.

Chapter 2

2.0 Introduction

Throughout this thesis we infer electrical properties of the earth's crust based on models of the interaction of the crust with the magnetotelluric field. The numerical expressions of the earth properties are the impedance and telluric tensors which relate respectively. the electric E to the magnetic H vector fields and spatially separated vector E fields. The fundamental properties of these tensors can be expressed in terms of tensor eigenstates: eigenvalues and eigenvectors. In this chapter, we formulate the eigenstates of the impedance and telluric and tensors using the shifted eigenvalue analysis of Lanczos (1961).

The concept of tensor eigenstates is the common thread through each part of the thesis. The eigenstates yield insights into the physical meaning of the tensor elements and allow the study of variations in the telluric tensor otherwise hidden.

2.1 The Eigenstates of the Impedance and Telluric Tensors

The magnetotelluric surface impedance, Z, is a tensor which relates the horizontal magnetic and electric fields at the earth's surface. The telluric tensor T is formulated to relate the horizontal electric field components. Normally tensors are defined at a point. However, electric field measurements require electrode separations from the order of one kilometer for local measurements to tens of kilometers for large scale measurements such as Madden's resistivity monitoring arrays near Hollister and Palmdale, Ca. Kasameyer(1974) and Swift(1967) have analyzed the difficulties in applying tensor analysis to impedances obtained using long line telluric data. Swift(1967) showed that if the lines were not spanning both sides of a two dimensional contact, the impedance could be treated as a tensor. Kasameyer (1974) analyzed separately the rows of the impedance associated with each telluric line when each line covered diferent structures. He then used the Z estimates associated with one line to constrain the estimates associated with the other. Both authors used two dimensional modelling techniques to analyze their data but pointed out that the approximation of considering long line telluric fields as point measures can lead to full tensors in 2D structures even when the impedance tensor has been rotated to its principal axes. In this chapter we shall consider the eigenstates of the impedance and telluric tensors with the realization that our use of the term tensor is an extension of its normal use. In Chapter 3 we shall consider the effects of this tensor assumption on our interpretation of long line telluric data. Because of the direct relation between the magnetotelluric and telluric tensors, let us consider first the eigenstates of the impedance tensor. Later we shall extend these eigenstate concepts to the telluric tensor.

For a model of the earth in which the conductivity varies only as a function of depth, the 1D model, the impedance degenerates to a simple scalar. For the model of a 2D earth for which conductivity varies with depth and one lateral direction, the impedance tensor is reduced to two off diagonal elements representing the impedance parallel and perpendicular to the strike direction along which the conductivity is constant. In geologically homogeneous areas and at frequencies greater than about 1 Hertz, one or two dimensional models of the earth often are sufficient to infer geologic structure from estimates of the impedance tensor. However, at lower frequencies and in geologically heterogeneous regions, three dimensional modelling of magnetotelluric data is necessary. Additionally, Eggers(1981) has pointed out the need for a more general approach to the analysis of the impedance tensor Z by showing that the 2D rotational approach produces ambiguous principal axes and apparent resistivities because much of the information in the impedance tensor is ignored. Specifically, Eggers(1981) notes that the rotationally defined apparent resistivities are insensitive to the addition of an abitrary constant along the diagonal of Z and that the conventional parameter set is incomplete. A more general analysis of the impedance tensor can be accomplished by application of the "shifted eigenvalue" analysis of Lanczos(1961), as suggested by Swift(1967). Eggers(1981), however, was the first to actually apply eigenstate analysis to the impedance tensor. Eggers' paper has not yet been published and may be changed. Presently, he is using a conventional eigenstate analysis which is a valid approach for Hermitian matrices but can lead to defective matrices when applied to non Hermitian matrices. The impedance tensor is rarely Hermitian. Accordingly, we shall follow Eggers' idea of using eigenstate analysis but shall use the shifted eigenvalue approach of Lanczos(1961) which is completely general and can be applied to all matrices.

In the frequency domain, the impedance tensor Z is a complex, non Hermitian matrix relating the horizontal electric and magnetic fields on the earth's surface such that:

$$E = Z H \tag{2-1}$$

The tensor itself is found from statistical averages of fields measured in a specific coordinate system e.g. X and Y and can be written as:

$$Z = \begin{bmatrix} Zxx & Zxy \\ Zyx & Zyy \end{bmatrix} \qquad (2\text{-}2)$$

Because Z is non Hermitian, it is also not self adjoint i.e.

$$\tilde{Z} \neq Z \qquad (2\text{-}3)$$

where the tilde represents complex conjugate transpose. To find the eigenstates of a non Hermitian matrix such as Z, Lanczos suggests the use of the augmented matrix form:

$$S = \begin{bmatrix} 0 & Z \\ \tilde{Z} & 0 \end{bmatrix} \qquad (2\text{-}4)$$

where S is a Hermitian matrix whose principal axis transformation can be found through the eigenvalue equation:

$$S\,w = \lambda\,w \qquad (2\text{-}5)$$

where (λ) is a real eigenvalue of S and w is the corresponding eigenvector. Consistent with equation 4, the augmented eigenvector w consists of two eigenvectors for each eigenvalue. We designate the electric field eigenvector as (u) and the magnetic field eigenvector as (v). Then, (w) can be written as:

$$w = \begin{bmatrix} u \\ \\ v \end{bmatrix} \qquad (2\text{-}6)$$

with (u) an eigenvector in the column space of Z and (v) an eigenvector in the row space of Z. From 4 and 5 we note that:

$$\begin{aligned} Z\ v &= \lambda\ u \\ \tilde{Z}\ u &= \lambda\ v \end{aligned} \qquad (2\text{-}7)$$

Multiplying both sides of 7 respectively by $\tilde{Z}$ and Z we find

$$\begin{aligned} \tilde{Z}\ Z\ v &= \lambda^2\ v \\ Z\ \tilde{Z}\ u &= \lambda^2 u \end{aligned} \qquad (2\text{-}8)$$

Thus, the (u) and (v) eigenvectors can be found independently. Arranging, the normalized (u) and (v) as columns in the matrices U and V and the eigenvalues as elements of the diagonal matrix (Λ) we can expand 7 to:

$$\begin{aligned} Z\ V = U\Lambda &= \begin{bmatrix} u_1 & u_2 \\ \\ \cdot & \cdot \end{bmatrix} \begin{bmatrix} \lambda_1 & \\ \\ & \lambda_2 \end{bmatrix} \\ \tilde{Z}\ U = V\Lambda &= \begin{bmatrix} v_1 & v_2 \\ \\ \cdot & \cdot \end{bmatrix} \begin{bmatrix} \lambda_1 & \\ \\ & \lambda_2 \end{bmatrix} \end{aligned} \qquad (2\text{-}9)$$

As shown in Appendix B, the two (u) eigenvectors are normalized and orthogonal as are the (v) eigenvectors. These eigenvectors form complete sets. Accordingly:

$$V \tilde{V} = I \qquad (2\text{-}10)$$

Combining 9 and 10, the formal eigenstructure of Z is:

$$Z = U \Lambda \tilde{V} = \begin{bmatrix} u_1 & u_2 \\ & \\ \cdot & \cdot \end{bmatrix} \begin{bmatrix} \lambda_1 & \\ & \\ & \lambda_2 \end{bmatrix} \begin{bmatrix} v_1^* & \cdot \\ & \\ v_2^* & \cdot \end{bmatrix} \qquad (2\text{-}11)$$

One problem not addressed explicitly by Lanczos is how the phases of complex tensors such as Z are assigned in the eigenstate formulation. This phase problem arises because the u and v eigenvectors in equation 6 are not truly independent. The phase constraints that exist between u and v are lost when we decouple the eigenvectors in equation 8. To complete this analysis, we could use the results of equation 8 in equation 7 to find the phases between the u and v eigenvectors as suggested implicitly by Aki and Richards (1980). However, such an approach would still require a set of conventions for assigning these phases to the eigenvectors. Alternatively, we suggest assigning the phases between the u and v eigenvectors to the eigenvalues. The resultant eigenstructure has the natural separation of the magnitude and phase of the impedance from the principal axis and polarization ellipticity information in the eigenvectors.

Allowing the eigenvalues to be complex requires a simple modification of the Lanczos analysis. Equation 5 is modified to:

$$S\ w = \begin{bmatrix} \lambda & \\ & \lambda^* \end{bmatrix} w \qquad (2\text{-}12)$$

where (*) denotes complex conjugate. As before the u and v eigenvectors must obey the orthogonality condition described in Appendix B. With complex eigenvalues, equation 7 becomes:

$$\begin{aligned} Z\ v &= \lambda u \\ \tilde{Z}\ u &= \lambda^* v \end{aligned} \qquad (2\text{-}13)$$

and, consequently. equation 8 is changed to:

$$\begin{aligned} \tilde{Z}\ Z\ v &= |\lambda|^2\ v \\ Z\ \tilde{Z}\ u &= |\lambda|^2\ u \end{aligned} \qquad (2\text{-}14)$$

With equations 12 and 13, we can assign phase to the eigenvalues retaining ellipticity information in the eigenvectors. We wish also to make the phases of these eigenvalues functions only of the earth properties and invariant to coordinate transformation. To this end we phase shift the eigenvectors calculated from equation 14 so that at t=0 each eigenvector is at the peak of its polarization ellipse. The four eigenvectors then are defined in terms of four points in space and one point in time. Coordinate transformations change neither the relative positions of these points nor the phase differences between them. With these phase shifted eigenvectors, the phases of the eigenvalues are calculated with either equation 11 or 13. The eigenvalue phases reflect the phase difference between the (u) and (v) eigenvectors at their respective peak magnitudes and are ,therefore, invariant to coordinate transformation as well. Additionally, with this modified eigenstate formulation we can infer three dimensional measures of structure from the eigenvectors.

In general, we can expect the electric field eigenvectors to be controlled by local structures and the magnetic field eigenvectors controlled both by local and regional structures. In our theoretical 3D modelling in Chapter 3, we find that current funnelling parallel to the coastline causes the near coast magnetic eigenvectors to be aligned perpendicular and parallel to the coastline but further inland the magnetic eigenvectors return to local control and near perpendicular relationships with the electric field eigenvectors.

For a 2D earth model, the electric and magnetic eigenvectors are linearly polarized and each electric eigenvector (u_λ) is perpendicular to its magnetic counterpart (v_λ). Accordingly, the ellipticities of the individual eigenvectors and the skew or deviation from perpendicularity of the electric and magnetic eigenvector directions are 3D measures of structure.

This eigenstate formalism is consistent with the notion that resistivity structures can cause the deviation of current away from the normal to the magnetic field. From the known extremum properties of these eigenvectors (Lanczos, 1961), we can interpret the electric eigenvectors as the maximum and minimum electric fields possible for a unit magnetic field and the magnetic eigenvectors as the magnetic field geometry that yields the electric field extrema.

The calculation of skew and its relationship with the conventional skew is included in Appendix B. Additionally. ellipticity and the conventions necessary for the asignments of signs and ellipticity phases to individual eigenvectors are included in Appendix B along with a numerical example of the eigenstate procedures. The algebraic formalism of the eigenstates in terms of the elements of Z are included in Appendix B as well. Further applications can be found in Chapter 3 for the crustal thin sheet analysis near Hollister and Palmdale, California as well as in Appendix C where the analysis of MT field data from Palmdale is described. Now let us extend the shifted eigenvalue analysis to the study of telluric tensors.

2.2 Telluric Tensors

The telluric tensor T is formulated in the frequency domain to relate two electric fields either from a single region or from separate regions. T is a function of the geologic structure beneath both E field measurements. The form of T can be induced from the impedance tensor. For a vector set of E,H measurements:

$$E_1 = Z_1 H_1 \qquad (2\text{-}15)$$

and for a second vector set:

$$E_2 = Z_2 H_2 \qquad (2\text{-}16)$$

The magnetic fields (H_1) and (H_2) can be related by a tensor which reflects the spatial variation of the horizontal magnetic field due to structurally induced current channelling and finite source wavelengths. The form of this relationship is:

$$H_1 = T_H H_2 \qquad (2\text{-}17)$$

Babour et al.(1976), and Swift(1967) have shown that at low frequencies and middle latitudes, the regional magnetic field tends to be a slowly varying function of position. Thus, for moderate measurement site separations, (T_H) is essentially diagonal and nearly equal to the identity matrix. The telluric tensor equation relating (E_1) and (E_2), then can be written in the form:

$$E_1 = Z_1 T_H^{-1} Z_2^{-1} E_2 = T E_2 \qquad (2\text{-}18)$$

Z_1 and Z_2 are functions of the regional and local properties of the earth. To gain further insights into the nature of the telluric tensor T let us use the eigenstate form of the impedances (Z_1) and (Z_2) in equation 15 with:

$$Z_1 = U_M^1 \Lambda_M^1 \tilde{V}_M^1$$

$$(2\text{-}19)$$

$$Z_2 = U_M^2 \Lambda_M^2 \tilde{V}_M^2$$

where (U_M^i) is the E field eigenvector matrix, (Λ_M^i) is the eigenvalue matrix and (V_M^i) is the H field eigenvector matrix. Here the subscript M designates magnetotelluric eigenstates. With equation 19, we can expand equation 15 to the form:

$$E_1 = U_M^1 \Lambda_M^1 \tilde{V}_M^1 T_H^{-1} V_M^2 (\Lambda_M^2)^{-1} \tilde{U}_M^2 E_2 \qquad (2\text{-}20)$$

When the magnetic field and magnetic eigenvectors do not vary with position, the eigenstates of the telluric tensor become:

$$T = U_M^1 \Lambda_M^1 (\Lambda_M^2)^{-1} \tilde{U}_M^2 \qquad (2\text{-}21)$$

with:

$$\tilde{V}_M^1 \, T_H^{-1} \, V_M^2 = I \qquad (2\text{-}22)$$

where I is the identity matrix. Additionally, when the maximum and minimum resistivity directions correspond to the directions of maximum and minimum contrast in resistivity:

$$U_T^1 = U_M^1 \qquad (2\text{-}23)$$

and

$$U_T^2 = U_M^2 \qquad (2\text{-}24)$$

and the telluric eigenvalues are related to the ratio of their magnetotelluric counterparts such that:

$$\Lambda_T = \Lambda_M^1 \left(\Lambda_M^2\right)^{-1} \qquad (2\text{-}25)$$

The telluric tensor eigenstates are expressed as:

$$T = U_T^1 \Lambda_T \tilde{U}_T^2 \qquad (2\text{-}26)$$

where the subscript T is used to designate telluric eigenstates. This eigenvector correspondence is true for two dimensional structures within which the horizontal magnetic field does not vary. For such structures, the eigenvalues of (Λ_T) are ratios of impedances and the eigenvectors at one position are orthogonal to each other and parallel to their counterparts at another position. Additionally, the 2D eigenvectors will be aligned perpendicular and parallel to the strike direction, i.e. along the directions of maximum and minimum impedance contrast. Correspondence can also occur when the direction of the maximum change in resistivity is aligned with the maximum resistivity direction. Such cases are locally two dimensional but can exhibit small skews. However, for more complicated structures, the magnetic eigenvectors can vary with position and the electric eigenvectors of the magnetotelluric and telluric tensors need no longer be in one to one correspondence.

The spatial variation of the magnetotelluric eigenvectors can be seen in our theoretical modelling of the eigenstates of the impedance tensor in Chapter 3. Impedance tensors and their eigenstates were calculated for points within an area of 270 kilometers squared centered near Palmdale, CA. For the tensor calculations we used the generalized thin sheet approach, a quasi 3D analysis, devised by Ranganayaki and Madden (1979). Within this geologically complicated region, the magnetic eigenvectors tend to vary with position along with the electric eigenvectors but when current funnelling occurred the magnetic eigenvectors did not vary spatially and the telluric eigenvectors corresponded locally to their magnetotelluric counterparts.

In the following chapters, we apply this eigenstate analysis to infer the sensitivity of telluric tensors to variations in crustal conductivity and to infer the presence of induced polarization targets based on the frequency dependence of the telluric tensor eigenstates.

CHAPTER 3

The Sensitivity of Telluric Field Measurements to Stress

3.0 Introduction

3.0.0 History and overview of resistivity monitoring with tellurics

Since 1972, Prof. Madden of MIT has been investigating means of predicting earthquakes using changes in the electrical properties as precursors. From these studies, Madden has devised a technique for monitoring resistivity in the crust based on the stability of the tensor relationships between telluric field measurements. Currently, he has two arrays of telluric measurement dipoles operating on a continuous basis. One array is centered in the Hollister area of central California where the San Andreas and Calaveras Faults merge as shown Figure 3.1. The second array is centered on the San Andreas Fault near Palmdale in southern California as depicted in Figure 3.2.

In this chapter, our primary goal is to investigate the sensitivity of telluric array measurements to changes in crustal conductivity due to stress. Specifically, we shall infer an approximate three dimensional model of the conductivity structure near Palmdale, calculate the magnetotelluric response to this model and relate the telluric field tensors calculated

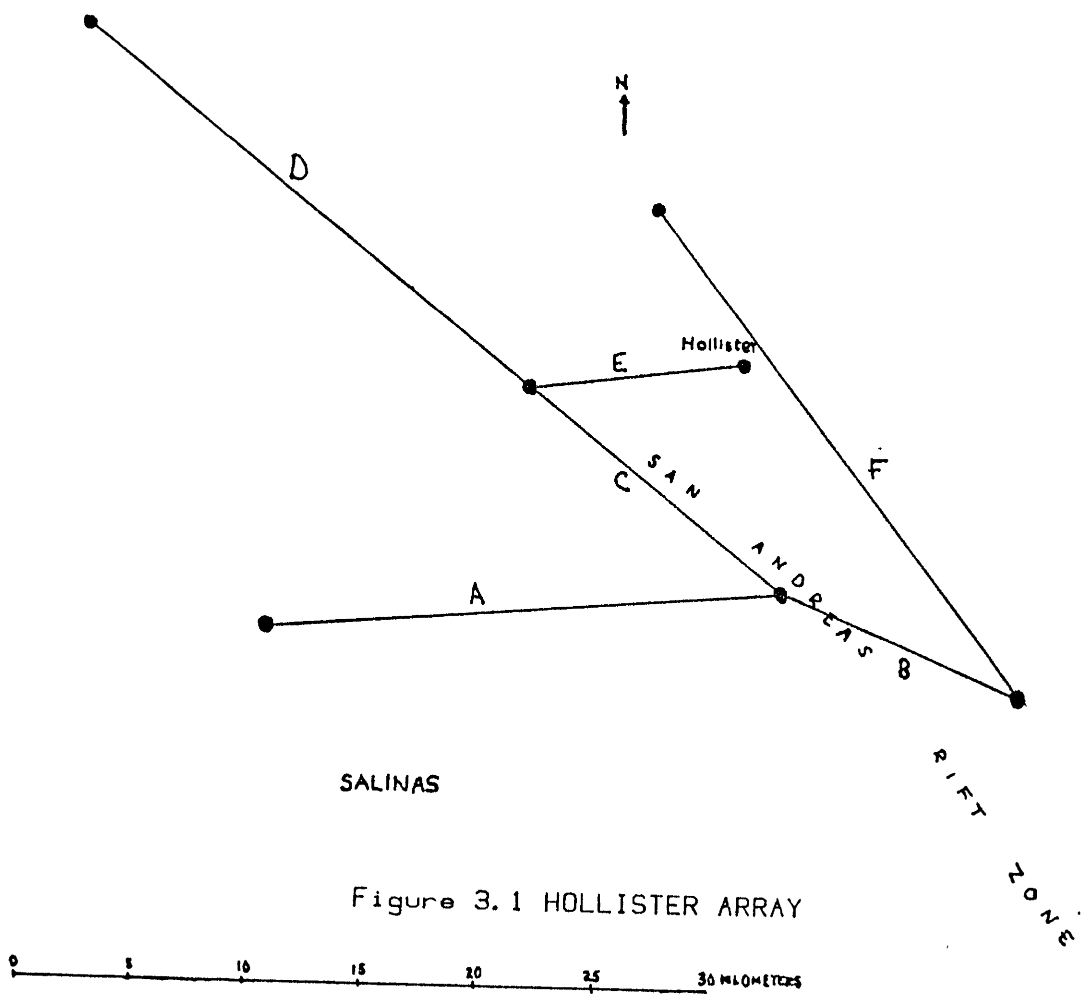

Figure 3.1 HOLLISTER ARRAY

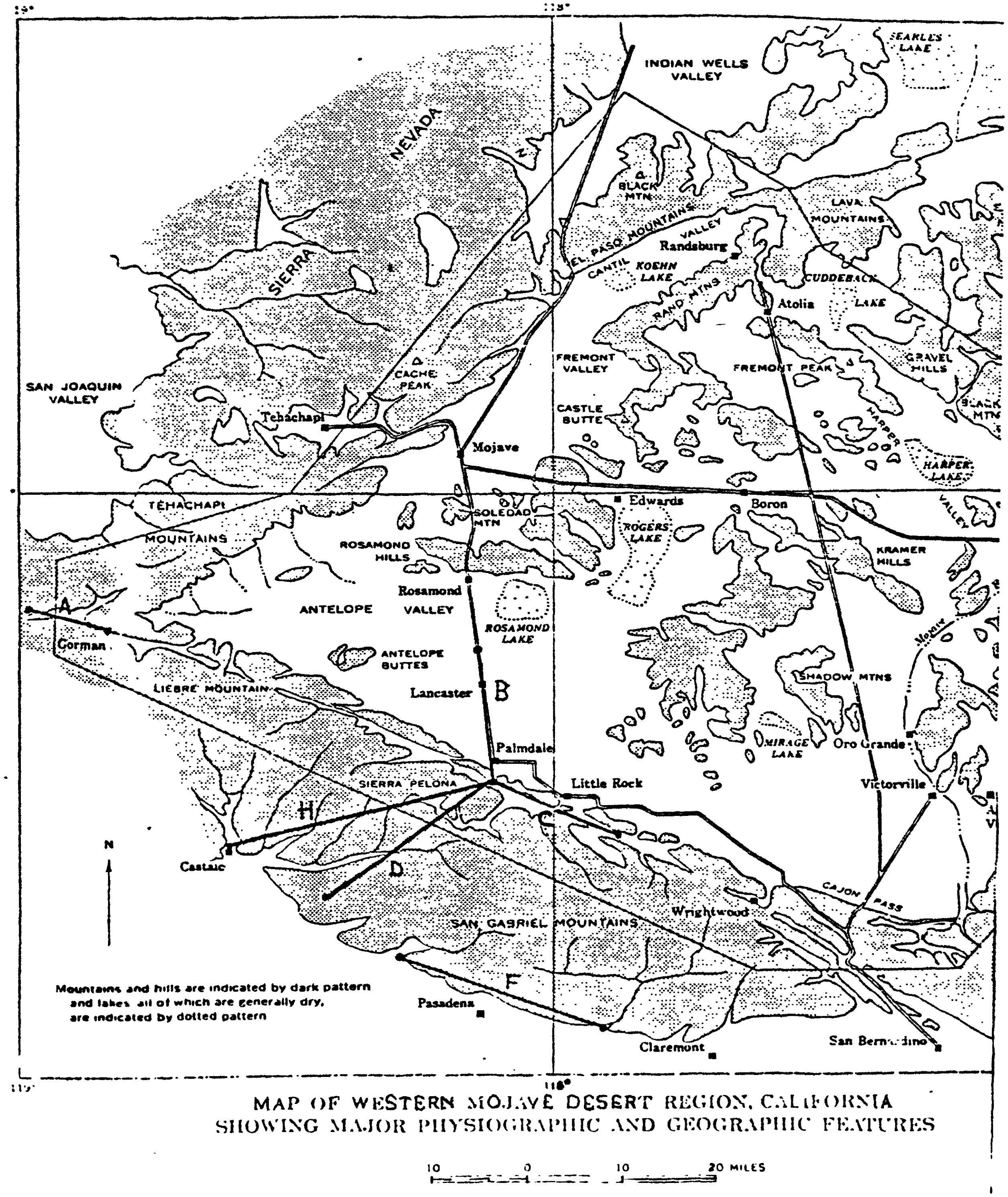

FIGURE 3.2 Palmdale Array.

from this response to the tensor relationships between the dipole signals of Madden's array. Perturbations in crustal conductivity due to stress, then, can be seen as variations in the telluric tensor relationships.

3.0.1 Chapter content

In sections 3.1 and 3.2, we review briefly the electrical properties of rocks and Madden's (1978) model of the stress and strain sensitivities of fault zones. The implications of Madden's model are that small temporal variations in electrical properties can be expected as precursors to earthquakes and very precise measurements are needed to monitor changes in crustal conductivity. In Section 3.2, we describe how Madden has used the high coherency of the telluric field to produce precise measures of the stability of the telluric tensor relationships between dipole measurements. Additionally, we shall relate the nature of the telluric field response near Palmdale to the eigenstate analysis of Chapter 2.

To infer a realistic stress sensitivity for Madden's array near Palmdale, we must use a conductivity model of the crust which incorporates the major features of the regional and local geology. The magnetotelluric response of simpler geological models (e.g. a two dimensional earth model) would not reflect properly the control of the telluric current system by regional features (Ranganayaki and Madden,1979). The generalized thin sheet approach of Ranganayaki and Madden (1979) not only reflects the regional control of the telluric current system but also yields an approximate measure of the magnetotelluric response to a three dimensional model of the earth. Consequently, in Sections 3.3 and 3.4, we describe and apply the thin sheet analysis to infer the magnetotelluric response of a large area (270km by 270km) of southern California centered near Palmdale.

In order to determine the sensitivity of the Palmdale array to stress related changes in crustal conductivity, in Section 3.5 we perturb the conductivity of crustal blocks within our numerical grid and infer the sensitivities of the telluric response in terms of tensor eigenstates. Finally, in Section 3.6, we relate the eigenstate sensitivities for our crustal model to Madden's Palmdale array measurements and reach conclusions about the efficacy of using telluric measurements to infer variations in the state of stress in the earth's crust. Sections 3.1-3.5 contain detailed descriptions of the techniques and constraints placed on our model. I suggest passing over these sections in the initial reading of the chapter and using 3.1-3.5 as a reference for Section 3.6.

3.1 Electrical Properties of rocks under stress

3.1.0 Content

In this section, we describe briefly, the mechanisms which control the electrical properties of upper crustal rocks. This section is included for the purposes of providing background for the rest of the chapter and to show why small changes are expected in crustal conductivity between earthquakes. Most of the information in this section can be found in greater detail in the paper of Madden(1978).

3.1.1 Electrical Conductivity Mechanisms

The conductivity of upper crustal rocks is controlled largely by the pore fluid salinity and the volume and geometry of interconnected pores and cracks. In terms of their electrical and mechanical properties, crustal rocks can be classified in three groups (Madden,1978): igneous and metamorphic, sedimentary and fault zone rocks. Because little is known about the properties of fault rocks, we shall assume that fault rock properties can be inferred from studies on sedimentary and igneous and metamorphic rocks.

The bulk conductivity of sedimentary rocks can be described by Archie's law:

$$\sigma_{rock} = \sigma_{fluid} \, (porosity)^2 \qquad (3\text{-}1)$$

The conductivity of igneous and metamorphic rocks is controlled by crack sizes and geometry. For small cracks and pores less than .01 micron across, conduction on the crack surfaces becomes the controlling factor for the conductivity. This surface conduction is due to an excess of ions attracted electrostatically to the crack surface where a net charge exists on the mineral surfaces. The potential caused by this charge is called the zeta potential which is typically -50 to -70 mv for silicate minerals at room temperature (MIT, 12.52 course notes, 1974).

The effect of the geometry of pores and cracks on the conductivity is not well established. However, from numerical studies using embedded networks to model cracks and pores, Madden (1974) has found that narrow cracks have an influence on the rock conductivity far in excess of their contribution to the total pore volume. Because narrow cracks are the most easily deformed, we can expect rocks to be sensitive to strain.

3.1.2 Conductivity: Stress-Strain Relationships

With the use of laboratory data, collected largely by Brace and coworkers, Madden(1978) has shown that the sensitivity of crustal rocks to stress and strain depends on the extent that cracks control the conductivity. High porosity sedimentary rocks have been shown to exhibit little stress sensitivity while igneous and metamorphic rocks have been shown to exhibit higher sensitivities. Additionally, Madden has inferred that stress-strain sensitivities tend to decrease with increasing confining stress but exhibit a reversal of this trend at the onset of dilatancy. Based on these findings and the assumption that cracks control the electrical properties of fault rocks, Madden(1978) proposed the crustal sensitivity models presented as Table 3.1. The amplification factors are the changes in resistivity per microstrain and the stress changes are in percentage change of resistivity per bar of deviatoric stress.

Earthquakes along the San Andreas system tend to occur at depths of 3 to 12 kilometers. Applying his model to the San Andreas, Madden predicted changes in conductivity per bar of .03 to .1% and amplification factors of 80 to 150 for effective porosities of 3%. From these sensitivity estimates and the assumption of 1 bar/year stress change, Madden (1978) concluded that conductivity changes of .03 to .1% per year can be expected in active fault zones. However, he argued further that crustal heterogeneities could cause unequal stress distributions resulting in accelerated local variations of up to 1% prior to earthquakes.

Perhaps the most important conclusions to be drawn from Madden's studies are that only small changes in crustal conductivity can be expected as precursors of impending earthquakes and that any electrical properties monitoring system must be capable of very precise and stable measurements. In the next section, we describe how Madden uses telluric cancellations to achieve the high

Table 3.1

Estimated Resistivity: Stress-Strain Relationships

Amplification Factor $(\Delta\rho/\rho)/\Delta\mu$

Porosity in %		1	3	10	30	
Depth, km	0	500	100	20	7	
	1	400	100	20	7	non-dilatant strain region
	3	300	80	20	7	
	10	200	60	20		
	0	750	200	30	10	
	1	500	200	30	8	
	3	400	150	25	7	dilatant strain region
	10	300	100	20		

Stress Sensitivity $\%\Delta\rho$/bar

Porosity in %		1	3	10	30	
Depth, km	0	.4	.3	.04	.02	
	1	.2	.15	.04	.02	non-dilatant strain region
	3	.07	.10	.03	.02	
	10	.03	.03	.02		
	0	.5	.4	.1	.03	
	1	.3	.2	.1	.03	
	3	.1	.10	.05	.03	dilatant strain region
	10	.05	.05	.03		

(from Madden, 1978)

sensitivities necessary to monitor the state of stress and strain in the crust.

3.2 Telluric Cancellations

3.2.0 Nature of the low frequency telluric field

The elements of the telluric field relating electric fields at the surface of the earth are generally frequency dependent. However, at low frequencies, the telluric currents are trapped in the conductive upper crust by the resistive lower crust (Ranganayaki and Madden,1979) and negligible phase shift exists between telluric fluctuations for which the skin depth is much larger than the upper crustal thickness. Source wavelengths tend also to be very large producing negligible phase shifts between telluric measurements separated by as much as 400 kilometers as indicated by the high coherency (>.999) between simultaneous measurements from the Palmdale and Hollister arrays (Madden, Personal Communication,1980).

3.2.1 Electronic determination of telluric tensor relationships

Consistent with these observations, three telluric field measurements are related accurately by real constants such that:

$$A \cong bB + cC \qquad (3\text{-}2)$$

These components can be combined electronically over a wide bandwidth of low frequencies to produce a near null or residual signal R such that:

$$R = A - bB - cC \qquad (3\text{-}3)$$

This process of producing residuals from two or more telluric measurements is called telluric cancellations (Madden,1976). The residual signal R can be amplified and its content studied with greater sensitivity than similar studies of the individual dipole signals for a given digitization accuracy. The constants b and c are measures of the integrated crustal conductivity under the telluric measurements. The stability of these constants then can be used as a measure of the temporal variation of the crustal conductivity (Madden,1978). Recordings of these signals over a 5 day period are included as Figure 3.3. H represents a single dipole signal. S_{B1} and S_{B2} represent scalar cancellation residuals and their gain relative to H is shown on the graph. The remaining signals represent tensor cancellations and their gains relative to H are listed as well. Dipoles A and F have pre-gains of 11 and 6 respectively.

3.2.2 Hollister and Palmdale array measurements

To implement the telluric cancellation scheme, Madden uses telephone lines to connect distant electrodes to central stations in Hollister and Palmdale, California (Figures 3.1,3.2). Combining three or four dipole signals at a time, he has produced and recorded sets of residuals R_i. These residuals reflect the incompleteness of the cancellations. To relate the residuals R_i to the stability of the tensor elements, two independent signals S_A and S_B with which any of the dipole signals can be

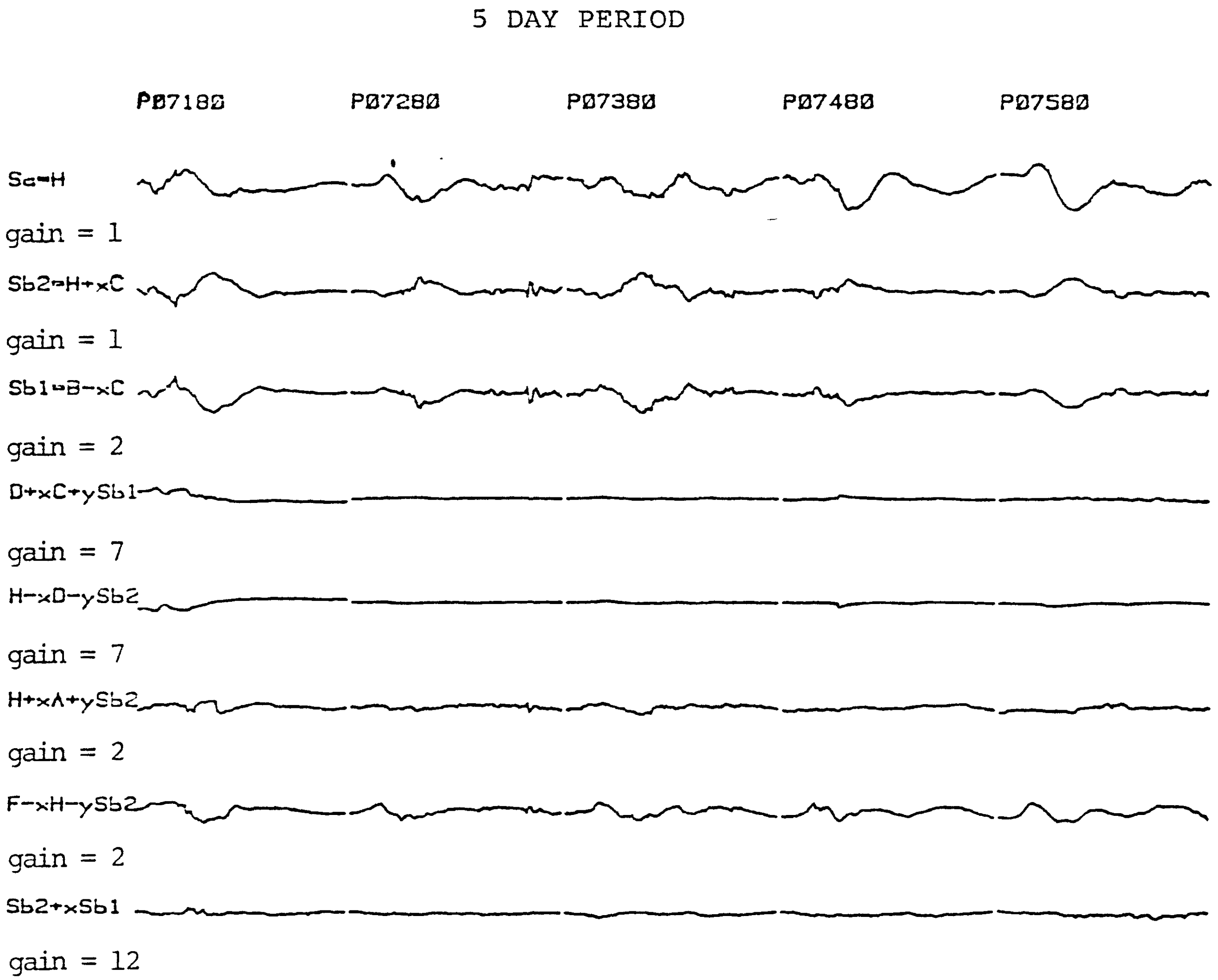

FIGURE 3.3 Palmdale Array Signals

represented are recorded as well. Temporal variations in the amounts of S_A and S_B in the residuals then are used as measures of the changes in the telluric tensor elements. By using combinations of cancellation residuals, the relative variation of an individual dipole signal or set of dipole signals can be determined uniquely. With this scheme, the sensitivities to tensor element variations are presently better than .1% over a period of a year.

Thus, Madden has developed a technique that is inexpensive and simple to implement yet achieves the goal of high sensitivity to variations in crustal conductivity. Stable circuitry and precise calibration schemes are necessary in the practical implementation of the telluric cancellation scheme but the only major weakness of this approach appears to be the dependence on the integrity of telephone lines. To use the telluric tensor information from the Palmdale array to constrain our crustal models, we need to establish relationships between the MT eigenstates and the telluric cancellation scheme.

3.2.3 Telluric cancellations and magnetotelluric tensor eigenstates

Before establishing the tensor cancellations in Palmdale, Madden noted that all of the low frequency dipole signals, had a dominant common component. This tendency is consistent with a nearly linearly polarized regional telluric field. This near linear polarization is a consequence of the regional crustal structure which, on the average, strikes parallel to the coastline and produces a highly anisotropic effective conductivity. In terms of eigenstates, this large anisotropy in the effective crustal conductivity produces a large spread in the impedance eigenvalue magnitudes and causes a general alignment of the eigenvectors perpendicular and parallel to strike. From our thin sheet modelling of southern California, described in Section 3.3, we found a wide spread in the eigenvalues for the area and a particularly large spread in the eigenvalues for the San Gabriel Mountains. Additionally, we found that the telluric eigenvectors for the impedance tensors in the San Gabriels to be aligned closely perpendicular and parallel to the strike of the mountains. Thus, we infer that dipoles spanning the San Gabriel Mountains will be strongly linearly polarized reflecting the large anisotropy in the eigenstates.

In Madden's Palmdale array, two dipoles span the San Gabriel Mountains (D and H) and their signals are virtually indistinguishable as predicted from the thin sheet analysis. Madden chose the larger of these dipoles as his independent signal S_A which we infer to be a related closely to the major eigenstate of the impedance tensor. When Madden used electronic differencing on pairs of dipole signals from the Palmdale array, he found that the residual signals all looked alike but were independent of the primary signal S_A. He interpreted these independent signals as the polarizations of the telluric field and chose two difference signals to be his S_{B1} and S_{B2}. Each dipole signal in his array, then, was interpreted as a linear combination of S_A and either S_{B1} or S_{B2}. The two difference signals used were:

$$S_{B1} = H + x_1 C \tag{3-4}$$

$$S_{B2} = B - x_2 C$$

Both of these signals can be considered as pseudo dipoles oriented along directions set by the weighted vector addition of the corresponding dipoles. Following this procedure for the areas spanned by dipoles B, C, and H, we find near alignment between the model minor eigenstate directions and the directions of S_{B1} but a less satisfactory result for S_{B2} as depicted in Figure 3.4. The model principal axes are the solid lines in each block and the dashed lines represent the principal axes inferred from array measurements. In the block containing dipole H, a dipole signal will be dominated by the major eigenstate except for a narrow band nearly perpendicular to the major eigenstate. Thus, estimating the S_{B2} direction from dipole signal directions is an inaccurate process. However, the correspondence between directions is sufficiently close to make us feel that the directions of Madden's independent signals are good approximations to the electric field eigenvector directions of the impedance

APPROXIMATE EIGENVECTOR DIRECTIONS

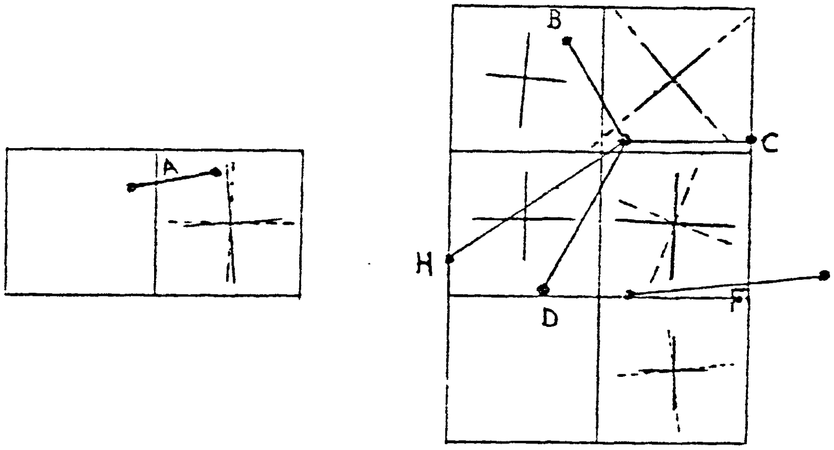

FIGURE 3.4

tensors for the Palmdale region. In sections 3.3 and 3.4, we use these approximate eigenstate relationships to constrain our crustal conductivity model of the Palmdale region.

3.2.4 Interpreting variations

For the remainder of this chapter, we seek to answer two questions. What variations in the tensor elements should we expect for changes in crustal conductivity and how should these variations be interpreted? Madden has hypothesized that the telluric cancellation approach, which involves an array of dipoles spanning a finite region, produces measures of the change in effective anisotropy of the crustal conductivity under the array. In the last section of this chapter, we shall reconsider Madden's hypothesis in terms of the results of our numerical models of the sensitivity of telluric measurements to changes in stress.

3.3 Generalized Thin Sheet Analysis

3.3.0 Introduction

The development and extensions of the treatment of the upper crust as a conducting sheet from Price's original analysis(1949) are described in the paper of Ranganayaki and Madden(1980). In this section, we shall outline qualitatively the basis for their model and its applicability to telluric resistivity monitoring along the San Andreas fault in California. We use the thin sheet modelling technique in in this chapter to predict the regional telluric field in Southern California centered near Palmdale. This region is a good example of varied crustal geology where a three dimensional MT modelling technique is necessary to account for large scale constraints on the local field.

3.3.1 Theoretical Basis

In the generalized thin sheet model, the upper crust is considered to be a thin conductive layer and the lower crust and part of the upper mantle a thicker resistive layer underlain by a conductive mantle. This generalized thin sheet earth model is based on the approximation that most of the change in the magnetic field occurs across the conductive sheet while most of the change in the elctric field occurs across the resistive sheet. For low frequency waves penetrating the earth, the ratio of skin depth to upper crustal thickness is large.

Because the lower crust is much more resistive, most of the induced current is confined to the upper crust with leakage to and from the mantle in regions of lateral conductivity contrasts where vertical E (electric) fields are generated. Ranganayaki and Madden introduced an "adjustment distance" term used to describe the spatial variation of the surface E field away from a lateral change in crustal conductivity. Near such a lateral conductivity contrast, the E field is distorted from its value far from the contrast. The distance required to diminish this distortion by a factor of 1/e is called the adjustment distance. The form of the adjustment distance is:

$$d_{adjustment} = (\sigma \Delta z_1, \rho \Delta z_2) \qquad (3\text{-}5)$$

where (σ) and (ρ) are functions of position on the surface (X,Y)

($\sigma \Delta z_1$) is the conductivity thickness product of the upper crust

($\rho \Delta z_2$) is the resistivity thickness product of the lower crust

From an ocean continent boundary, the adjustment distance may be as much as 1000 km over the ocean and 100s of kilomters over the continent. However, the importance of the adjustment distance concept for us is that low frequency E fields in areas exhibiting variety in crustal geology, are rarely "in adjustment" with the conductivity structure.

3.3.2 The Numerical Grid

In this thesis, I use Ranganayaki's (1979) numerical formulation of the magnetotelluric (MT) response for a generalized thin sheet earth model. A copy of her program, revised by Steve Park, is included in the Semi-Annual Technical Report to the USGS Geothermal Research Program by Prof. T.R. Madden(1980). In the present thin sheet formulation, the conductivity thickness product is allowed to vary as a function of position (X,Y) but the resistive sheet is modelled as a homogeneous layer overlying a layered model of the mantle. Figure 3.5 is a graphical representation of the numerical grid used. Each grid block can span electrically varied crustal sections. The average conductivity thickness product of each block is represented as a conductance tensor. Homogeneous blocks are assigned isotropic conductances. To assign conductances to the heterogeneous blocks, we assume that each block can be represented as geometric mix of two homogeneous sub blocks of equal volume. The sub block conductances are treated as circuit like elements and combined as series and parallel averages to determine the effective anisotropy of the conductance for each full block. The choice of block conductivities is based initially on the geology within each block as inferred from regional geology maps, known depths to basement and available resistivity data. Our procedure for assigning anisotropy to blocks is illustrated by example in Appendix

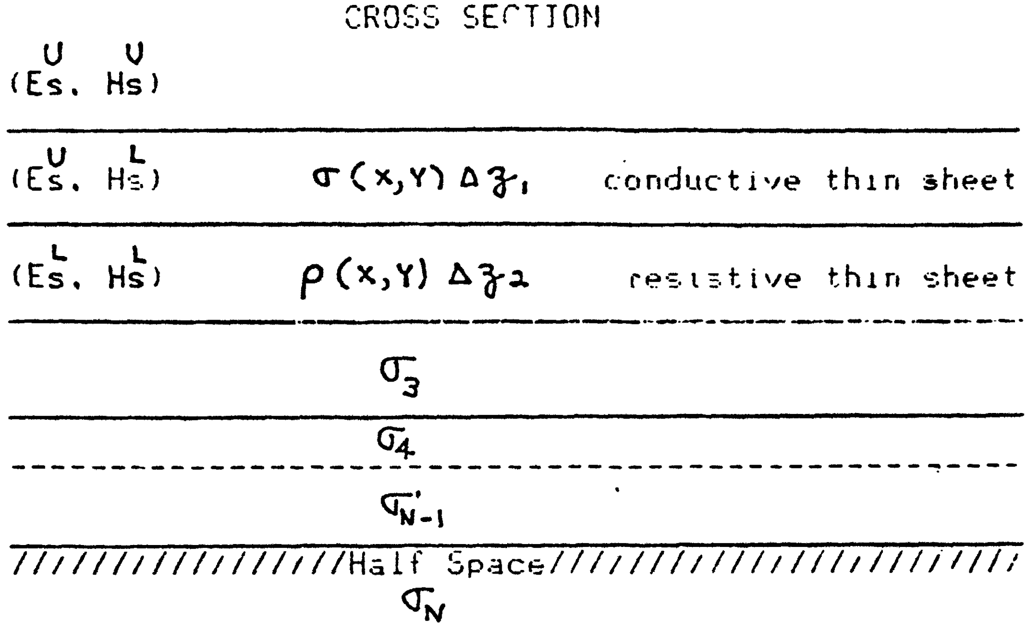

Es and Hs are the horizontal electric and magnetic fields at the top (U) and the bottom (L) of the thin sheet sandwich

Es = 0 across the conductive thin sheet
Hs = 0 across the resistive thin sheet

Generalized thin sheet geometry

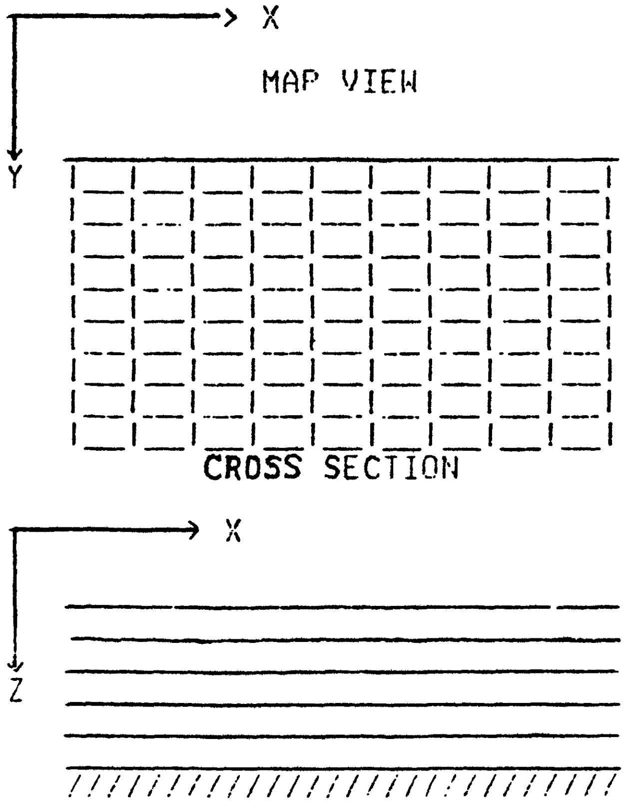

THIN SHFET NUMERICAL GRID FIGURE 3.5

E.

3.3.3 Block Conductance versus Stress

Ultimately, we wish to know the sensitivity of the Palmdale array measurements to changes in stress and strain (Madden, 1978). Consequently, we shall consider changes in the crustal conductance consistent with changes in stress. Given our base model, we perturb the stress and infer changes in the conductance tensor. The perturbed conductivity model is used with the thin sheet program to determine a new set of impedance tensors. The impedance tensors are then used to calculate telluric tensors which relate the electric fields for each block to a reference block spanning the middle of Madden's array. The sensitivity of the array is then inferred from the changes in tensor eigenstates for stress related changes in block conductances.

The calculation of the sensitivities of the block conductances to stress changes is based on the assumption that the electrical properties of the crust near Palmdale are crack controlled (Madden,1978). Accordingly, changes in block conductance are associated with the opening and closing of old cracks and the opening of new cracks. Cracks are opened along the applied stress direction (increasing conductivity) and closed perpendicular to the applied stress (decreasing conductivity). Under uniaxial stress, the conductance of a homogeneous block becomes anisotropic and the anisotropic conductance of a heterogeneous block is modified. Examples of how we model changes in the conductances of crustal blocks due to changes in stress are included in Appendix E.

3.3.4 Telluric Current Saturation Conditions

How the telluric current system responds to block conductance variations will be an important factor in the use of telluric measurements to monitor the state of stress in the crust. The electric field response to a block conductance change depends on the current saturation condition for that block. Perturbations in current density J can be expressed as:

$$\delta J = \sigma \, \delta E + E \, \delta \sigma \qquad (3\text{-}6)$$

For complete current saturation (Appendix D), no change in J occurs and:

$$\frac{\delta \sigma}{\sigma} = -\frac{\delta E}{E} \qquad (3\text{-}7)$$

For a totally unsaturated current condition, no change in E occurs and:

$$\frac{\delta \sigma}{\sigma} = \frac{\delta J}{J} \qquad (3\text{-}8)$$

In general, we can expect the current saturation condition for a crustal block to be between these two extremes and the electric field to reflect some fraction of the change in block conductance produced by a change in stress. Thus, the sensitivity of the electric field to block conductance changes depends on the role of that block in establishing the regional current distribution. In section 3.5, we compute the sensitivity of the electric fields to changes in block conductance using generalized thin sheet models, but first we shall describe the geophysical and geological constraints on our model and present our base crustal thin sheet model for the Palmdale area.

3.4 The Palmdale Thin Sheet Model

3.4.0 Content

In this section, we consider the geophysical constraints on our model of the crustal conductance near Palmdale. We use these constraints along with sediment thicknesses determined from gravity and geological mapping to infer an initial model. We present as well the base model MT and telluric eigenstates which are used as references for our stress sensitivity analysis presented in section 3.5.

3.4.1 Data Constraints

Constraints on our models are provided by telluric and magnetotelluric measurements as well as gravity and geological measurements. The MT data of Reddy et. al.(1979) are useful not only as constraints but serve also to illustrate the need for a regional approach to interpret local measurements. They obtained MT data in the San Gabriel mountains over the wide frequency band of .001 to 10 Hertz. From their data, presented as Figure 3.6, we infer that the low frequency current in the mountains is essentially perpendicular to the mountain-Los Angeles basin contact with the E field perpendicular to the contact much larger than the parallel E field. Analysis of the small E parallel field, based on a two dimensional model of the earth, has lead Reddy et al.(1979) to the interpretation that the San Gabriel mountains are

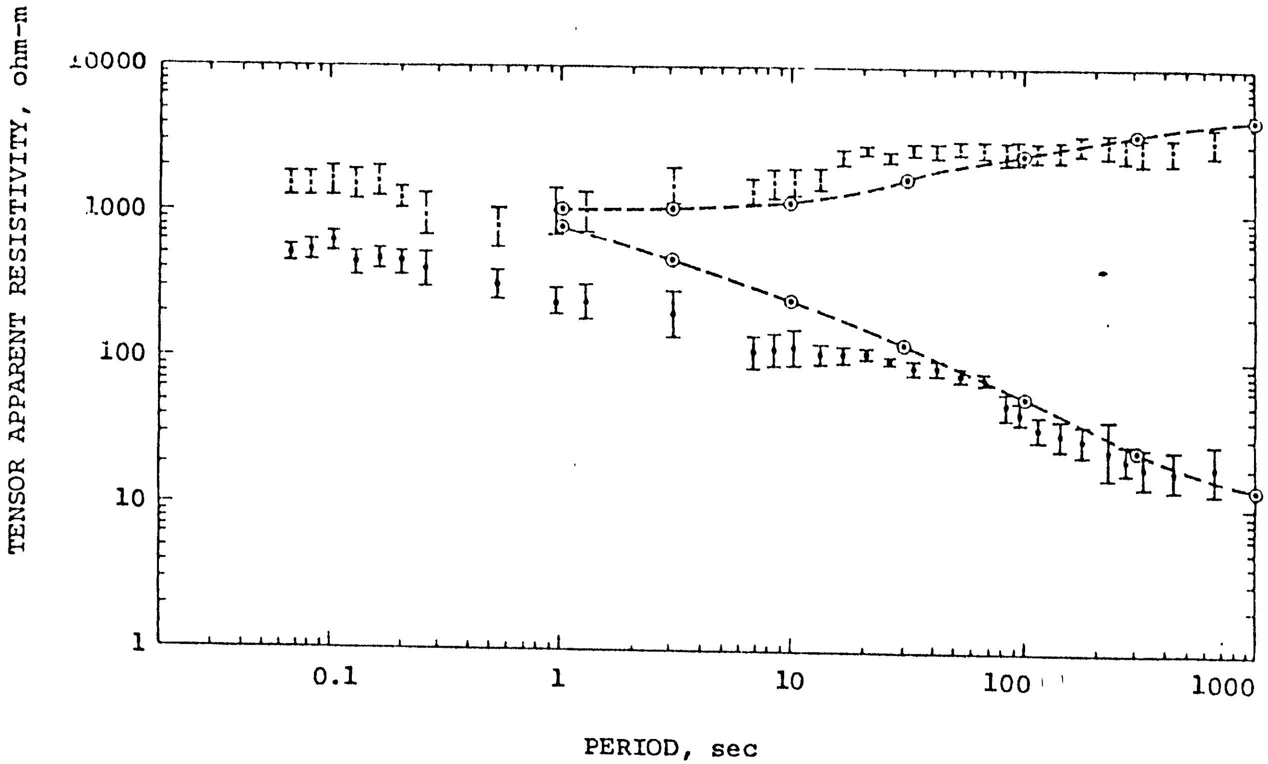

The magnetotelluric tensor apparent resistivity curves in the principal directions with their 95% confidence limits for the San Gabriel Mountains, from Reddy et al. (1977)

FIGURE 3.6

underlain by a conductive lower crust. Implicit in such two dimensional schemes is the assumption that the electric fields parallel to strike are in adjustment with the local geology i.e. the parallel field is set only by the local magnetic field and local geology. Ranganayaki and Madden(1980) using the generalized thin sheet approach have shown that the low frequency telluric field is set not only by the local but also the regional geology. Using their thin sheet approach we interpret the MT data of Reddy et al. to be consistent with the San Gabriels as a window to the lower crust with no requirement for a shallow conductive basement. Consistent with this interpretation, the large anisotropy in the low frequency electric field is a manifestation of the complicated regional geology. Further constraints on our regional resistivity model are provided by Madden's array of telluric measurements used to monitor resistivity near Palmdale, California and local bandlimited MT measurements also obtained near Palmdale.

As described previously in Section 3.2, the directions of the independent S_A and S_B signals are oriented respectively roughly parallel to the major and minor electric field principal axes of the magnetotelluric tensor. We compare the directions of these signals in each block spanned by dipoles in the array with the model principal axis directions and adjust the model to achieve correspondence. An example of this correspondence has been shown in Figure 3.4.

As a consequence of the telluric cancellation tensor scheme described earlier, we can relate each dipole in Madden's array to two other dipoles i.e. one dipole signal is a linear combination of two others. Thus, if the impedance tensor relating any two of our dipoles with the magnetic field is known, we can determine the impedance tensors for the remaining dipoles. While conducting MT field measurements near Palmdale, we recorded simultaneously telluric signals from the Palmdale array. From that set of measurements we have inferred the impedance eigenstates for pairs of dipoles within the array. Descriptions of our field procedures and details on the analytical approaches used can be found in Appendices A and C.

3.4.2 Conductance Assignments and the Base Crustal Model

The MT and telluric data from the Palmdale array plus the data of Reddy et al. are used to constrain model conductances of the San Gabriel Mountain blocks and the Mojave blocks near Palmdale and Lancaster. The conductances of the remaining Mojave desert blocks are inferred from a combination of our bandlimited MT measurements in the Mojave, gravity data (Hanna et al.,1974) and geological mapping of the western Mojave (Dibblee, 1967). Gravity and geological mapping data are used also to infer conductances for the San Joaquim Valley and Los Angeles Basin. The metamorphosed Precambrian and Mesozoic rocks of the Tehachapi, Sierra Nevada, San Gabriel and San Bernardino mountains were all assigned the same conductance.

Following the procedures outlined in Appendix E, we assigned anisotropic conductances spanning heterogeneous regions. Ocean block conductances were determined from the depth of the ocean and the assumption of 3.3 mhos/meter for sea water.

Our base model for the conductivity structure of the Palmdale region is shown as Figure 3.7. The blocks are square, 30 km on a side, and members of a 9 by 9 grid. We use matrix notation to designate each block such that I,J corresponds to the row and column of the block within the 9 by 9 grid. The effective thickness of the conductive thin sheet is 3 km. Beneath the conductive thin sheet, the earth is modelled as layered with the resistive upper crust as the top layer. Conductivities are in mhos/m and thicknesses in meters. The block conductivity indices are arranged in map form with their translation to conductivity listed below the map. The blocks most important to our analysis of the sensitivity of the Palmdale array are delineated by heavy lines in Figure 3.8. This region spans the array and includes a quite varied geological structure. Blocks 5,4-5,6 span the metamorphic Precambrian and Mesozoic terrain of the San Gabriel Mountains and are modelled as resistive homogeneous blocks. Blocks 4,3-4,6 span part of the

```
NUMBER OF BLOCKS:            X=9       Y=9
INDIVIDUAL BLOCK DIMENSION:    0.3000E+05X0.3000E+05 METERS
THIN SHEET THICKNESS    3 KM
CONDUCTIVITIES AND THICKNESSES FOR CAGNIARD LAYERED
MODEL BELOW THIN SHEET
  0.1000E-03      0.3000E+05
  0.1000E-01      0.7000E+05
  0.1000E+00      0.0
PERIOD=1000 SECONDS
     CONDUCTIVITY MAP
8  8  8  3  3  3  3  3  3
3  8  8  3  3  3  3  3  3
2  8  4  5  3  3  3  3  3
2  5  2  3  3  3  3  8  8
4  4  5  8  8  8  5  5  5
3  3  3  3  4  3  3  4  3
1  3  5  1  1  1  3  8  4
0  0  0  0  1  0  1  1  2
0  0  0  0  1  1  0  0  1

INDEX   CDXX         CDXY          CDYX         CDYY
  0    0.3000E+01   0.0           0.0          0.3000E+01
  1    0.4000E+00   0.0           0.0          0.4000E+00
  2    0.1000E+00   0.0           0.0          0.1000E+00
  3    0.5000E-01   0.0           0.0          0.5000E-01
  4    0.1750E-01   0.0           0.0          0.2000E-02
  5    0.5500E-02   0.0           0.0          0.2000E-02
  6    0.3300E-01   0.3000E-01    0.3000E-01 0.3300E-01
  7    0.3300E-01   -.3000E-01    -.3000E-01 0.3300E-01
  8    0.1000E-02   0.0           0.0          0.1000E-02
  9    0.1000E+00   0.0           0.0          0.1000E-02
```

Conductivities in mho/m; thicknesses in meters

Figure 3.7 Conductivity Model for Palmdale Array

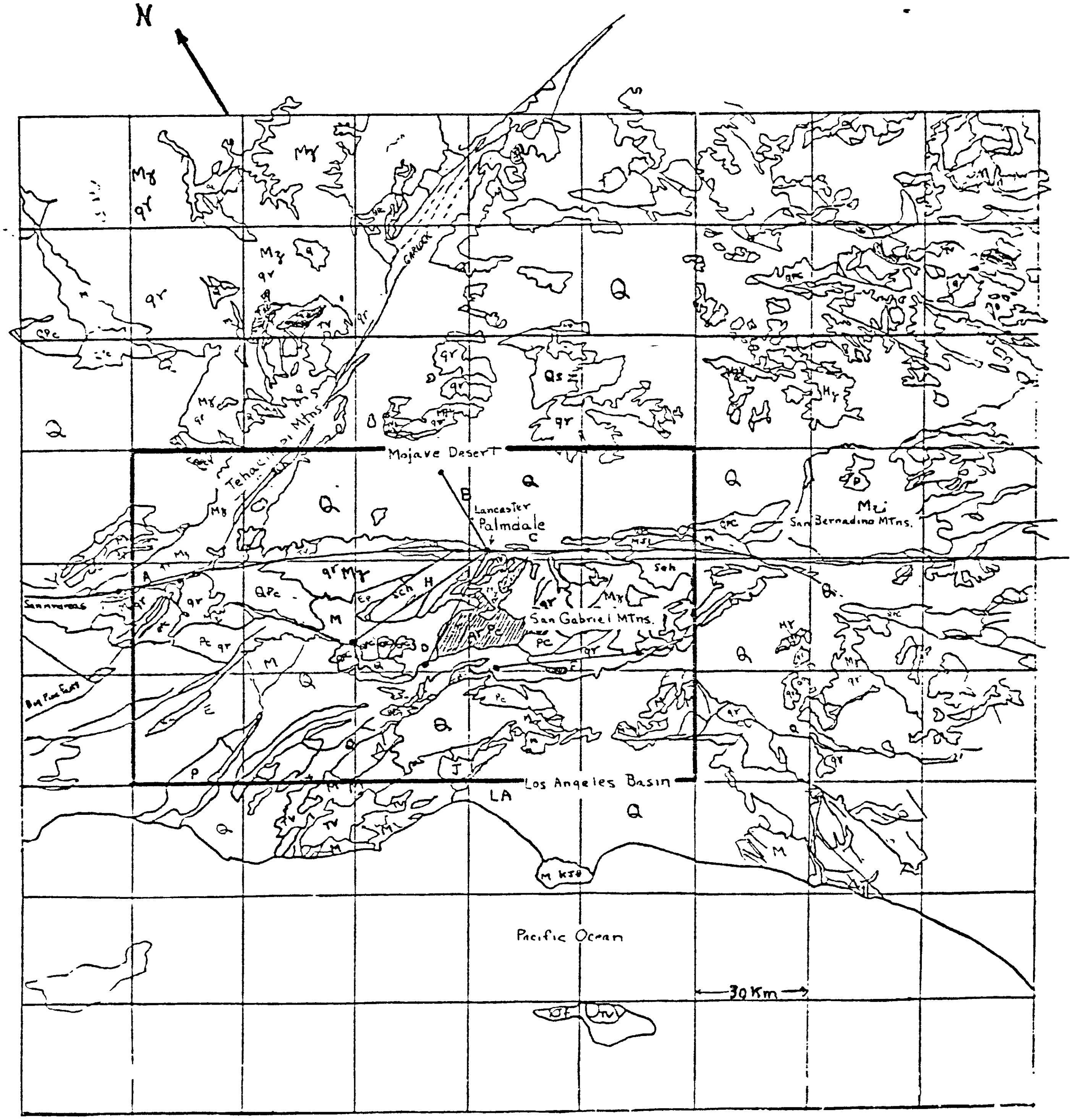

FIGURE 3.8 PERTURBED REGION

sediments of the Western Mojave Desert and are modelled as conductive and homogeneous. Blocks (4,2), (5,2) and (5,3) represent the heterogeneous transitional zone between the Tehachapi and San Gabriel Mountains. These blocks are modelled as anisotropic and more conductive than blocks 5,4-5,6. Blocks 6,2-6,6 represent part of the Los Angeles Basin, San Fernando Valley, and upthrusted marine sediments and are modelled as conductive and homogeneous.

Final adjustments to our base model were made by changing block conductances to achieve correspondence between the eigenstates for our model and data impedances. The impedance eigenstates for our base model are largely consistent with the bandlimited impedance (MT) data we used as constraints. The only difficulty we had in adjusting the model block conductances to fit the model to the narrow band data eigenstates occurred in the Lancaster-Palmdale block (4,5) where the eigenstate associated mostly with dipole C from Palmdale to Pearblossom was a factor of two larger than could be predicted with a reasonable set of conductances for the block based on local MT measurements and gravity profiles. We attribute this anomalously large eigenstate to a local resistive zone along the usually conductive San Andreas Fault system in which current may be funnelled. Another possibility is that the 24 km long dipoles B and C spanned sufficiently different structures that the description of the impedance as a tensor was unwarranted

(Kasameyer,1974).

3.4.3 Base Model Eigenstates

With our base model, we compute the impedance tensor eigenstates for each grid block and the telluric eigenstates relative to block 5,4 (row,column). The resultant MT eigenvectors are all essentially linearly polarized (small ellipticities) with appreciable skew only in the ocean blocks where current funneling occurs. We represent, graphically, the MT eigenstates for each block in two parts. Figure 3.9 is a representation of the electric field eigenvectors multiplied by their respective eigenvalue amplitudes and Figure 3.10 is a representation of the magnetic field eigenvectors. These representations are drawn on a geological map of the region which includes the locations of Madden's telluric array. The major and minor axes of the ellipses in Figure 3.9 represent the electric field amplitudes produced by the magnetic eigenvectors of Figure 3.10. As a point of distinction the ellipses of Figure 3.9 are not polarization ellipses. We have left out the ellipticity and eigenvalue phase information, because the ellipticities are small and vary little with conductance perturbations and the eigenvalue phases depend largely on the mantle conductivity which for our model does not vary with position. The ellipses point toward the directions of maximum electric fields in each block and reflect the effects of regional and local geology on the telluric current system. Our major use of

ELECTRIC EIGENVECTOR PRINCIPAL AXIS ELLIPSES FOR THE IMPEDANCE TENSOR

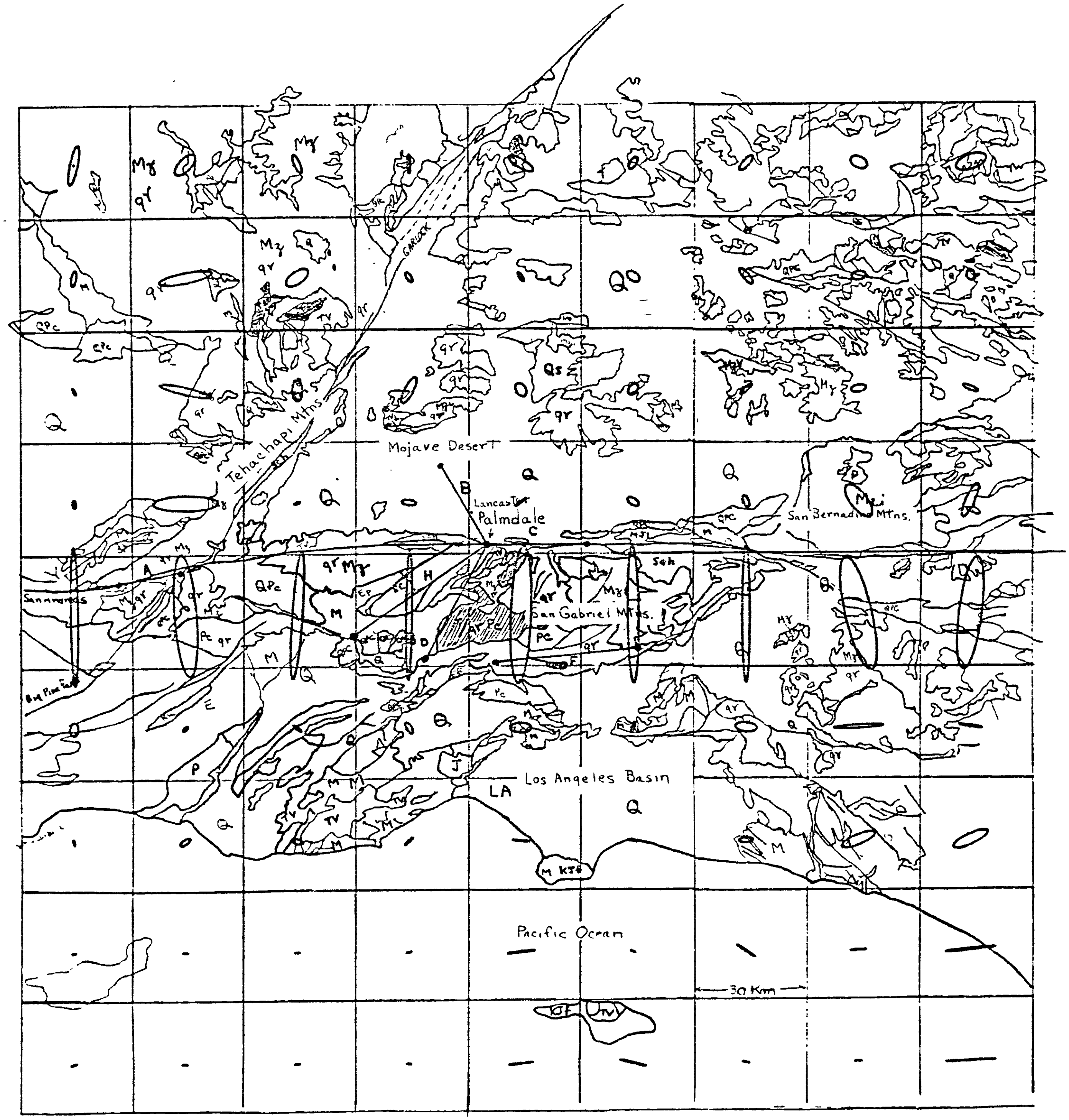

FIGURE 3.9 THIN SHEET MODEL EIGENVECTOR DIRECTIONS

MAGNETIC EIGENVECTOR PRINCIPAL AXIS DIRECTIONS FOR THE IMPEDANCE-TENSOR

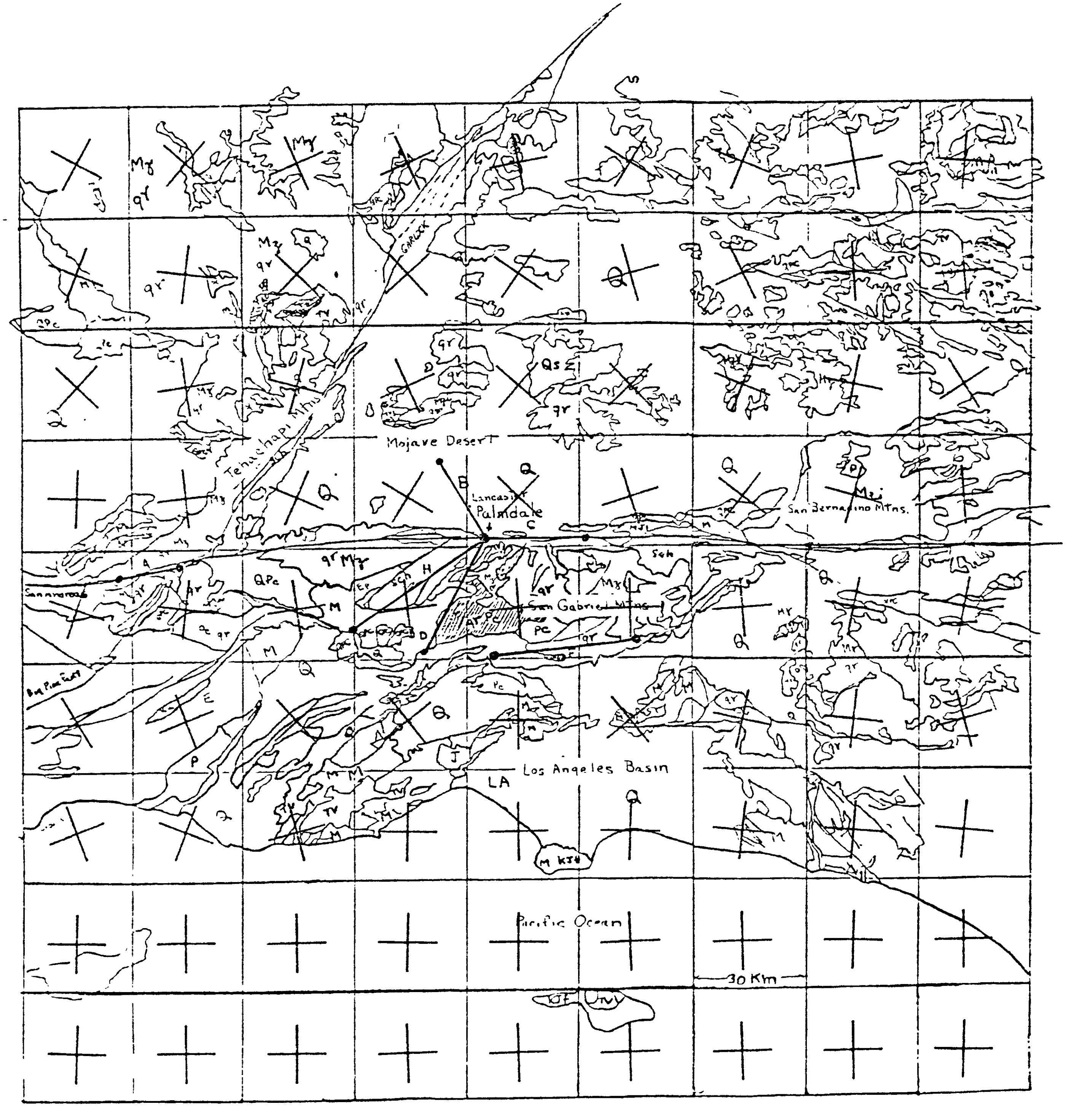

FIGURE 3.10 MAGNETIC EIGENVECTORS

the impedance eigenstates was to infer a reasonable crustal model within the constraints of our magnetotelluric measurements. However, the telluric tensor eigenstates can be used directly to infer the sensitivity of Madden's arrays. Consequently, for the rest of this chapter, we shall concentrate our efforts on the characteristics of the telluric eigenstates.

The telluric eigenstates for the Palmdale region are shown as Figure 3.11. The telluric ellipses for each block represent the maximum and minimum electric fields for that block due to unit electric fields in reference block 5,4 where dipoles D and H are located. The directions of the eigenvectors for block 5,4 are rarely more than 4 degrees from being parallel and perpendicular to the strike of the San Gabriel Mountains. Again, we have left out phase and ellipticity information. The phases of the telluric eigenvalues represent largely the phase differences between the impedance eigenvalue phases and are consequently nearly zero. The ellipticities of the eigenvectors are also small and vary little with conductance perturbations. The telluric ellipses for each block point toward the maximum contrast in resistivity between that block and the reference block, whereas the MT ellipses point toward the maximum resistivity direction. The correspondence of these directions, then, is a measure of the alignment of the maximum resistivity direction (MT) with the maximum change in resistivity. In the Palmdale

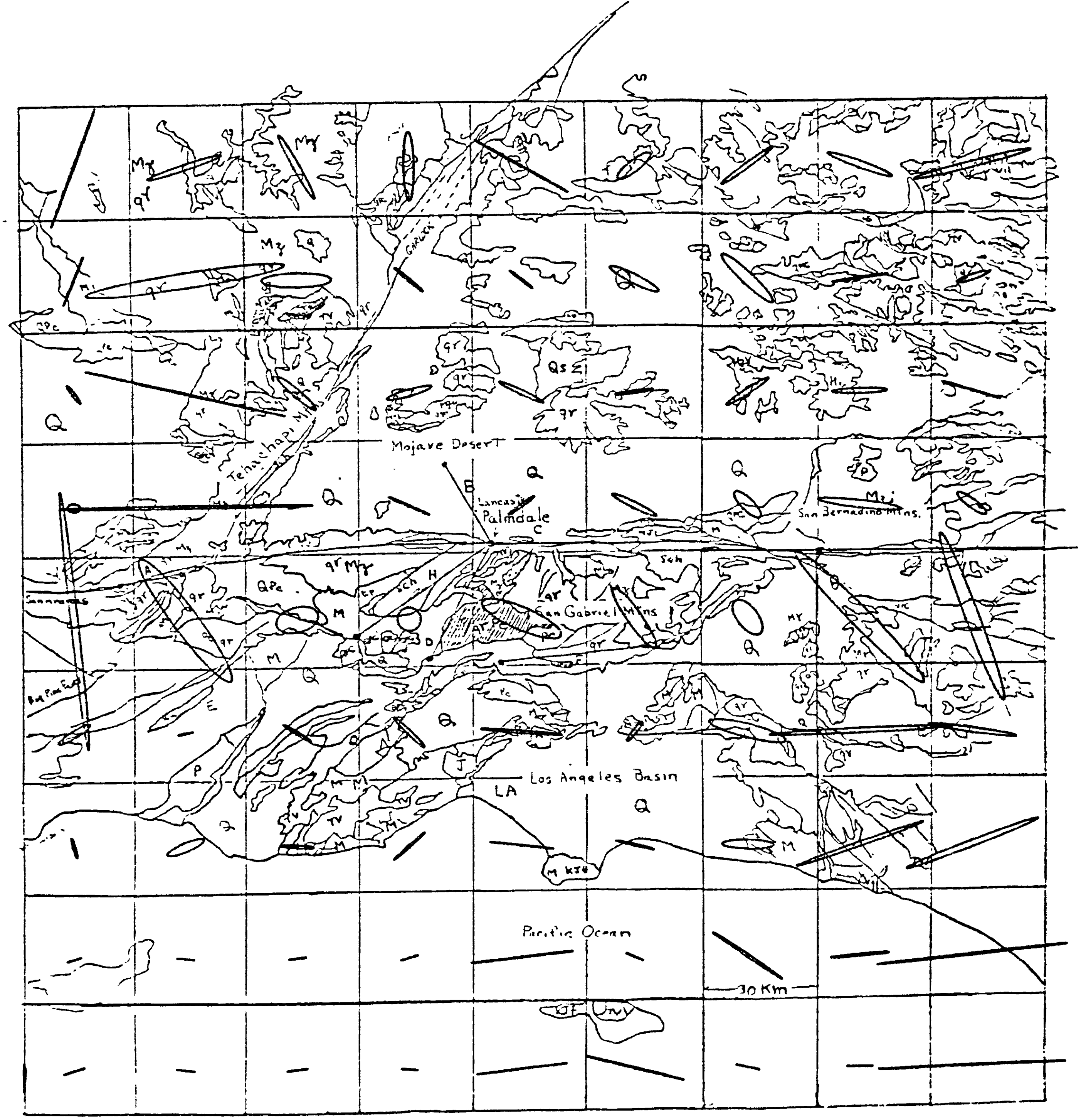

FIGURE 3.11 TELLURIC EIGENSTATES

region, the geological structure is aligned largely with the coastline with the result that both the maximum change in resistivity and maximum resistivity directions tend to be perpendicular to the coast and the impedance and telluric eigenstates exhibit similar principal directions.

3.5 Crustal Model Stress Sensitivity

3.5.0 Introduction

In this section, we discuss how the geological control of the telluric current system is reflected in the MT response of the Palmdale region. We consider then the implications of the current controls on the sensitivity of the telluric eigenstates to changes in block conductances. Next, we present the sensitivity parameters, eigenvalues and skew, which we use in our studies of the sensitivity of the telluric eigenstates to stress induced changes in block conductance. As noted previously, earthquakes occur at depths of 3 to 12 kilometers in the crust. In this study, we are considering only the upper portion of the earthquake depth range, because of limitations in our modelling procedures and the expected insensitivity of telluric measurements to variations in the resistivity of the lower crust.

3.5.1 Structural Control of the Telluric Currents

From Figure 3.9, we notice that the San Gabriel blocks, though modelled as isotropic, have strongly anisotropic responses. This large anisotropy occurs because the current flowing between the Mojave desert and the Los Angeles Basin must pass through the mountains causing large electric fields across the mountains. Conversely, most of the current parallel to the strike of the San Gabriels can bypass the mountains and be channeled in the Mojave desert and Los Angeles basin with a resultant small parallel E field in the mountains. The anisotropy in the eigenstates for the mountain blocks, then, is a consequence of the control of the telluric currents by regional structure.

The western Mojave is another region where the telluric current levels are controlled by regional structure. The western Mojave is a conductive wedge between the relatively resistive San Gabriel and Tehachapi mountains. Telluric currents parallel to the wedge bisector need pass only through the resistive tip of the wedge into the San Joaquim Valley and consequently will tend to be larger than currents perpendicular to the wedge bisector which must pass through the San Gabriel and Tehachapi mountains. Conductive blocks, then, tend to control the current levels in the crust while resistive blocks can influence the distribution of currents. With the exceptions of isolated resistive blocks, currents within a resistive block tend to be unsaturated and decrease in response to an increase in block conductance with the result that the electric field within the block will tend to remain constant. Thus, a stress induced conductance change in one of the San Gabriel Mountain blocks need not be expected to cause a change in the electric fields of that block but can be expected to cause changes in the electric fields of the adjacent Los Angeles Basin and Mojave Desert blocks because of the change in telluric current. Additionally, conductive blocks are more apt to be saturated because they play a greater role in setting the average telluric current levels than do the resistive blocks. Thus, the eigenstates of conductive blocks will tend to be more sensitive to conductance changes than the eigenstates of resistive blocks.

With the assumption that the resistive blocks have little control of crustal current levels, we can expect dipoles D and H in Madden's telluric array (Figure 3.2) to be largely insensitive to variations in mountain block conductances. Conversely, we can expect dipoles A,B,C, and F, which are located in more conductive areas, to be sensitive not only to conductance variations in their own blocks but also, to a lesser degree, to variations in adjacent unsaturated blocks.

3.5.2 Eigenstate Sensitivity Measures

The telluric tensor eigenstates are derived from the elements of the telluric tensor. Thus, the sensitivity of the telluric eigenstates to conductivity variations is a direct meassure of the sensitivity of the tensor elements. Another measure of the telluric tensor is the skew i.e. the difference between the directions of the corresponding eigenstates. Similar to the magnetotelluric skew formulation, the telluric skew angle can be represented as:

$$T_S = \arctan\left\{\frac{T_{xy} - T_{yx}}{T_{xx} + T_{yy}}\right\} \tag{3-9}$$

where the telluric tensor is represented as:

$$T = \begin{bmatrix} T_{xx} & T_{xy} \\ T_{yx} & T_{yy} \end{bmatrix} \tag{3-10}$$

In terms of the tensor eigenstates, the angle T_S is the angle between the $U_T^{(1)}$ and $U_T^{(2)}$ eigenvectors. When the directions of $u_{T1}^{(1)}$ is clockwise from the direction of $u_{T1}^{(2)}$, T_S is positive. For counterclockwise rotation, T_S is negative. A measure of skew can be determined even when only three dipole signals are used. The tensor relating three dipoles that have been rotated to a Cartesian coordinate system with one dipole aligned with a coordinate axis can be expressed as:

$$\begin{bmatrix} A \\ B \end{bmatrix} = \begin{bmatrix} T_{11} & T_{12} \\ 1 & 0 \end{bmatrix} \begin{bmatrix} B \\ C \end{bmatrix} = T \begin{bmatrix} B \\ C \end{bmatrix} \tag{3-11}$$

The skew angle for this tensor when all the elements are real is:

$$T_S = \arctan\left\{\frac{T_{12} - 1}{T_{11}}\right\} \tag{3-12}$$

We introduce the telluric skew, because it is sensitive to anisotropic changes in conductivity which can occur due to deviatoric stress. A simple example of this behavior can be inferred from our analysis in Chapter 4 of the tensor relating electrical fields inside and outside a conducting ellipsoid embedded in a conducting earth. The tensor relating these fields is symmetric with a resultant skew of zero. Isotropic changes in conductivity do not change the symmetry of the tensor. Thus, no change in skew occurs. However, anisotropic changes in conductivity cause the tensor to become asymmetric causing a finite skew. Thus, we deduce that an anisotropic change in the effective conductivity of the crust will result in a change in the telluric skew while isotropic conductivity changes will cause no change in skew. In our numerical modelling of the effects of perturbations in crustal conductivity, we shall determine the sensitivities of the telluric eigenstates and skew as measures of the sensitivity of Madden's telluric array measurements near Palmdale.

We present the results of two sets of conductivity perturbations. The first set involves isotropic conductivity changes associated with variations in hydrostatic stress and the second set involves anisctropic conductivity variations associated with changes in deviatoric stress. We define the sensitivity of the telluric eigenvalues to changes in block conductance as a relative percentage change such that:

$$S_T = \frac{\sigma}{\lambda} \frac{\delta\lambda}{\delta\sigma} * 100\,\% \qquad (3\text{-}13)$$

and we define the skew sensitivity as the change in skew angle for a percentage change in conductivity such that:

$$S_{T_S} = \frac{\delta T_S}{\left(\frac{\delta\sigma}{\sigma} * 100\right)} \qquad (3\text{-}14)$$

An eigenvalue sensitivity of 100% means that the change in block conductance is reflected completely in the eigenvalue variation and skew of one means that a one percent change in the conductivity produces a one degree change in skew. Changes in skew can be thought of as percentage changes relative to one radian such that a .57 degree change in skew is equivalent to a 1% change. In the final section of this chapter (3.6), we present the results of our sensitivity studies using the telluric tensor skew and eigenvalues as sensitivity parameters.

3.6 Sensitivity Analysis: Results

3.6.0 Introduction

This section is divided into three parts. First we make general observations applicable to both isotropic and anisotropic variations in crustal conductivity. Then, we discuss the sensitivities peculiar to isotropic and anisotropic variations and finally we apply these results to the Palmdale array measurements.

We perturb the conductivity of the crustal blocks delineated in heavy ink in Figure 3.8. This region includes the Palmdale array and spans a varied geology as described in Section 3.4. Eigenvalue and skew sensitivities are calculated for the blocks which span the Palmdale array within the perturbed region. Variations in the eigenvalues are determined from the model electric fields for a spatially invariant magnetic field source. The eigenvalue sensitivities for each block are measures of the change in apparent resistivity of that block with respect to our reference block (5,4) which includes dipoles D and H in the Palmdale array. The skew sensitivities are measures of anisotropic changes in the resistivity contrast between the measurement and reference blocks.

3.6.1 General Results

The general pattern of eigenvalue sensitivity is a manifestation of the role of the individual blocks in determining the levels and distribution of the telluric current system. The eigenvalue sensitivities of the more conductive blocks (4,3)-(4,6) and (6,2)-(6,6) tend to be much higher than the sensitivities of the resistive mountain blocks (5,4)-(5,6). In the conductive blocks, small changes in current occur for a change in conductivity with the result that most of the conductivity change is reflected in the electric fields. For the mountain blocks, changes in conductivity cause the current levels to change with the result that no change occurs in the electric fields for those blocks. However, the actual current change is so small relative to the unperturbed current levels that little effect is seen in the electric fields of surrounding current saturated blocks.

Conductivity variations in blocks which cause the current levels to change in the reference block result in a diffused eigenvalue sensitivity. All of the block eigenvalues change proportionally to the change in the apparent conductivity of the reference block.

Blocks in the Mojave Desert and Los Angeles Basin tend to be partially saturated with the result that variations in one block affect the current levels in the nearby blocks and all the block eigenvalues change. The implication of this sensitivity diffusion is that the inference of a variation in many of the Desert or Basin blocks from telluric measurements is not unique. In fact, only completely current saturated blocks will produce an eigenvalue variation that can be determined uniquely from telluric measurements.

3.6.2 Isotropic versus Anisotropic Conductivity Variations

Isotropic conductivity variations are consistent with variations in hydrostatic stress while anisotropic variations are consistent with deviatoric variations in stress (Appendix E). For isotropic variations, both eigenvalues of the telluric tensor tend to change together while for anisotropic changes the eigenvalues can vary in opposite directions. For isotropic changes, negligeable variation in skew occurs but for anisotropic changes the skew varies as much as .4 degrees/percent change in block conductivity. For anisotropic changes, the eigenvalue sensitivities are less than their isotropic counterparts because part of the anisotropic variation is reflected in the change in skew. Thus, changes in skew and the signs of the eigenvalue variations can be used to distinguish between hydrostatic and deviatoric stress variations. Figures 3.12-3.14 are, respectively, matrices of the relative sensitivities of the isotropic eigenvalues and anisotropic eigenvalues and skews. Each row represents the sensitivity of one block to variations in the corresponding blocks in the columns of the matrix.

3.6.3 Conclusions

From our sensitivity analysis of the Palmdale region, we have found that the telluric tensor parameters

$$S_{\lambda} = \frac{\sigma}{\lambda}\,\frac{\delta\lambda}{\delta\sigma} \times 100$$

Isotropic Conductivity changes

Block Indices	4,2	4,3	4,4	4,5	4,6	5,3	5,4	5,5	5,6	6,3	6,4	6,5	6,6
4,2	-38 -7	12 -22	-6 -31	4 -3	-13 -12	-26 8		-17 1	-27 16	-23 -42	-17 -16	-19 -7	-17 -16
4,3	3 -6	-83 -84	5 0	6 0	0 1	-6 -8		-1 2	-3 5	2 -2	-1 0	0 1	2 0
4,4	63 3	67 39	-22 -34	76 58	59 56	62 -2		-69 -4	53 -2	56 51	61 60	56 34	58 56
4,5	-50 23	-46 -27	-43 -34	-200 -200	-50 -38	-73 -14		-64 -8	-200 -28	-50 -39	-53 -57	-53 -22	-62 -44
4,6	-13 4	-13 5	-13 -18	-10 -5	-76 -77	-15 -9		-22 3	-14 -35	-14 -5	-16 -24	-16 -16	-19 -36
5,3	-14 3	-17 -3	-14 18	-15 -13	-14 -10	-26 -8		-14 1	-11 3	-16 0	-10 -14	-14 1	-15 -15
5,4	3 4	3 12	3 7	4 1	3 3	4 1		4 1	3 2	3 4	3 3	4 0	3 3
5,5	-4 -3	-3 0	-3 -2	-5 -2	-5 -4	-2 -10		-9 -6	-8 0	-4 -1	-5 -5	-5 3	-4 -9
5,6	0 1	1 2	0 1	0 -1	0 -1	1 0		1 -1	-2 -3	0 0	1 1	0 5	-2 1
6,3	15 3	18 38	15 2	16 16	1	-4 5		21 0	15 -5	-36 -45	21 16	14 23	16 23
6,4	52 -5	50 31	57 57	54 48	50 49	85 14		37 5	40 20	60 -88	-8 -19	51 -32	63 58
6,5	31 -1	-31 -9	-30 -10	-23 -40	-32 -30	-19 -21		-59 2	-52 43	-31 -24	-32 -75	-66 -27	-36 -117
6,6	-10 -1	-10 -10	-9 -3	-11 -4	-11 -2	-14 -3		-14 -1	-20 1	-10 -5	-7 -6	-12 35	-64 -76

Figure 3.12 Isotropic Eigenvalue Sensitivities

$$S_{\lambda_{\boxed{1/2}}} = \frac{\sigma}{\lambda}\,\frac{\delta\lambda}{\delta\sigma} \times 100$$

Block Indices I, J

Anisotropic Conductivity changes

	4,2	4,3	4,4	4,5	4,6	5,3	5,4	5,5	5,6	6,3	6,4	6,5	6,6
4,2	44 -3	-11 32	-5 41	-1 32	16 14	32 -9	X	21 0	32 -14	28 49	21 19	23 8	21 20
4,3	5 -5	102 -71	5 17	3 8	8 6	18 9	X	12 -2	12 -7	7 5	11 9	9 3	7 8
4,4	-68 -1	-71 -32	87 -64	68 -56	-64 -59	-85 -8	X	-62 8	-71 1	-61 -64	-58 -51	-60 -26	-58 -54
4,5	-19 7	-22 -4	-19 -2	20 -40	-23 -39	-17 -6	X	-12 10	-43 7	-18 -14	-16 -16	-19 6	-15 -11
4,6	-8 5	-9 15	-7 -3	-11 93	41 -41	-12 0	X	-13 -16	11 29	-4 -4	-6 -13	-3 -9	-16 -16
5,3	15 22	18 14	15 22	17 15	15 13	28 1	X	15 2	12 3	17 10	11 14	14 10	16 13
5,4	-4 3	-4 -3	-3 6	-4 -2	-4 -3	-4 0	X	-4 1	-3 2	-3 -3	-3 1	-4 6	-4 -4
5,5	5 3	5 2	4 0	6 3	5 4	5 2	X	7 0	4 -3	5 2	6 9	6 11	6 9
5,6	0 1	0 1	0 0	1 2	1 0	0 0	X	-1 -1	0 2	1 2	0 0	0 0	0 -2
6,3	38 -1	37 47	39 36	41 35	39 41	61 12	X	38 1	28 6	67 12	19 40	39 35	34 23
6,4	-78 -6	-77 -40	-75 -6	-78 -81	-81 -76	-57 -34	X	-93 -5	-87 -1	-82 -46	-70 -66	-98 34	-73 -72
6,5	23 0	22 6	22 5	16 29	24 21	14 14	X	44 -2	40 -31	23 17	25 53	47 8	29 20
6,6	7 -3	7 10	8 -6	10 3	5 8	5 2	X	-8 2	6 31	7 16	8 1	-3 -113	-2 22

Figure 3.13 Anisotropic Eigenvalue Sensitivities

Block Indices I,J

$$S_{T_s} = \frac{\delta T_s}{\left(\frac{\delta\sigma}{\sigma} \times 100\right)}$$

Anisotropic conductivity changes

(zero sensitivity for unmarked blocks)

	4,2	4,3	4,4	4,5	4,6	5,3	5,4	5,5	5,6	6,3	6,4	6,5	6,6
4,2		+.1	-.1			+.3							
4,3		-.2				-.1							
4,4			+.3	.1		-.2		+.2	+.1	+.1			
4,5				-.4	-.1	-.1		+.1	+.1				
4,6				+.1	+.3			+.3	+.1				
5,3													
5,4				-.1									
5,5													
5,6												-.1	
6,3						+.1				+.3			
6,4						+.3			+.2		+.4	-.1	
6,5						-.1		-.2		-.2			+.2
6,6									+.1			+.1	-.3

Figure 3.14 Anisotropic Skew Sensitivities

eigenvalue and skew are important to determine not only the levels of conductivity variations but also the the type of variation. We find that measurements in the Mojave Desert (dipoles B and C) should be sensitive to conductivity variations not only under the dipoles but also in the surrounding areas of the Mojave. Additionally, dipoles A and F are located in nearly current saturated regions and should be sensitive largely to local variations although dipole F may also be affected by changes in adjoining regions.

Dipoles D and H span the largely current unsaturated San Gabriel Mountains and are insensitive to variations in conductivity. One of these dipoles is useful as a reference but the other appears redundant.

Chapter 4

INDUCED POLARIZATION WITH TELLURIC FIELDS

4.0 Introduction

The term induced polarization (IP) is applied to an electrical prospecting technique designed to detect the presence of metallic minerals by measuring the surface polarization effects induced on the metals by currents in the ground. For an in depth review of the IP technique, read the paper by Cantwell and Madden (1967). Here we present only those aspects of IP necessary for our studies.

Electrical conduction in rocks is due predominantly to the flow of ions through pore spaces. The presence of metallic minerals in and near the rock pores adds an electrochemical barrier to electrical current because of a change in the conduction mechanism from ionic to electronic. This added electrochemical impedance is due to the depletion or excess of current carrying ions at the metal solution interface. The ion imbalance is compensated by diffusion to or from the solution. Because diffusion is time dependent (or equivalently frequency dependent) current through a metal solution interface will require a finite time to equilibrate after an electric field is applied and will decay accordingly when the applied field is removed.

The impedance of a metallic mineral bearing rock can be represented by purely resistive paths due to conduction through barren pores acting in parallel with partially mineralized paths which are time/frequency dependent. A simplified circuit analog of the IP impedance is depicted in Figure 4.1 from Cantwell and Madden (1967).

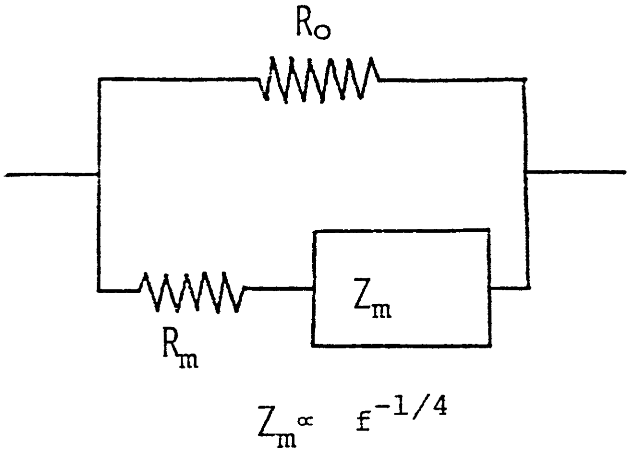

Figure 4.1 Equivalent Circuit for mineralized rock

where Ro represents the barren pore paths and $(R_m + Z_m)$ represents the mineralized pore paths. The impedance of metal bearing rocks varies from 1 to 100% per decade of frequency in the band .01 to 100 Hz with associated phase shifts typically less than 1 degree per decade (Cantwell and Madden,1967).

In practice, a time varying source current is applied to the ground and the potential is measured as a function of position. For time domain methods, the source current is switched on and off and the rise and decay times of the potential used to infer the presence of IP targets. Both techniques are limited by noise from electromagnetic coupling at high frequencies (>100 Hz) and tellurics at low frequencies (<1 Hz) where the telluric field increases rapidly with decreasing frequency (Cantwell,1960). The presence of the telluric field, then, limits the depth to which IP targets can be discerned using active measurements. To alleviate this low frequency noise problem, Halverson (1981) has used telluric cancellations to remove tellurics from his active IP measurements. Also, Madden(1979), in an oral presentation to the first biennial SEG meeting in Australia, proposed using the telluric fields directly to infer the presence of an IP target by analyzing the relative frequency dependence of telluric measurements within and near the target. In this chapter, we consider the feasibility of applying Madden's premise to actual field data.

We model the IP target as an embedded ellipsoid of revolution whose conductivity varies with frequency. Then, using an approximate extension of the electrostatic field solutions for an embedded ellipsoid, we predict the frequency dependence of the telluric tensor eigenstates. Next, we calculate the frequency dependence of the telluric tensor eigenstates for field data obtained near an IP target, a pyritic schist near Harvard, Mass. We then compare our model and data analyses and set bounds on the applicability of our models and our ability to discern the IP frequency effects in telluric data corrupted by noise. As a control study, we analyze telluric data from Salinas, Ca. where no IP effect is expected.

The results of our studies can be summarized as follows:

(1) To discern unambiguously the frequency dependence of the telluric field associated with an IP target, the coherency in predicting one field component in terms of two others must be high (the order of .995).

(2) For low noise measurements, the eigenstate analysis allows us to study the electrical properties of the earth beneath the measurements free from source effects.

(3) Frequency effects consistent with the presence of an IP target were inferred from the Harvard data and no such frequency effects were found in the data from Salinas.

(4) The ellipsoidal approximation to a 3D heterogeneity provides useful qualitative insights but care must be used in its quantitative application.

The rest of this chapter is divided into four sections. In section 4.1. we consider the effects of measurement geometry on our ability to discern IP effects in the telluric field and develop a strategy for conducting field measurements. In section 4.2. we present our analysis of telluric data from the vicinity of an IP target, a pyritic schist near the town of Harvard, Mass. In section 4.3. we present the analysis of similar small scale telluric measurements obtained near Salinas. Ca. where no IP related frequency dependence was expected and in section 4.4. we summarize our results and make recommendations for further study.

4.1 Telluric measurement geometries for discerning IP targets

4.1.1 The ellipsoidal model (Appendix D)

In Appendix D we present the algebraic formalism for the electrostatic response of a conducting ellipsoid of revolution (spheroid) embedded in a conducting earth and the approximate extension of this analysis to the low frequency telluric field response to a buried spheroid. With this approximate analysis, we establish a model of the telluric tensor relating the telluric fields across the boundary of the embedded spheroid. As a consequence of spheroidal symmetry and the curl free nature of the DC field, our model of the telluric tensor is shown to be symmetric and the directions of the two parallel sets of tensor eigenvectors not only insensitive to the conductivity contrast of the ellipsoid with its surroundings but also always normal and parallel to the surface of the ellipsoid. Additionally, we find that for thin spheroids exhibiting moderate conductivity contrasts, measurement positions exist for which one of the tensor eigenstates can be insensitive to the frequency dependence of the spheroidal IP target. Thus, the directions of the tensor eigenvectors are set only by geometry whereas the eigenvalues and their frequency dependences are set by conductivity contrast and target shape.

4.1.2 Array locations and configurations

In the preceding discussion of our model of the telluric tensor, we have assumed tacitly that the tensor was calculated from two electric field measurements at each side of an ellipsoidal ore body. In a practical situation the location of the ore body is unknown and a strategy for prospecting with telluric measurements need be established. Accordingly, we seek now to answer the question, what measurement configurations and locations are necessary to infer the frequency dependent eigenstates of the telluric tensor when the IP target has the shape of a prolate or oblate spheroid? Additionally, we wish to streamline our measurement system to allow rapid coverage of regions where an ore body is expected to exist. In accordance with these goals, we shall present first the "normal" method of inferring the telluric tensor using four dipole measurements. Then, we simplify the geometry to a three dipole system and investigate the conditions under which this logistically simpler system can be used to infer the presence of an IP target.

To calculate the telluric tensor at a field site, an array of four dipoles with a common center can be used as depicted in Figure 4.2. In general, the angles between dipoles can be somewhat arbitrary and are chosen usually to conform with the terrain, the road system, or suspected target boundaries. In Figure 4.2, dipoles A and C are chosen roughly parallel as are dipoles B and D. The

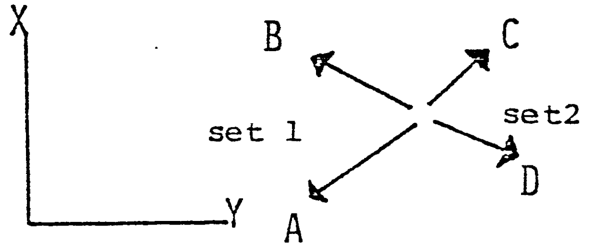

Figure 4.2 Four dipole telluric tensor geometry

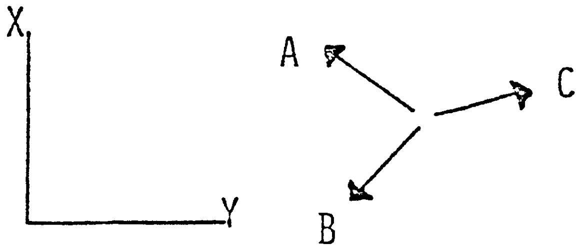

Figure 4.3 Three dipole measurement geometry

tensor relationships between dipole set 1 (A and B) and dipole set 2 (C and D) are calculated and rotated to the Cartesian coordinate axes X and Y. The tensor eigenstates are then calculated in this coordinate system. A logistically simpler measurement approach is to use a three dipole array with a common center as depicted in Figure 4.3. With only three dipoles, we can calculate a tensor relationship of the form:

$$\begin{bmatrix} A \\ B \end{bmatrix} = \begin{bmatrix} T_{11} & T_{12} \\ 1 & 0 \end{bmatrix} \begin{bmatrix} B \\ C \end{bmatrix} = T \begin{bmatrix} B \\ C \end{bmatrix} \qquad (4 - 1)$$

and after rotation to X and Y coordinates, the eigenstates of this three dipole tensor can be inferred. Both the three and four dipole tensors can be analyzed for the presence of an IP target when the centers of the dipole arrays are within or near the boundaries of the target. The most important aspect of the array location is that at least one dipole must exhibit sensitivity to the frequency dependence of the IP target while a second dipole must exhibit little or no sensitivity to this frequency dependence. Now let us consider how the position of the array center can affect the frequency dependence of the tensor eigenstates.

Using three dipoles as shown in Figure 4.3. at least one of the tensor eigenstates will be sensitive to the presence of an IP target when one of the dipoles is within the target boundaries because of the relative frequency dependence of the dipole signals. However. if all three dipoles are within the IP target boundaries, usually there will be no indication of the presence of the IP target because all three dipoles will have the same or close to the same sensitivity to conductivity changes with frequency. The one exception to this rule occurs when the current saturation condition, described in Appendix D, is anisotropic within the IP target. For example, when the current within the target is saturated to changes in conductivity in one direction and unsaturated in another, the frequency dependence of the telluric field will be anisotropic and, consequently, at least one of the telluric eigenstates will be a function of frequency. If one or more dipoles span the target boundaries, our ability to discern the target is diminished because the tensor eigenstates will reflect the mix of frequency dependences of the IP target and its surroundings. As Figure 4.4, we present a summary of the important three dipole array geometries associated with the detection of IP targets with telluric fields. Additionally. we feel that the major advantage of using a four dipole array instead of a three dipole array is the reduction of the possibility that none of the dipoles lies within the confines of the IP target, but that this advantage does not outweigh the logistical simplicity of the three dipole system.

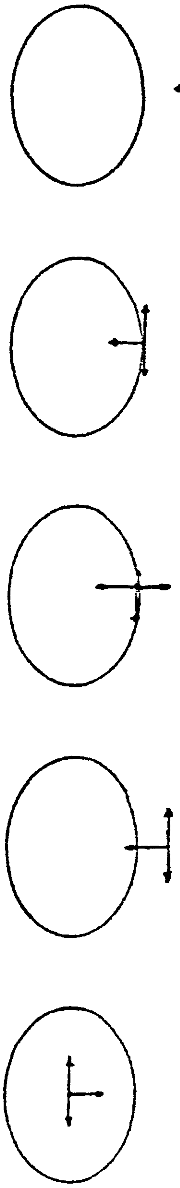

Three dipoles outside target

No measureable IP effect

One dipole inside, two outside

At least one eigenstate will exhibit part or all of the frequency dependence of the IP target

Two dipoles inside, one outside

Both eigenstates will exhibit the full effects, unless an anisotropic current saturation condition exists

One dipole partially inside, two outside

One eigenstate will exhibit partial frequency dependence of the IP target

Three dipoles inside

No observable frequency dependence unless an anisotropic current saturation condition exists

FIGURE 4.4 MEASUREMENT SENSITIVITIES

Our strategy for IP prospecting with tellurics is, then. to use three dipole arrays over a region where the presence of an IP target is suspected. In particularly promising areas, we suggest orienting two colinear dipoles normal to the suspected boundary of the IP zone to maximize the frequency dependence of the related tensor element. The number of measurements required to delineate the IP zone will depend on complexity of its boundary, the size of the zone and the degree of a priore geological control. Let us now apply these concepts to the inference of the boundary of a pyritic schist near Harvard, Mass.

4.2 Telluric field measurements near an IP site

4.2.1 Previous geoelectric measurements near Harvard, Mass.

Harvard, MA is a town located approximately 40 miles northwest of Boston (Figure 4.5). The basement rock in the Harvard area is largely Ayer granite with dispersed metamorphosed remnants of older sedimentary structures. One of these remnants is a mica schist facies of the Worcester formation. This schist contains varying amounts of pyrite and graphite and exhibits an IP response. East of the center of Harvard, the schist is a topographic high upon which the Harvard Observatory is located. Over the past two decades, geophysical surveys have been conducted within and near the observatory's grounds including the pioneering magnetotelluric studies of Cantwell (1960).

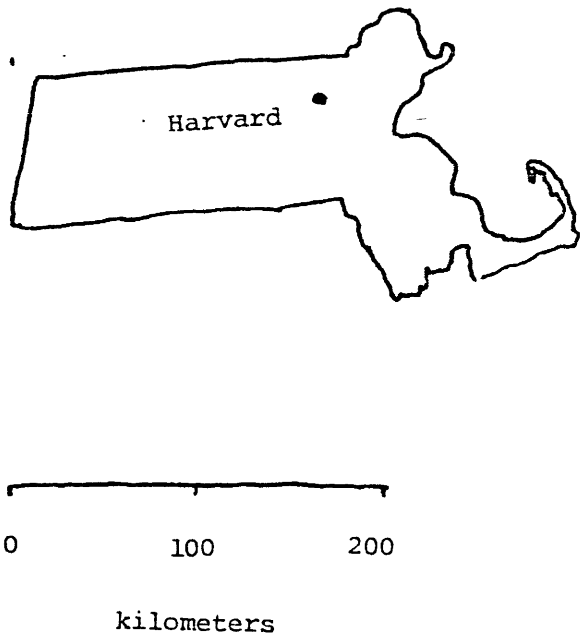

Figure 4.5 Location Map for Harvard, MA

Recently a study of the lateral heterogeneity of the crust in the Harvard area was conducted by Bob Davis (1979), and in 1979 and 1980 active source resistivity and IP measurements were conducted on a smaller scale by students in the MIT Geophysics Field Course under the tutelage of Prof. Madden and Steve Park.

From the active source measurements, the Worcester formation has been inferred to be more conductive ($\sim$10-100 Ω-m) than its surroundings (Ayer granite, ρ=1000-10,000 Ω-m) and, because of the presence of pyrite, to exhibit an IP effect of approximately 10%/decade of frequency. From geologic maps of the area, the surficial expression of the Worcester formation is a narrow (1-1.5 km) schist extending tens of kilometers in a NE-SW direction as depicted in Figure 4.6 from Davis (1979). Using magnetotelluric measurements in the 50-150 second band, Bob Davis inferred that the schist was not only a shallow feature ($\sim$1.5 km) relative to its length but was pinched out by Ayer granite near Whitney Road (see Figure 4.6). Thus, the Worcester formation near Harvard can be modelled as an elongated three dimensional conducting body which exhibits an IP response and is embedded in a more resistive granite host.

To test Madden's hypothesis that the telluric fields inside and outside an IP target would exhibit relative frequency dependence, we have conducted telluric field measurements in and near the schist. Additionally,

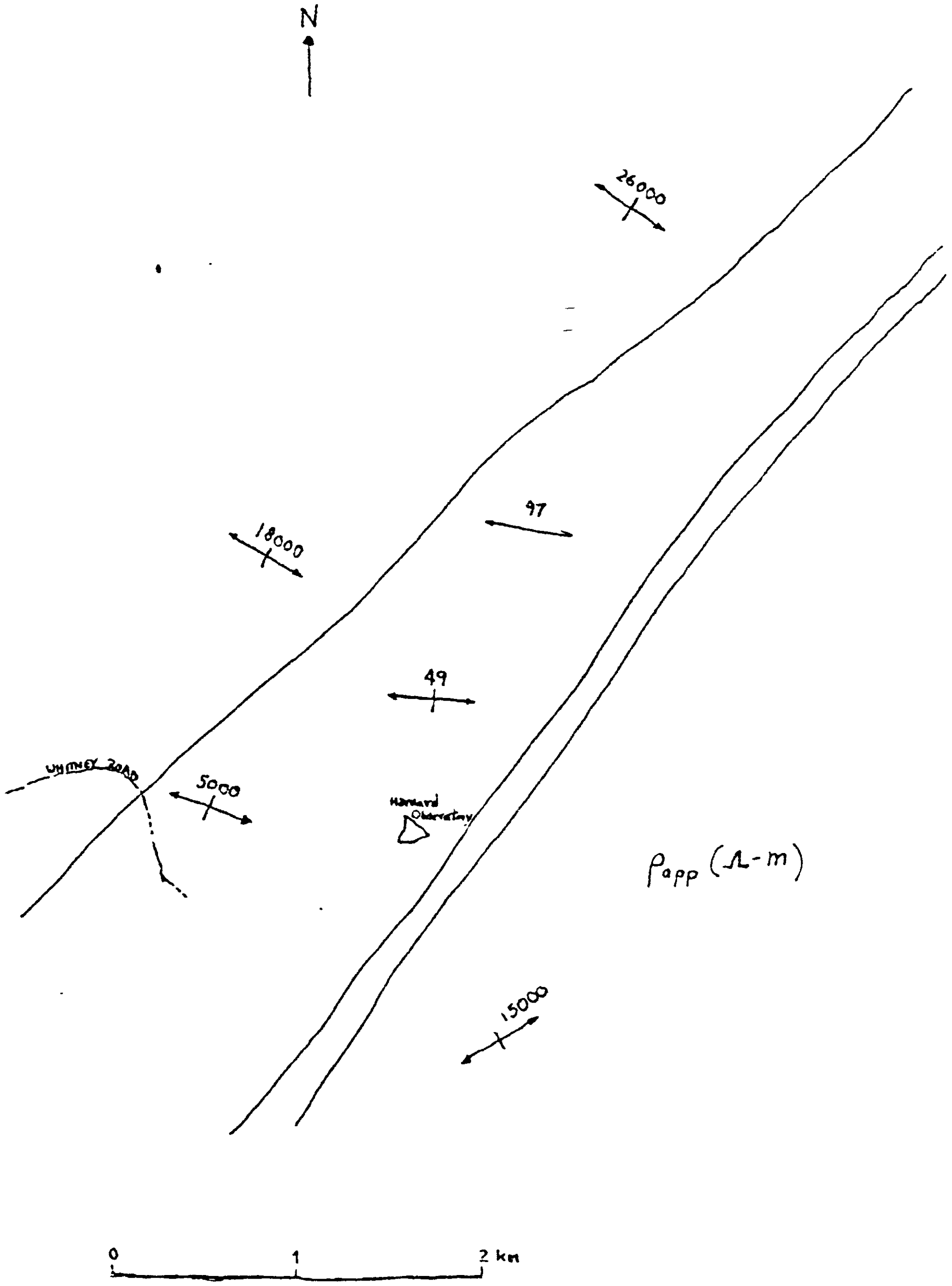

MAGNETOTELLURIC SURVEY MAP (from Davis, 1979)

FIGURE 4.6

with the realization that IP targets are generally three dimensional bodies, we developed the approximate embedded ellipsoid analysis outlined previously in this chapter and discussed in detail in Appendix D. Now let us consider the acquisition and analysis of telluric field data from the vicinity of the Harvard Observatory.

4.2.2 Data Acquisition

Near Harvard, MA we deployed an array of three dipoles as depicted in Figure 4.7. Dipole A is inside the schist approximately perpendicular to the strike or long direction of the schist. Dipole B is outside the schist also roughly perpendicular to strike. Dipole C is within the schist and oriented roughly parallel to strike. A detailed description of our field equipment and procedures can be found in Appendix A.

The telluric signals were amplified and filtered in the 10-120 second band and digitized at a 1 second sampling period. our data contained noise due to nearby power lines, road traffic, and particularly high self potentials at the electrode sites. We were plagued by a much higher degree of cultural noise at our site in surburban Harvard than at measurement sites in desert and farming regions in California. The local power ground for a high voltage line was located near our center electrode. Rectification of current through this ground may have caused the high self potential noise we measured.

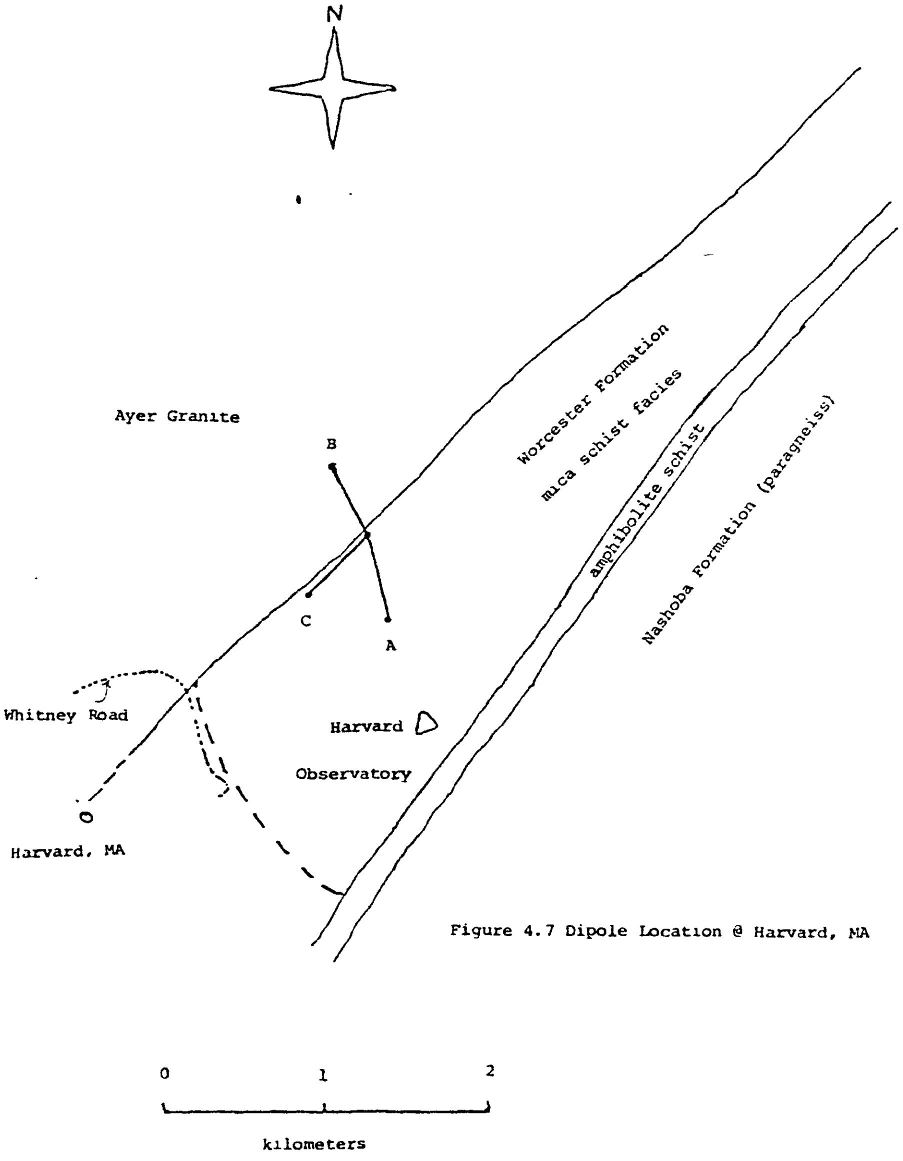

Figure 4.7 Dipole Location @ Harvard, MA

Additionally, as much as 5 volts AC was measured between electrodes separated by 500 meters. which required strong suppression of the AC in our input circuitry to prevent saturation of our amplifiers.

The noise in the records was limited to a few points or was impulsive decaying at the rate of the filter time constant. An example of a recording with high coherency between signals is given as Figure 4.8 and an unacceptably noisy recording is shown as Figure 4.9. Both recordings consist of three signals which represent electronically filtered and amplified dipole signals or combinations of dipole signals. The difference between the noise levels in the two recordings appears slight at a first glance. However the broad band coherency between signals in Figure 4.8 is .992 (12% noise) while for the signals in Figure 4.9 the coherency is .975 (23% noise).

4.2.3 Data Analysis

Our aim in the analysis of the telluric data was to infer a relative frequency dependence between telluric fields inside and outside of the schist of 10-20% per decade of frequency. When the noise levels or incoherencies between these signals approached or exceeded their expected frequency dependences, we could not differentiate between noise and relative frequency dependence. Consequently, we were able to infer reliable estimates of the eigenstate frequency dependences for only

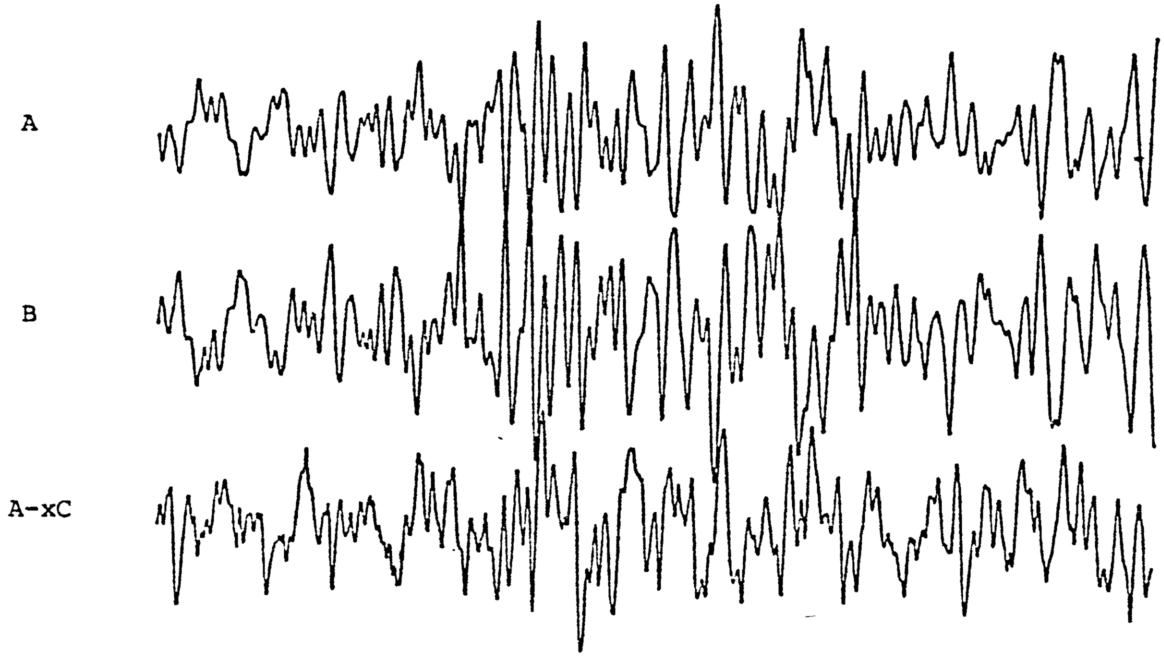

Figure 4.8 High Coherency Recording

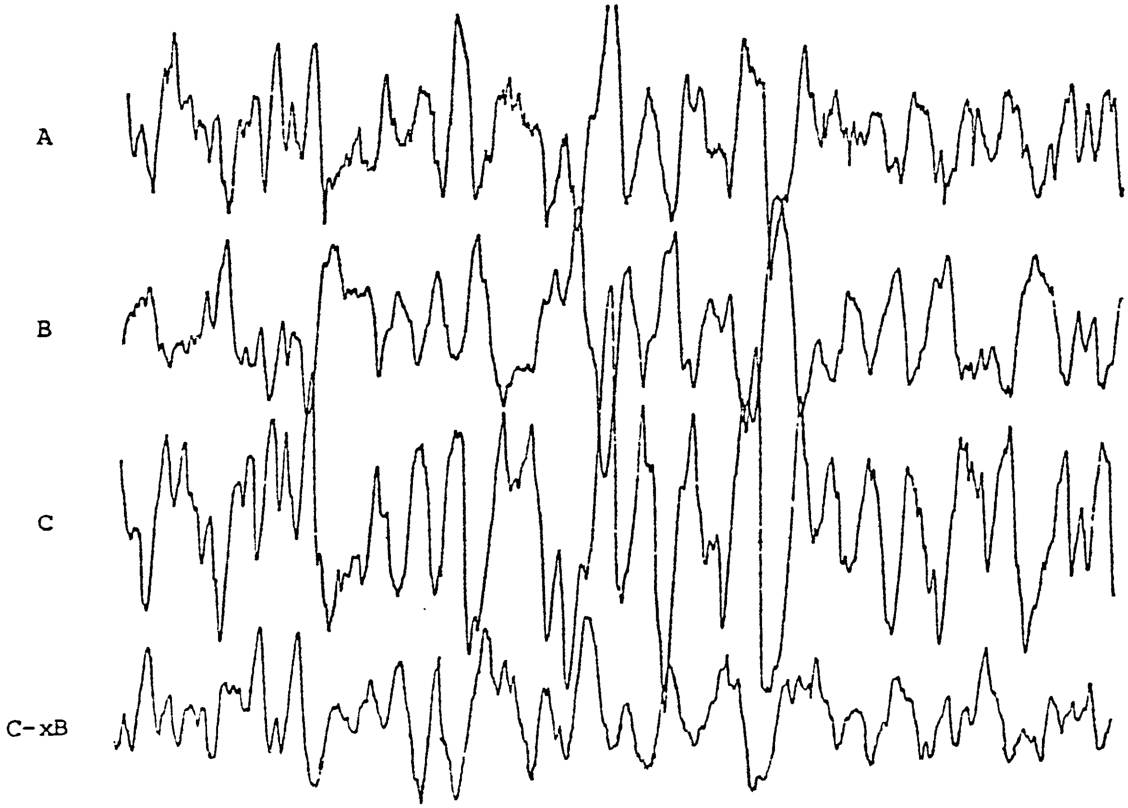

Figure 4.9 Low Coherency Recording

one set of recordings.

Two numerical approaches can be used to infer the frequency dependence of the telluric tensor. The data can be transformed to the frequency domain and the real tensor elements calculated as a function of frequency in the least squares sense. Alternatively. constant Q digital filters can be applied to the recorded time series and the tensor elements estimated in the least squares sense for each band. For both domains the coherency between the tensor prediction of one dipole signal and the actual signal was used as a measure of goodness of fit. We tried both approaches but ultimately used the filtered time series approach because we could accomplish noise suppression simply by the removal of incoherent data points. Noise suppression in the frequency domain was more complicated. Least squares time domain analysis is described in detail in Appendix C. Let us present now a simple example of how we estimate and reduce the noise in the elements of our telluric tensors.

We seek a least squares solution to the equation:

$$B_{pred}\,(t_i) = a\,A(t_i) + c\,C(t_i) \qquad i=1 \text{ to } N \qquad (4\text{-}2)$$

which relates the dipole signals A and C to dipole B oriented as in Figure 4.7. The three dipole time series can be thought of as column vectors of length N. In terms of the dot products between these column vectors, a least squares solution for the tensor elements a and c is of the form:

$$\begin{bmatrix} a \\ c \end{bmatrix} = \begin{bmatrix} A\cdot A & A\cdot C \\ C\cdot A & C\cdot C \end{bmatrix} \begin{bmatrix} A\cdot B \\ C\cdot B \end{bmatrix} \qquad (4 - 3)$$

The coherency between the prediction of signal B (Bpred) and the actual signal B is determined with the equation:

$$\mathrm{coh}(B\cdot B_{pred}) = \frac{B\cdot B_{pred}}{\left\{(B\cdot B)(B_{pred}\cdot B_{pred})\right\}^{1/2}} \qquad (4 - 4)$$

For the Harvard, MA data, we calculated the tensor elements and coherency (equation 4-1) for the complete frequency band. With these tensor estimates, we isolated spuriously noisy data points which we replaced with a spline fit. With this initial noise suppression, we filtered the data in four bands and recalculated the tensor elements and coherencies. We then discarded data points for which the error in the least squares fit exceeded a predetermined value. With this reduced data set, we recomputed the tensor values and coherencies and iterated on this procedure reducing the acceptable least squares error with each step. The iterations were stopped when the percentage reduction in the number of points exceeded the percentage reduction in noise level or incoherency. Typically. more than half the data points were used in the last iteration and the coherency improved from an initial value of approximately .992 to better than .998 for the final iteration. The tensor values from the final iteration were rotated to a Cartesian coordinate system (X.Y) whose axes aligned perpendicular and parallel to dipole C. The eigenstates were then calculated for each frequency band. A plot of the eigenvalues versus frequency for our most coherent recording (HV296) is presented as Figure 4.10 and the eigenvector orientations are shown as Figure 4.11. From Figures 4.10 and 4.11. we notice that the larger eigenvalue is consistent with a more than 50 to 1 conductivity contrast between the schist and the surrounding granite and the smaller eigenvalue is consistent with some heterogeneity along the strike of the schist. Both eigenvalues exhibit frequency dependence consistent with the presence of an IP target. In fact, the telluric tensor frequency dependence is greater than the 10%/decade frequency dependence inferred from active source measurements at 10 and 1 second periods. The smaller IP effect for active source measurements may be caused by the presence of a pyrite free weathered surface layer over the schist that has little effect on the telluric field but can dilute the frequency dependence of the active source measurements. Alternatively. the

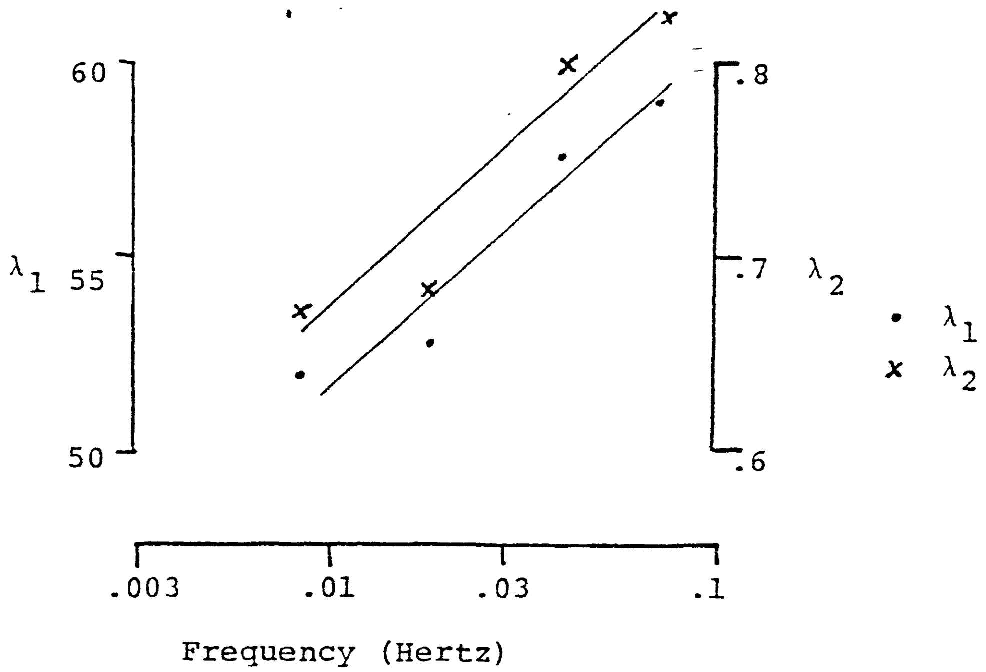

Figure 4.10 Eigenvalue frequency dependence for Harvard, Mass telluric data.

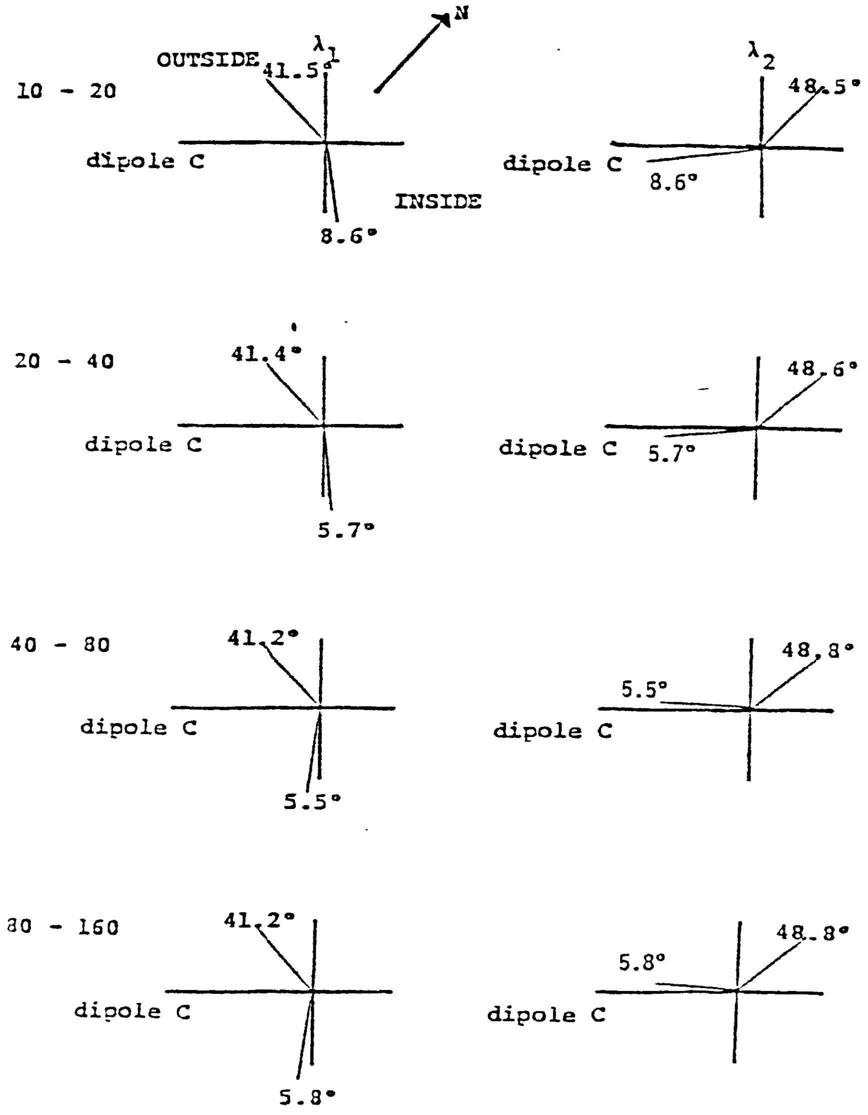

Figure 4.11 Eigenvector directions versus frequency

increased IP effect at the lower telluric frequencies is consistent with laboratory measurements on pyrite by Morgan (1981).

We notice also that the frequency dependence of the eigenvalues is consistent with the ellipsoidal models of a prolate IP target but unlike the ellipsoid model. the corresponding eigenvectors inside and outside the schist not only vary with frequency but also are not parallel. This variation in the principal axis directions with frequency could be due either to noise in the data causing uncertainty in the eigenvector estimates or to local heterogeneity within the schist. Another possibility is that dipoles B and C may have spanned the boundary of the schist and their signals exhibited a mixture of the internal and external frequency dependences.

The most significant points of this example are that consistent with Madden's hypothesis (1979). we were able to infer a frequency dependence in the telluric tensor for fields in and near an IP target. Additionally, consistent with Morgan's observations, the low frequency end of the telluric spectrum may be helpful in discriminating between the presence of pyrite and copper sulfide deposits. To add credence to our IP field studies, we applied a similar analysis to telluric measurements near Salinas. CA where no IP effects were either expected or found.

4.3 Telluric Field Measurements near Salinas, CA

We present in this section, an analysis of a telluric tensor relating fields measured near the site in Salinas. CA depicted in Figure 4.12. The small scale array is within 10 miles of the Pacific ocean and involves 3 dipoles less than one kilometer in length. Near coastlines the telluric field is dictated largely by the ocean and tends to be linearly polarized. This tendency toward linear polarization can be seen in a 1024 second long recording of the dipole signals presented as Figure 4.13.

Applying the same procedures described in the previous section, we computed the tensor and tensor eigenstates plotted in Figures 4.14 and 4.15. Figure 4.14 is a plot of the tensor eigenvalues versus frequency and Figure 4.15 is a plot of the frequency independent eigenvector directions. This lack of frequency dependence is consistent with the absence of an IP target and the short dipole lengths used and, in fact, should be typical of small scale telluric tensor analyses. The data sets used in this example were extremely coherent. Typically the coherency between the predicted and actual fields was greater than .9995 and unlike the IP example little noise suppression was required.

4.4 Summary and Conclusions

4.4.1 Summary

Figure 4.12 Location Map for Salinas, CA

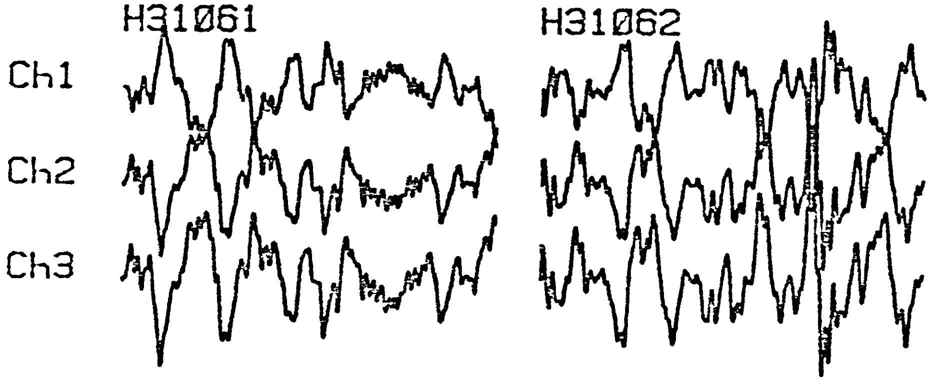

Figure 4.13 Salinas Telluric Data

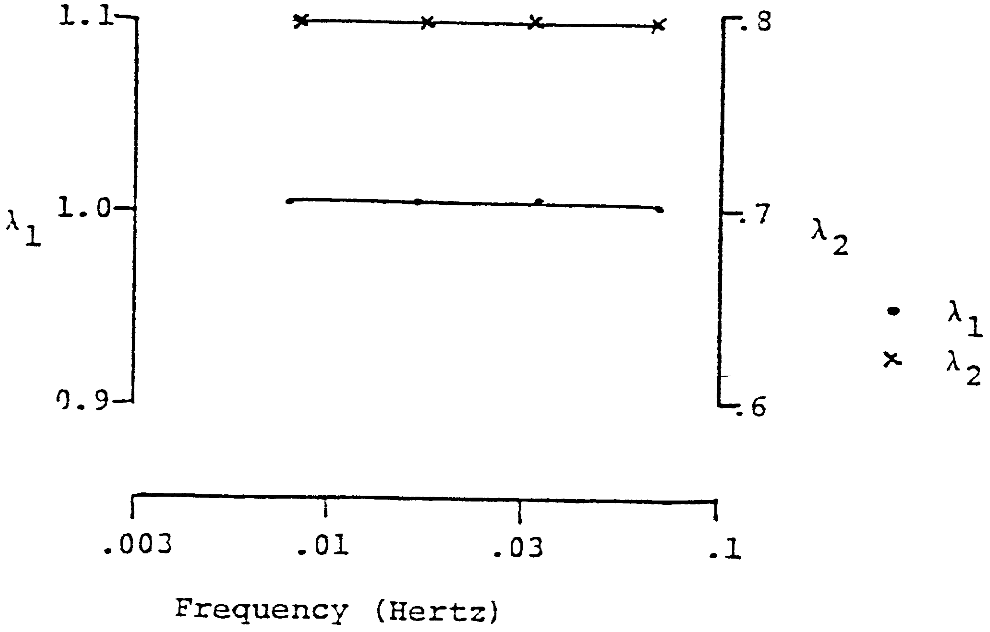

Figure 4.14 Eigenvalue frequency dependence for Salinas, California data.

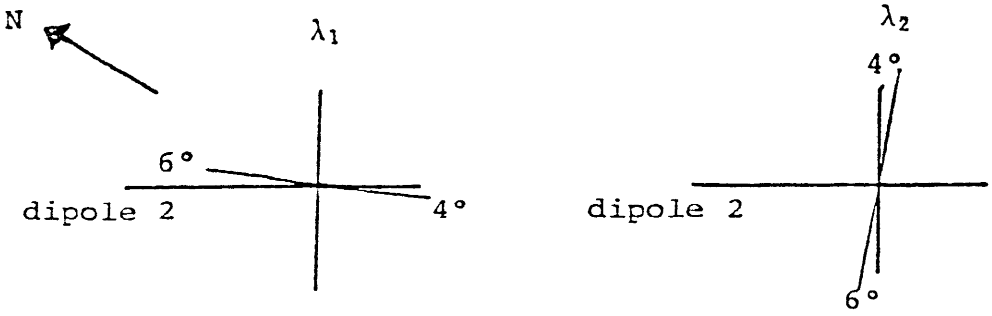

Figure 4.15 Eigenvector directions for Salinas site

In this chapter. we have presented an approximate model of the low frequency telluric field response to an embedded ellipsoidal IP target (ore body) and have described an experimental procedure for measuring the telluric fields necessary to determine the frequency dependent eigenstates of the telluric tensor in the vicinity of such an IP target. We have applied the eigenstate analysis of Chapter 2 to telluric data from two sites; one near an IP target and the other far from any known IP targets. We have inferred a frequency dependence for the tensor eigenstates consistent with the presence of an IP target at the first site and found no such frequency dependence at the second site.

4.4.2 Conclusions

We conclude from our studies that the use of the telluric field and the telluric tensor eigenstate analysis as a prospecting tool for the inference of IP targets shows considerable promise. We feel that more extensive studies are necessary to determine the generality of this approach and explore the possibility of differentiating between pyrite and copper sulfide targets.

We find that the ellipsoidal model of an IP target is a qualitatively useful tool for predicting the eigenstate frequency dependences but its quantitative applicability appears limited to simple geological formations.

Finally, we feel that the ease at which noise can be removed using the time domain analysis along with the requirement of highly coherent signals makes the filtered time series approach preferable to frequency domain analysis.

CHAPTER 5

Thesis Summary and Extensions

5.0 Summary

We have sought to apply the concept of differential tellurics to infer geophysical information from the fine structure of the telluric field. We have found the small frequency dependence in the fine structure of local telluric field measurements to be consistent with the presence of an IP target. We have ascertained that the stability of differential telluric measurements is a sensitive measure of the stability of the conductance of the crust and have determined that the sensitivity is dependent on the degree of current saturation.

We have obtained considerable insight into the telluric field fine structure with the shifted eigenvalue analysis of Lanczos(1961). We can separate the telluric tensor relationships into two natural modes modes representing the structurally imposed maximum and minimum electric field directions and use the skew of the tensor as a measure of the spatial variation of these directions. Thus, with the eigenstate analysis, we can study the fine structure of the telluric field in terms of a few parameters which are reflections of the physical properties of the earth. The application of the Lanczos analysis to the impedance tensor also has yielded insights into the electromagnetic response of the earth.

Consistent with the heterogeneous nature of the earth, the electric and magnetic eigenstates need not be orthogonal. The skew considered usually as a "three dimensional parameter", can be interpreted as the structurally imposed deviation of the electric and magnetic fields from perpendicularity.

In our studies of the stress sensitivity of differential telluric measurements, we have considered source frequencies low enough that the telluric tensor relationships are independent of frequency even for large measurement separations over varied crustal structure. Additionally, in our IP studies we have considered measurement separations small enough that any frequency dependence in the telluric field fine structure could be attributed to a local feature whose conductivity is frequency dependent. Thus, the sensitivity study represents the low frequency limit for telluric tensor relationships while the IP study represents the limiting case of small separations between measurements. In the next section, we describe our progress in the study of the fine structure of the telluric field for frequencies high enough and separations large enough that the frequency dependence of the telluric tensor is a measure of the change in upper crustal atructure between telluric measurements.

5.1 Lateral Variations in Crustal Conductivity

For frequencies greater than about .1 Hz, the ratio of upper crustal thickness to skin depth can no longer be considered small and the frequency dependence of the telluric field becomes a function of position. For example, in conductive regions the telluric currents will start to "skin out" at lower frequencies than in resistive regions and differential telluric measurements between these regions will exhibit the difference between the frequency responses. As described in Appendix D, the telluric current system can be separated into poloidal and toroidal modes. Both current systems contribute to the surface field and both modes are generally frequency dependent. At low frequencies, the poloidal mode is the dominant contributor to the surface field and the frequency dependence of large scale differential telluric measurements can be attributed to the skinning out of the poloidal currents. At frequencies high enough that the thin sheet approximation begins to break down, the tensor eigenstates relating separated field measurements will exhibit amplitude variations with frequency with little associated phase shift. Minimal phase shifts are expected initially with the poloidal mode because the low frequency phase at each telluric site is set largely by the mantle conductivity which is not known to vary rapidly with position on the earth's surface. The eigenvalue phase can be as much as 45 degrees for the limiting case when the telluric field at one site is completely skinned out while the telluric field at another measurement site is sensitive only to the crustal conductance. At low frequencies, then, the telluric tensor is real, independent of frequency and a measure of the crustal conductance. At higher frequencies, the telluric tensor is frequency dependent and tends to be real. At even higher frequencies, the telluric tensor tends to be complex and is set by the apparent conductivity of the upper crust. The transition between these regimes, then, should be diagnostic of the relative thickness and conductivity of the upper crust.

Using the Hollister and Palmdale array dipoles, we have measured the telluric fields for frequencies up to .3 Hz and applied the telluric cancellation scheme to determine the tensor relationships between dipoles. An example of the cancellation signals is given as Figure 5.1. Notice that as the degree of cancellation is increased, the resultant residual signal contains increasing levels of high frequencies consistent with a relative change in crustal conductivity under the measurement dipoles. We suggest that with such data, we should be able to get both estimates of the contrast in crustal conductance and the contrast in apparent conductivity under the dipole measurements. From these estimates, we should be able to infer spatial variations in the conductivity and upper crustal thickness and suggest further study on this subject. In the next section, we make specific suggestions for future study in

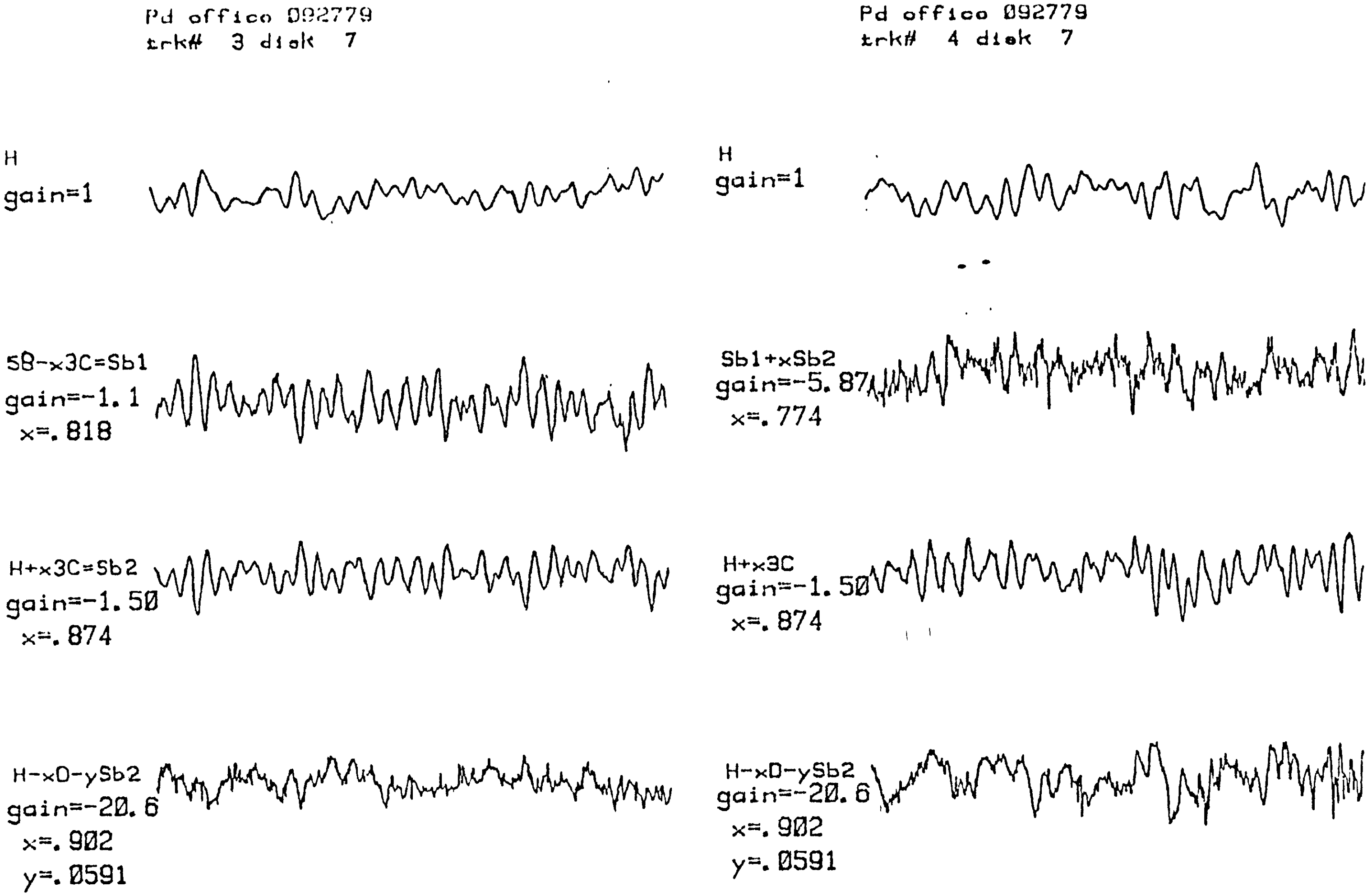

Figure 5.1 High Frequency Cancellations 1024 second sweeps

the application of differential tellurics to resistivity monitoring and IP prospecting as well as consider further the application of eigenstate analysis to the impedance tensor.

5.2 Future Studies

In Chapter 2, we have proposed the use of the eigenstate formulation to represent succinctly the properties of the telluric and magnetotelluric tensors. How to interpret the ellipticity of the impedance eigenvectors is still problematic. One possibility is that the ellipticity represents induction effects in the vicinity of large vertical magnetic fields. Further consideration should be given to this interpretation, however.

In Chapter 3, we have presented our study of the sensitivity of differential telluric measurements in the Palmdale region of southern California. We have begun studies of Madden's Hollister array but the work is not yet finished. We have suggested that the inference from telluric measurements as to where a stress change has occurred is not unique but further consideration should be given to this problem.

Studies of the stability of small scale differential telluric measurements have been initiated by Prof. Madden. Such small scale measurements are portable and can be deployed rapidly. From preliminary studies of the sensitivities of small scale measurements, we feel that the skew of the telluric tensor should be the most sensitive tensor parameter to stress changes, because of the anisotropic response of local heterogeneities to deviatoric stress.

In Chapter 4, we have presented the results of our inference of an IP target from the fine structure in the telluric field. We have presented only one result from an IP zone and feel that more field studies should be conducted. We have noted that the eigenvectors associated with our IP target, a pyritic schist, vary with frequency while the eigenvectors associated with the surrounding granites are invariant with frequency (Figure 4.12). We interpret the frequency dependence of the schist eigenvectors as a manifestation of an anisotropy in the conductivity of the schist but feel that further study is warranted.

Another approach to using differential tellurics to infer the presence of IP targets is to establish a base telluric station and a roving telluric station (Berdichevskii,1960) and through a telemetry link monitor tellurics simultaneously from both stations. With such an approach, we should be able to detect the presence of an IP target even when the roving station is within the effective boundaries of the IP target. Further study is warranted here as well.

REFERENCES

Aki,K. and P. Richards,(1980), QUANTITATIVE SEISMOLOGY, Theory and Methods,W.H. Freeman and Co.,pp 932.

Babour,K.,J. Mosnier,M.Daignieres,G.Vasseur,J.L. LeMouel and J. Rossignol,(1976), A geomagnetic variation anomaly in the Northern Pyrenees, Geophys. J. R. astr. Soc.,45,pp583-600.

Babour,K. and J.,Mosnier,(1979), Differential geomagnetic sounding in the Rhinegraben, Geophys. J.R. astr.Soc.,58,135-144.

Berdichevskii, M.N.,(1960), Electrical surveying by means of telluric currents: Moscow, Gostoptekhizdat. Translation by G. Keller 1965, Quarterly of the Colorado School of Mines, v.60,No.1.

Bostick,F.S.,and H.W. Smith,(1962), Investigation of large-scale inhomogeneities in the earth by the magnetotelluric method, Proc. IRE, vol. 50, pp 2339-2346.

Cagniard,L.,(1953), Basic Theory of the magnetotelluric method of prospecting, Geophysics,vol. 18, pp605-635.

Cantwell,T.,(1960), Detection and analysis of low frequency magnetotelluric signals, Phd thesis,MIT.

Cantwell,T and T.R. Madden,(1967), Induced Polarization, A Review, SEG Mining Geophysics, Vol. II,Theory,pp373-400.

Carslaw, H.S. and J.C. Jaeger,(1959),Conduction of Heat in Solids, Oxford University Press.510 p.

Claerbout, Jon F.,93(1976),Fundamentals of Geophysical Data Processing with applications to petroleum prospecting, McGraw Hill,1976,274p.

Davis, R.A.,(1979), A bandlimited magnetotelluric study of an area in Harvard, MA., Ms. Thesis, MIT.

Diblee,T.W.,(1967), Areal Geology of the western Mojave Desert, California: U.S. Geol. Survey Prof. Paper 522, pp 153.

d'Erceville,I. and G. Kunetz,(1962), The effect of a fault on the earth's natural electromagnetic field, Geophysics,vol. 27, pp 651-665.

Hanna,W.F.,J.Rietman, and S. Biehler,(1975), Bouguer Gravity Map of California, Los Angeles Sheet.

Jackson, John D.,Classical Electrodynamics, Wiley and Sons, NY, 1962, pp 641.

Kasameyer, P.W.,Low frequency magnetotelluric survey of New England, Phd thesis, MIT, 1974.

Kaufmann,A.A.,(1978a),Frequency and transient responses of the electromagnetic fields created by currents in confined conductors,Geophysics,vol.42,No.5,pp1002-1010.

Kaufmann,A.A.,(1978b),Resolving capabilities of the inductive methods of electroprospecting,Geophysics,vol.43,No.7,pp1392-1398.

Kaufmann,A.A.,(1979),Harmonic and transient fields on the surface of a two layer medium,Geophysics,vol.44,No.7,pp1208-1217.

Lanczos,C.,(1958),Applied Analysis,Prentice Hall,539p.

Lanczos,C.,(1961),Linear Differential Operators,Van Nostrand.

Lee,T.C.,(1977),Telluric anomalies caused by shallow structures: Ellipsoidal approximations,Geophysics,vol.42,No.1,pp97-102

Madden,T.R. and P. Nelson,(1964), A defense of Cagniard's magnetotelluric method, ONR Project NR-371-401, Geophysics Lab.,MIT.

Madden,T.R.,(1976), Resistivity Variations and Self Potential Measurements using Telluric Field Cancellation Methods Special Technical Report to the USGS Dept. of Earthquake Hazards, Menlo Park,CA, June.

Madden,T.R.,(1978),Electrical Measurements as Stress-Strain Monitors, Procedings of Conference VII on Stress Strain Measurements Related to Earthquake Prediction, USGS Open-File Report 79-370, September.

Madden,T.R.,(1979), Induced Polarization Measurements with Tellurics, Oral Presentation to the First Biennial Conference of the Australian SEG, August.

Ness, N.F.,(1959), Resistivity Interpretation in Geophysical Prospecting, Phd Thesis, MIT.

Price, A.T.,(1949), The induction of electric currents in non-uniform thin sheets and shells, Quart. J. Mech. Appl. Math.,2, pp 263-310.

Ranganayaki,R and T. Madden,(1979),Generalized thin sheet analysis in magnetotellurics: an extension of Price's analysis, Geophys. J. R. astr. Soc.,

Reddy,I.K.,R. Philips,J. Whitcomb, and D.Rankin,(1977), Electrical Structure in a Region of the Transverse Ranges, Southern California, Earth and Planetary Sciences Letters, 34, p313-320.

Swift,C.M.,(1967), A Magnetotelluric Investigation of an Electrical Conductivity Anomaly in the Southwestern United States. Phd thesis, MIT,pp 211.

APPENDIX A

Field Equipment and Procedures

A.1 Field Equipment

Small scale telluric signals are obtained by measuring the voltage difference between two electrodes in contact with the earth and separated by distances the order of a kilometer. As a minimum three dipole signals are measured, usually with dipoles approximately orthogonal as depicted in Figure A-1.

The electrodes are made of silver mesh coated with silver chloride immersed in a saturated solution of potassium chloride and enclosed in a porous pot. Each electrode pair or dipole is buffered by a low noise instrumentation amplifier with a variable gain of 1.2 to 201 followed by a 500 sec high pass filter with a gain of 10 as shown schematically in Figure A-2. The consequent dipoles signals are then cancelled with DC amplifiers combining a fraction of one signal with another then combining these scalar signals in a similar manner to form a tensor cancellation as depicted in Figure A-1.

The output or residual of these cancellations is then filtered and amplified before being recorded on a digital acquisition system designed and constructed by Tibor Lukac and packaged for field use by Steve Park. Figure A-3 is the schematic of the two pole Bessel filters used to amplify the telluric signals in the band 120 to 10 seconds. Our data acquisition system was designed for direct data transfer to our computer system a Hewlett Packard 9825T desktop computer with which data analysis was performed.

To measure magnetic fields we use the magnetic coils built for and described by Cantwell(1960) and packaged in PVC pipe by Bob Davis(1979). The coils are five and six feet long with 90,000 turns of magnet wire on a cylindrical core of high magnetic permeability. The coil constants are, respectively, for the long and short coils:

3.51 gammas/mv/Hz (long coil)
5.37 gammas/mv/Hz (short coil)

The coil outputs tend to be a fraction of a microvolt in the 10 to 100 second periods and preamplification is accomplished by the use of the low noise chopper stabilized operational amplifier circuit drawn schematically as Figure A-4. All of the electronics were battery operated.

A.2 Telluric Field Measurements

To obtain the three or four dipole signals necessary to perform telluric cancellations long wires are laid out to connect distant electrodes to the centrally located circuitry. We have used number 22 magnet wire as well as PVC coated number 28 stranded copper wire for this purpose. To minimize electric field noise induced by motion of the wire in the earth's magnetic field, care is taken the keep the wire on the ground. The need for immobilizing the dipole wire can be seen with a simple calculation. A 100 second oscillation of 5 centimeters over a 5 meter length of wire in a 40,000 gamma field will produce a 10 microvolt noise signal on the wire. Since the typical electric fields are approximately 1 mv/km for 100 second periods, 10 microvolts represents 1% amplitude noise. Other major sources of telluric noise are from the measuring electrodes themselves or from local self potentials affecting the electrodes. To minimize electrode noise we use the following procedures. All electrodes to be used in the measurements are inspected for proper plating (indicated usually by a grey-black coating on the silver mesh) and tested in a pit for consistency in potential and impedance before being installed in the field. At each electrode site a pit approximately 30 cm deep is dug and saturated with water . A local (1meter) SP survey is made around the electrode pit. After installation of the electrode , the pit is covered to minimize drying of the soil around the electrode and temperature variations. Additionally , when possible, each electrode is left in its hole overnight to allow for chemical equilibration with its surroundings.

A.3 Magnetic Field Measurements

Potentials can be induced at the output of the magnetic coils by relative motion of their ends in the earth's magnetic field (a v X B term). More importantly, moving vehicles within a hundred meters of our coils can cause unacceptably high magnetic variations in our 10-120 second period range. Thus, the coils must be placed in stable positions as far from automobile and pedestrian traffic as possible. To this end, we buried the coils at distances of 50-100 meters from our recording equipment and as far from existing roads as possible. The need for large separations between the coils and traffic can be seen also by a simple example.

Assume a vehicle to have a magnetic dipole field of 10,000 gammas at 1 meter. The typical magnetotelluric field measured at 100 seconds is less than 1 gamma. The field of a dipole decreases as the inverse cube of the separation, so that when the vehicle moves within 100 meters of the coils, a field of .01 gammas will be sensed by the coils or approximately 1% noise amplitude. The magnetic field preamp was placed near the coils (10 m) to maximize signal to noise in the long cables to the recording equipment.

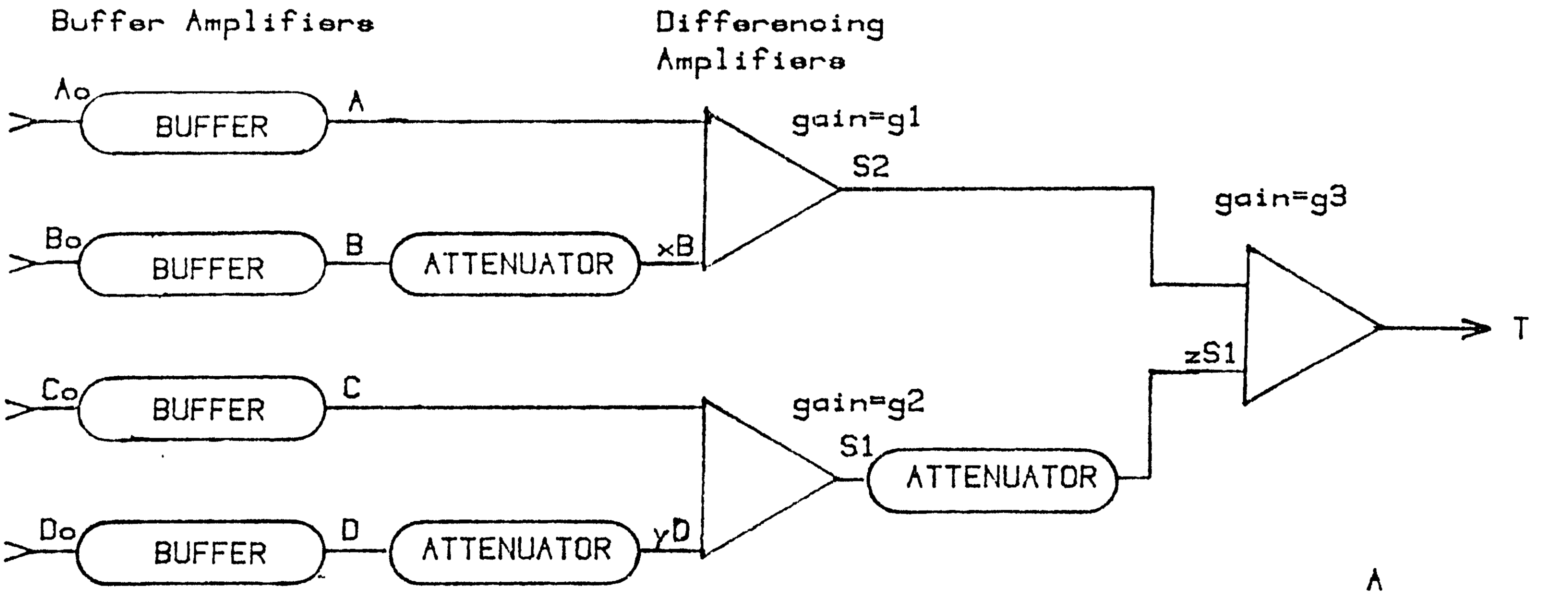

$T=g3(S2+zS1)$

$S2=g1(A+xB)$

$S1=g2(C+yD)$

ASSUMED:

$|B| > |A|$

$|D| > |C|$

$|S1| > |S2|$

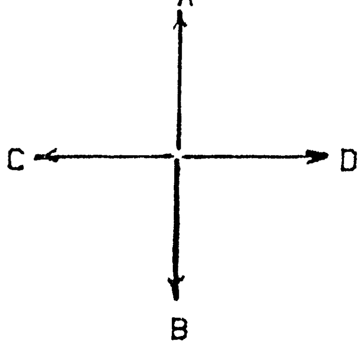

DIPOLE GEOMETRY

TELLURIC CANCELLATION SYSTEM

FIGURE A-1

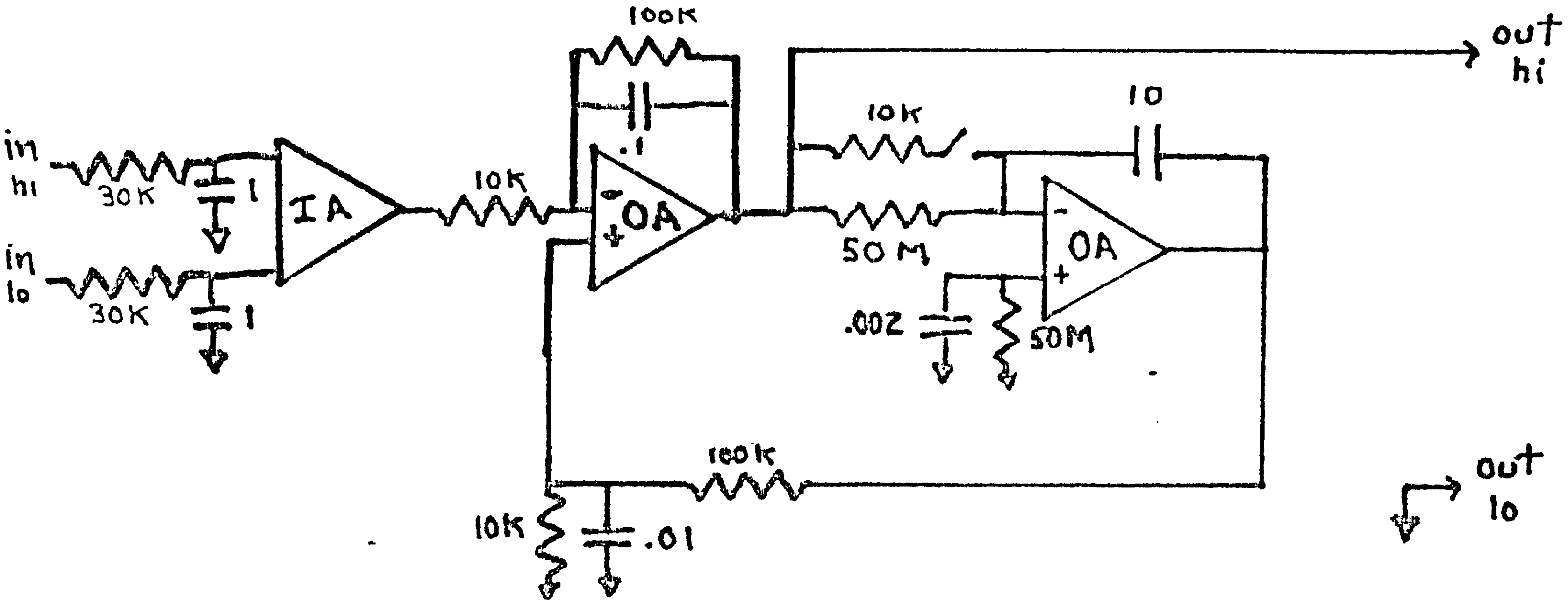

IA-instrumentation amplifier Analog AD522A

OA-operational amplifier Precision Monolithics OP-15

resistors-1% (Cermet)

capacitors <1mf 10% ceramic
≥1mf 1% (Component Research)

GAIN=10 to 1000

ELECTRIC FIELD PREAMPLIFIER

FIGURE A-2

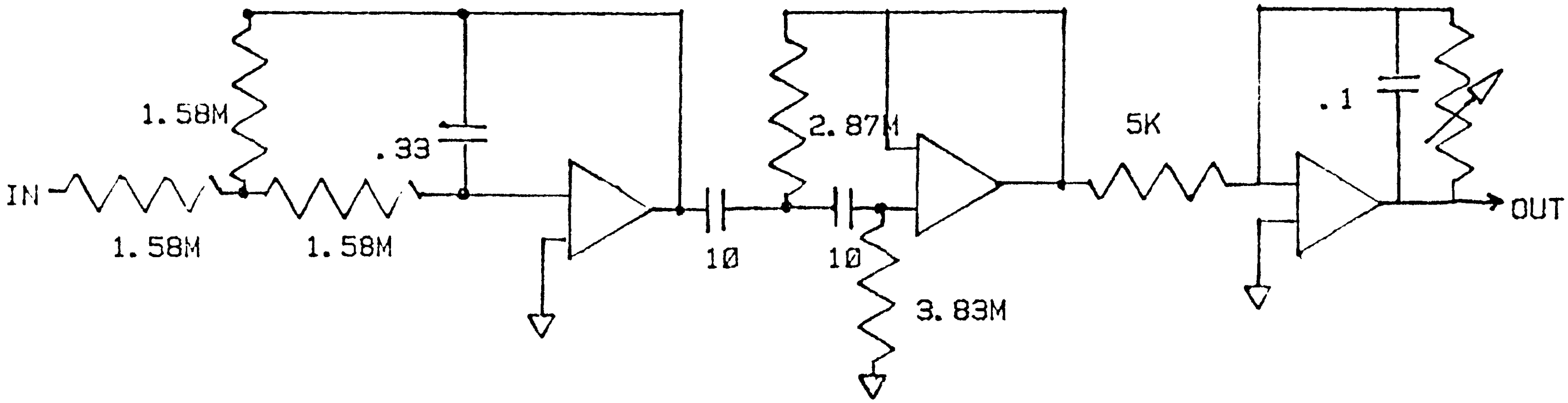

capacitors 1% (Component Research)

resistors 1% cermet

operational amplifiers Precision Monolithics OP-15 or equivalent

Bandpass 120-10 seconds, gains .2 to 200

BESSEL FILTER

FIGURE A-3

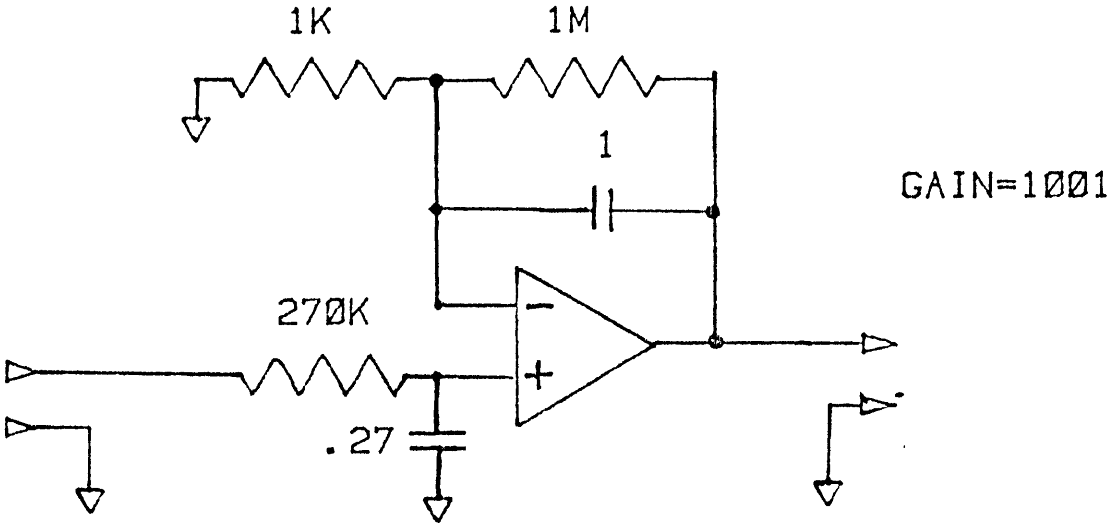

resistors 1% cermet

capacitors 1% Component Research

Chopper stabilized operational amplifier Analog (AD261K)

MAGNETIC FIELD PREAMPLIFIER

FIGURE A-4.

Appendix B

Impedance Eigenstate formalisms with a numerical example

B.0 Introduction

In this appendix we present the orthogonality relationships for the u and v space eigenvectors, establish an algebraic formalism for the eigenstates of the impedance tensor and give a numerical example of the eigenstate-calculations described in Chapter 2.

Lanczos' book "Linear Differential Operators" is out of print and difficult to locate. However, Aki and Richards (1980) have included the Lanczos analysis in their book along with a numerical example which emphasizes the utility of his analysis when applied to defective matrices. They use real matrix elements in their example and do not address the phase convention problem we discussed in Chapter 2 and describe by example in this appendix. Let us consider now the eigenvector orthogonality conditions.

B.1 Orthogonality Conditions

From Chapter 2, the eigenvalue equation is of the form:

$$S\, w = \lambda\, w \qquad \text{(B-1)}$$

where S is the augmented Hermitian matrix, (λ) is a real eigenvalue and w is the augmented eigenvector with components u and v such that:

$$S = \begin{bmatrix} & A \\ \tilde{A} & \end{bmatrix} \quad ; \quad w = \begin{bmatrix} u \\ v \end{bmatrix} \qquad \text{(B-2)}$$

Additionally, we modified equation 1 to allow the eigenvalues to be complex such that:

$$S\, w' = \begin{bmatrix} \lambda & \\ & \lambda^{*} \end{bmatrix} w' \qquad \text{(B-3)}$$

For both equations 1 and 3, any two distinct eigenvectors of S are orthogonal. Therefore:

$$\tilde{u}_i \cdot u_j + \tilde{v}_i \cdot v_j = 0 \qquad i \# j \qquad \text{(B-4)}$$

For a non zero eigenvalue (λ_i) not only does the solution to (4) (u, v, λ) exist but the solution $(u, -v, -\lambda)$ exists as well. As a consequence of the second solution:

$$\tilde{u}_i \cdot u_j - \tilde{v}_i \cdot v_j = 0 \qquad i \# j \qquad \text{(B-5)}$$

which together with (5) requires that:

$$\begin{aligned} \tilde{u}_i \cdot u_j &= 0 \\ & \qquad\qquad i \# j \qquad \text{(B-6)} \\ \tilde{v}_i \cdot v_j &= 0 \end{aligned}$$

B.2 Algebraic form of the Impedance Eigenstates

As indicated in Chapter 2, the impedance tensor in a given coordinate system X,Y with Z down can be written as:

$$Z = \begin{bmatrix} Zxx & Zxy \\ Zyx & Zyy \end{bmatrix} \qquad (2\text{-}2)$$

To establish eigenstate magnitudes and relative phases, we apply equation (2-14), rewritten below, to equation (2-2).

$$\begin{aligned} \tilde{Z}\, Z\, v &= |\lambda|^2 v \\ & \qquad\qquad (2\text{-}14) \\ Z\, \tilde{Z}\, u &= |\lambda|^2 u \end{aligned}$$

The matrix product $Z\tilde{Z}$ takes the form:

$$Z\tilde{Z} = \begin{bmatrix} |Zxx|^2 + |Zxy|^2 & ZxxZyx^* + ZxyZyy^* \\ Zxx^*Zyx + Zxy^*Zyy & |Zyx|^2 + |Zyy|^2 \end{bmatrix} \qquad (B\text{-}7)$$

Labelling the determinant of $Z\tilde{Z}$ as $\det(Z\tilde{Z})$ and defining the variable B as:

$$B = \{ |Zxx|^2 + |Zxy|^2 + |Zyx|^2 + |Zyy|^2 \}/2, \qquad (B\text{-}8)$$

the eigenvalue equation can be expressed as:

$$|\lambda|^2 = B + \{B^2 - \det(Z\tilde{Z}) \}^{\frac{1}{2}} \qquad (B\text{-}9)$$

For the degenerate model of a 1D earth:

$$Zxx = Zyy = 0 \;;\; Zxy = Zyx \qquad (B\text{-}10)$$

and the eigenvalues become:

$$|\lambda|^2 = \frac{|Zxy|^2}{|Zyx|^2} \qquad \text{(B-11)}$$

For a 2D earth:

$$Zxx = Zyy = 0 \qquad \text{(B-12)}$$

and the eigenvalues become:

$$|\lambda|^2 = \frac{|Zxy|^2}{|Zyx|^2} \qquad \text{(B-13)}$$

where Zxy and Zyx are the impedances perpendicular and parallel to the strike direction. In general, however, no simplifications occur and the eigenvalues are calculated with equation 9.

With equations 7 and 9, the unnormalized eigenvectors for the electric field take the form:

$$E_+ = \begin{bmatrix} ZxxZyx^* + ZxyZyy^* \\ \{|Zyx|^2+|Zyy|^2-|Zxx|^2-|Zxy|^2\}/2 + \{B^2 - \det(Z\tilde{Z})\}^{\frac{1}{2}} \end{bmatrix} \qquad \text{(B-14a)}$$

$$E_- = \begin{bmatrix} \{|Zxy|^2+|Zxx|^2-|Zyx|^2-|Zyy|^2\}/2 - \{B^2 - \det(Z\tilde{Z})\}^{\frac{1}{2}} \\ Zxx^*Zyx + Zxy^*Zyy \end{bmatrix} \qquad \text{(B-14b)}$$

Similarly, the unnormalized eigenvectors for the magnetic field have the form:

$$H_+ = \begin{bmatrix} Zxx^*Zxy + Zyx^*Zyy \\ \{|Zxy|^2+|Zyy|^2-|Zxx|^2-|Zyx|^2\}/2 + \{B^2 - \det(\tilde{Z}Z)\}^{\frac{1}{2}} \end{bmatrix} \qquad \text{(B-15a)}$$

$$H_- = \left[\frac{\{|Zxx|^2+|Zyx|^2-|Zxy|^2-|Zyy|^2\}/2 - \{B^2-\det(\tilde{Z}Z)\}^{1/2}}{ZxxZxy^*+ZyxZyy^*} \right] \quad (B-15b)$$

where the eigenvalues are calculated with equation 9. The eigenvectors paired with each eigenvalue are:

$$\begin{aligned} &H_+,\ E_+ \text{ with } \lambda_+ \\ &H_-,\ E_- \text{ with } \lambda_- \end{aligned} \quad (B-16)$$

and consistent with equation 6:

$$\begin{aligned} H_+\cdot H_- &= 0 \\ E_+\cdot E_- &= 0 \end{aligned} \quad (B-17)$$

but the E and H eigenvectors need not be orthogonal to each other. In the next section, we present a numerical example illustrating our eigenstate procedures and conventions.

B.3 A numerical example of the eigenstate formulation

Let us consider the eigenstates for the following impedance tensor.

$$Z = \begin{bmatrix} .4314\exp(-i68.29) & 5.481\exp(-i57.34) \\ 7.896\exp(i113.46) & .9775\exp(-i58.57) \end{bmatrix} \quad (B-18)$$

Forming the matrix products necessary to determine the eigenstates we find:

$$\tilde{Z}Z = \begin{bmatrix} 62.53 & -5.359\exp(+i6.65) \\ -5.359\exp(-i6.65) & 31.00 \end{bmatrix} \quad (B-19)$$

$$\tilde{ZZ} = \begin{bmatrix} 30.23 & 1.964\exp(+i6.40^\circ) \\ 1.964\exp(-i6.40^\circ) & 63.30 \end{bmatrix} \qquad (B-20)$$

From application of equation (2-14), we find the magnitudes of the eigenvalues to be:

$$|\lambda_1| = 7.964 \qquad |\lambda_2| = 5.488 \qquad (B-21)$$

Again using equation (2-14), we find the ratios of the eigenvector components to be:

$$\frac{V_{1x}}{V_{1y}} = -5.896\, e^{i6.65^\circ} \qquad \frac{V_{2x}}{V_{2y}} = .1653\, e^{i6.65^\circ}$$
$$\frac{U_{1x}}{U_{1y}} = .05917\, e^{i6.40^\circ} \qquad \frac{U_{2x}}{U_{2y}} = -16.90\, e^{i6.40^\circ} \qquad (B-22)$$

With equation 22, the eigenvector component magnitudes are found. To assign the signs and phases to the eigenvector components, we must choose arbitrarily the form of one eigenvector. Then, the remaining eigenvectors can be determined from the orthogonality conditions and Poynting vector requirements.

We consider first the v_1 eigenvector and choose to associate the phase difference and negative sign of equation 22 with the Y component. With these initial assignments, both the X and Y components of u_1 must be negative to satisfy the Poynting vector requirements:

$$\mathrm{Re}\{u \times v^*\} > 0 \qquad (B-23)$$

for Z positive down. Allowing for the phase shift required to put v_1 at the peak of its polarization ellipse at $t=0$, we find v_1 to be of the form:

$$v_{1x} = +.9863\, e^{-i\beta_0^{\circ}}$$
$$V_{1y} = -.1648\, e^{-i(6.65-\beta_0)^{\circ}} \qquad \text{(B-24)}$$

where $\beta_0 = \omega t_0$. To find β_0 and the sense of rotation of the v_1 polarization ellipse, we need to determine first the time domain form of the complex vector v_1. Then, following a procedure outlined by Eggers(1981) we find the time at which the magnitude $v_1(t)$ is a maximum and noting the eigenvector position at β_0 and $\beta_0 + \pi/2$, we find the sense of rotation of v_1.

The frequency domain representation of v_1 can be written as:

$$v_1 = a + i\, b \qquad \text{(B-25)}$$

where a and b are vectors in the X,Y coordinate system. The time domain representation of v_1 is:

$$\begin{aligned} v_1(t) &= \mathrm{Re}\{\exp(-i\omega t)[a + ib] \\ &= a\cos(\omega t) + b\sin(\omega t) \end{aligned} \qquad \text{(B-26)}$$

Taking the derivative of the squared magnitude of $v_1(t)$ with respect to (ωt) we find that the phase shift (ωt_0) for which $v_1(t)$ is at the maximum of its polarization ellipse can be calculated with the equation:

$$\tan(2\omega t) = 2\, a \cdot b / (\, |a|^2 - |b|^2\,) \qquad \text{(B-27)}$$

Applying equations 25-27 to equation 24, we find the phase shift β_0 to be:

$$\beta_0 = \omega t_0 = -.18 \text{ degrees} \qquad \text{(B-28)}$$

and the final form for v_1 is:

$$V_{1x} = +.9863 \exp(+i.18)^{\circ}$$
$$V_{1y} = -.1648 \exp(-i6.47)^{\circ} \qquad \text{(B-29)}$$

Following similar procedures for finding the phase of v_2 at its polarization ellipse maximum and requiring v_1 and v_2 to be Hermitianally orthogonal, we find v_2 to be:

$$V_{2x} = .1648 \exp(+i6.47^{\circ})$$
$$V_{2y} = .9863 \exp(-i.18)^{\circ} \qquad \text{(B-30)}$$

Consistent with equation 23, we calculate the u_1 components and assign the ellipticity phase to the X component which causes the u_1 and v_1 eigenvectors to rotate in the same direction about their respective polarization ellipses. As a result of this phase assignment, u_2 and v_2 also have the same sense of rotation. The phase at the polarization maximum is found to be essentially zero and u_1 can be written as:

$$u_{1x} = -.05907 \exp(+i6.40^{\circ})$$
$$u_{1y} = -.9983 \qquad \text{(B-31)}$$

Similarly, u_2 is found to be:

$$u_{2x} = +.9983$$
$$u_{2y} = -.05907 \exp(-i6.40^{\circ}) \qquad \text{(B-32)}$$

To calculate the eigenvalue phases, we apply equation (2-13) such that:

$$Z\, v_i = |\lambda_i| \exp(i\alpha)\, u_i \quad i = 1,2 \qquad \text{(B-33)}$$

where α_i is the phase of the eigenvalue. Applying equation 33 to equations 29-32, we find the eigenvalue phases to be:

$$\alpha_1 = -66.5^\circ \qquad \alpha_2 = -57.4^\circ \tag{B-34}$$

and the impedance can be written as:

$$Z = \begin{bmatrix} -.05907\,e^{i6.4^\circ} & .9983 \\ -.9983 & -.05907\,e^{-i6.4} \end{bmatrix} \begin{bmatrix} 7.964\,e^{-i66.5} & \\ & 5.488\,e^{-i57.4} \end{bmatrix} \begin{bmatrix} .9863\,e^{-i.18^\circ} & -.1648\,e^{+i6.47^\circ} \\ .1648\,e^{-i6.47^\circ} & .9863\,e^{+i.18^\circ} \end{bmatrix}$$

(B-35)

The eigenvalue magnitudes represent the maximum and minimum electric fields that can be produced with unit magnetic fields. The eigenvalue phases represent the phase shift between the E and H eigenvector fields caused by the presence of the conducting earth. In this example, the u and v eigenvectors are nearly linearly polarized with principal directions within 10 degrees of the X and Y axes.

The angle each of the polarization ellipses makes with respect to the X axis can be found with the equation (Stratton,1941) for the electric eigenvectors:

$$\tan 2\theta_i = \frac{2|u_{ix}|\,|u_{iy}|}{|u_{ix}|^2 - |u_{iy}|^2} \cos(\delta_i) \tag{B-36}$$

and for the magnetic eigenvectors:

$$\tan 2\phi_i = \frac{2\,|V_{ix}|\,|V_{iy}|}{|V_{ix}|^2 - |V_{iy}|^2} \cos(\xi_i) \qquad \text{(B-37)}$$

where (δ_i) are the phase differences between the X and Y components of the electric eigenvectors (u_i) and (ξ_i) are the phase differences between the X and Y components of the magnetic field eigenvectors. The quadrants for (θ_i) and (ϕ_i) are determined from considerations of the signs of the eigenvector components. For this example:

$$\begin{array}{ll} \theta_1 = -93.4^\circ & \theta_2 = -3.4^\circ \\ \phi_1 = -9.4^\circ & \phi_2 = 80.6^\circ \end{array} \qquad \text{(B-38)}$$

As mentioned in Chapter 2, the three dimensional parameter. skew, is the deviation from perpendicularity of the u and v eigenvectors. We define our coordinate invariant skew as:

$$S = 90 - |\theta - \phi| \qquad \text{(B-39)}$$

where (θ) is either of the u eigenvector principal axis directions and (ϕ) is the corresponding v principal axis direction. Negative skew corresponds to an angle greater than 90 degrees and positive skew for angles less than 90 degrees. For our example:

$$S = +6 \text{ degrees} \qquad \text{(B-40)}$$

With this sign convention, the tangent of our skew angle (S) is equal to the conventional skew (Sc). We can derive this relationship by noting first that:

$$\mathrm{Re}\left\{ u_i \cdot v_i^* \right\} = \cos \xi \qquad (B-41)$$

$$i = 1,2$$

and:

$$\mathrm{Re}\left\{ (u_i \times v_i^*) \cdot \hat{i}_z \right\} = \sin \xi \qquad (B-42)$$

where (ξ) is the angle between the unit eigenvectors (u_i) and (v_i). From equations (2-2) and (2-7). we find that:

$$Z_{xx} + Z_{yy} = \lambda_1 u_1 \cdot v_1^* + \lambda_2 u_2 \cdot v_2^* \qquad (B-43)$$

and:

$$Z_{xy} - Z_{yx} = \lambda_1 (u_1 \times v_1^*) \cdot \hat{i}_z + \lambda_2 (u_2 \times v_2^*) \cdot \hat{i}_z \qquad (B-44)$$

Combining (43) and (44), the conventional skew (Sc) can be represented in terms of the eigenvector products such that:

$$S_c = \frac{Z_{xx} + Z_{yy}}{Z_{xy} - Z_{yx}} = \frac{\lambda_1 u_1 \cdot v_1^* + \lambda_2 u_2 \cdot v_2^*}{\lambda_1 (u_1 \times v_1^*) \cdot \hat{i}_z + \lambda_2 (u_2 \times v_2^*) \cdot \hat{i}_z} \qquad (B-45)$$

From (41) and (42), the real part of the conventional skew is related to the angle between (u_i) and (v_i) such that:

$$\mathrm{Re}\,\{Sc\} = \cot(\xi) \qquad (B-46)$$

Because the angle (ξ) represents the 90 degree phase shift between (u) and (v) associated usually with 2D structures minus the skew (S). we can write (ξ) in the form:

$$\zeta = 90 - S \qquad \text{(B-47)}$$

and:

$$Re\left\{ \frac{Z_{xx} + Z_{yy}}{Z_{xy} - Z_{yx}} \right\} = Re\left\{ S_c \right\} \simeq \tan(S)$$

Thus, our skew and the conventional skew have the relationship:

$$S = \text{arc } \tan[Re\{Sc\}] \qquad \text{(B-49)}$$

For our example:

$$Sc = .105\exp(i1.2\ ) \qquad \text{(B-50)}$$

and:

$$\tan[Re\{Sc\}] = 6 \text{ degrees} = S \qquad \text{(B-51)}$$

Thus, the conventional skew is related directly to our skew definition and is a measure of the deviation from normal of the electric and magnetic principal axis directions.

The other 3D parameter of interest in magnetotelluric studies is the aspect ratio of the eigenvector polarization ellipses. Because of the orthogonality condition, the aspect ratio is the same for both the electric polarization ellipses. Similarly, the magnetic eigenvector ellipses are described by a single aspect ratio. The aspect ratio for an ellipse is the ratio of its minor axis to its major axis. Eggers (1981) suggests assigning a sign to the aspect ratio to indicate the rotation direction of the eigenvector or handedness of the polarization state. Using Eggers (1981) ellipticity formulation, the signed aspect ratio is:

$$e = \frac{1-r}{1+r} \qquad (B\text{-}52)$$

where:

$$r_{u_i} = \frac{|u_{ix}^2 + u_{iy}^2|}{|u_{ix}|^2 + |u_{iy}|^2 - 2\,\mathrm{Im}\{u_{ix} u_{iy}^*\}} \qquad (B\text{-}53)$$

for the u eigenvectors and:

$$r_{v_i} = \frac{|v_{ix}^2 + v_{iy}^2|}{|v_{ix}|^2 + |v_{iy}|^2 - 2\,\mathrm{Im}\,(v_{ix} v_{iy}^*)} \qquad (B\text{-}54)$$

for the v eigenvectors. This formulation is an outgrowth of the ellipticity representation of Jackson (1975). A positive sign corresponds to counterclockwise rotation and the negative sign corresponds to clockwise rotation as viewed against the direction of propagation (Eggers,1981). For our example, the aspect ratios are:

$$e_{u_1} = -.00658 \qquad e_{u_2} = +.00658 \qquad (B\text{-}55)$$
$$e_{v_1} = -.0379 \qquad e_{v_2} = +.0379$$

To reiterate the steps of our procedure. we first form $Z\tilde{Z}$ and $\tilde{Z}Z$ with which we find the eigenvalue magnitudes and eigenvector component ratios. We then normalize the component magnitudes and assign, arbitrarily, the phase and sense of one (v) eigenvector with which the second (v) eigenvector is calculated to be Hermitianally orthogonal. The signs of the (u) eigenvector components are then determined such that the corresponding (u) and (v) eigenvectors obey Poynting vector requirements. The phases are assigned so that the corresponding (u) and (v) eigenvectors rotate in the same direction around their polarization ellipses. The individual polarization ellipses are phase shifted so that each eigenvector is at its maximum at $(t = 0)$. After these assignments, the phases of the eigenvalues are calculated. The skew is then calculated from the spatial directions of the corresponding (u) and (v) eigenstates. The ellipticities of the (u) and (v) eigenstates are calculated from the eigenvector magnitudes at $(\omega t=0)$ and $(\omega t = \pi/2)$.

As Figure B.1, we present graphically the individual eigenvector polarization ellipses which represent the electric fields $(\lambda_1 u_1)$ and $(\lambda_2 u_2)$ for the unit magnetic fields (v_1) and (v_2). The arrows point to the positions on the polarization ellipses of each of the eigenstates at $(t = 0)$.

To summarize this appendix, we have presented the eigenvector orthogonality conditions, the algebraic form of the impedance eigenstates, and a numerical example of our procedures and conventions for calculating the eigenstates of the impedance tensor.

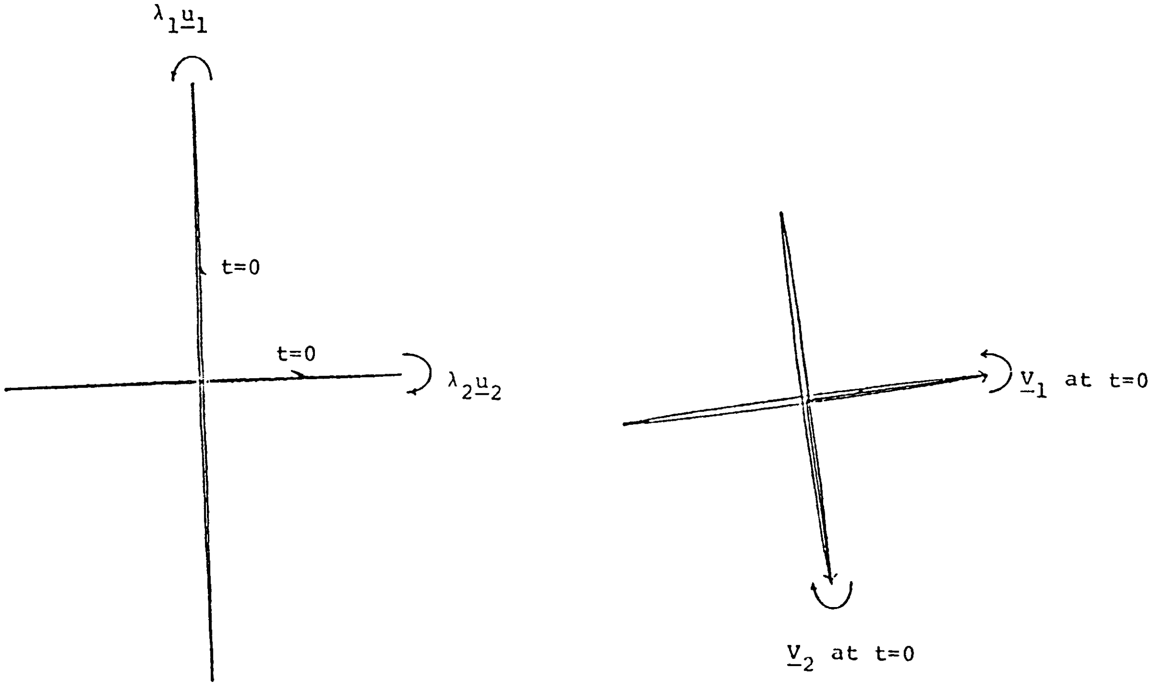

FIGURE B.1 MAGNETOTELLURIC EIGENSTATES

Appendix C

Impedance Calculations: An Approximate Form

C.0 In phase behaviour

To infer lateral variations in geologic structure and regional current density patterns. we measured the magnetotelluric field at sites along and near the San Andreas Fault system between Frazier Park and Wrightwood, California. The data was bandlimited to periods between 50 and 150 seconds. For these long periods, the relationship between E and H is controlled by the mantle conductivity which increases with increasing depth. Accordingly. the horizontal E fields tend to be within 20-30 degrees of being in phase with the time derivatives of their magnetic field counterparts. This in phase behaviour can be illustrated best by an example due to Ted Madden (personal communication).

Consider a toroidal E field source ($E_z = 0$) responding to an earth for which conductivity increases with increasing depth. Then, the curl of E in the X direction is:

$$\frac{\partial E_x}{\partial z} = -\mu \frac{\partial H_y}{\partial t} = -\mu \dot{H}_y \qquad \text{(C-1)}$$

With the conductivity increasing with depth Ex will diminish to zero at some depth z and :

$$\left(E_{x@z} - E_{x@z_0}\right)/(z-z_0) \hat{=} -\mu \dot{H}_y \qquad \text{(C-2)}$$

or

$$E_{x\,(\mathrm{surface})} \propto \dot{H}_y \qquad \text{(C-3)}$$

Conversely. if the conductivity decreases with depth. at some point the magnetic field will diminish to zero and. from the curl of H. the surface H will be proportional to and in phase with the surface E. Straddling these two extremes is the case of a homogeneous earth for which the phase between E and H is 45 degrees.

At low frequencies. the magnetotelluric field samples the upper mantle and the deviation from zero phase between E and $\dot{H}$ is due largely to the mantle's finite conductivity. For this finite but increasing with depth conductivity. the elements of the modified impedance relating E and $\dot{H}$ have a common phase. Ignoring this common phase and using real analysis has little effect on the calculation of the principal axes of the impedance tensor and reduces only slightly the estimates of the eigenvalues. As we show later in this appendix, larger biases of the calculation of the impedance tensor itself can occur due to noise in the measurements and we feel that the use of the approximate real analysis is justified especially at the low frequencies of our measurements.

C.1 Impedance calculations

As indicated in Appendix A. we used magnetic coils to measure the magnetic fields. The output of these coils is proportional to $\dot{H}$. Thus. our field measurements consisted of two horizontal E field channels and two horizontal $\dot{H}$ measurements. In view of the approximately in phase relationships between our E and $\dot{H}$ measurements we chose to simplify our analysis to estimating the modified impedance tensor $\dot{Z}$ for which:

$$E = \dot{Z}\,\dot{H} \tag{C-4}$$

where $\dot{Z}$ has the units mv/km/γ/sec. We note that for our limited frequency band estimates of $\dot{Z}$ will tend to be independent of frequency which allows us to form consistent data comparisons between our MT stations. Let us consider now the techniques used to infer estimates of $\dot{Z}$.

Two impedance estimation procedures can be used to find $\dot{Z}$. For one procedure the E fields are assumed free of noise and for the other the H fields are assumed free of noise. With both procedures the impedance tensor is determined in the least squares sense. Because both E and $\dot{H}$ channels have noise. we use both approaches to estimate $\dot{Z}$. Then, based on the calculated coherencies and spread of tensor element values between the two sets of estimates, we infer an intermediate impedance tensor as a coherency weighted geometric mean of the two calculated tensors and estimate a signal to noise ratio. Finally, we recompute both tensor estimates using a stochastic inverse. The stochastic inverse provides damping of the two tensor estimates toward the intermediate model. The level of damping is based on the assumed signal to noise ratio and model undertainty.

The major constraint on this scheme is the requirement that the damping does not degrade markedly the coherency between the E and $\dot{H}$ fields. Poor choices of an intermediate $\dot{Z}$ or signal to noise ratio can result in degradation of the E,$\dot{H}$ coherency. Let us consider now the details of these estimation procedures followed by examples of impedance tensors calculated from data taken near the San Andreas fault system in southern California.

After inspection of the data for spectral content usually two frequency bands are chosen and the data is filtered with a four pole Bessel digital filter.

For these filtered records. we assume the E and $\dot{H}$ data sets are related by real constants such that:

$$\begin{bmatrix} E_{11} & E_{21} \\ \vdots & \vdots \\ E_{1N} & E_{2N} \end{bmatrix} = \begin{bmatrix} \dot{H}_{11} & \dot{H}_{21} \\ \vdots & \vdots \\ \dot{H}_{1N} & \dot{H}_{2N} \end{bmatrix} \begin{bmatrix} a & c \\ b & d \end{bmatrix} \tag{C-5}$$

where Ei and $\dot{H}i$ are the filtered time series. Alternatively we can write 5 in the more compact form:

$$E^{T} = \dot{H}^{T} \dot{Z}^{T} \tag{C-6}$$

For the assumption of no noise in the magnetic fields we pre-multiply both sides of (6) by the filter time series $\dot{H}$ and solve for $\dot{Z}$ such that:

$$\dot{H}\ E = \dot{H}\ \dot{H}^{T} \dot{Z}^{T} \tag{C-7}$$

and:

$$\dot{Z} = E\ \dot{H}^{T} [\dot{H}\ \dot{H}^{T}]^{-1} \tag{C-8}$$

$$= \begin{bmatrix} E_1 \cdot \dot{H}_1 & E_1 \cdot \dot{H}_2 \\ E_2 \cdot \dot{H}_1 & E_2 \cdot \dot{H}_2 \end{bmatrix} \begin{bmatrix} \dot{H}_1 \cdot \dot{H}_1 & \dot{H}_1 \cdot \dot{H}_2 \\ \dot{H}_2 \cdot \dot{H}_1 & \dot{H}_2 \cdot \dot{H}_2 \end{bmatrix}^{-1}$$

where $A \cdot B$ is the vector dot product. Note that noise in $\dot{H}1$ or $\dot{H}2$ is additive in their auto products with the result that the estimates of $\dot{Z}$ are biased downward. For the assumption of no noise in the E fields we premultiply both sides of (6) by E and solve for Z such that:

$$E\,E^{T} = E\,\dot{H}^{T}\dot{Z}^{T} \qquad \text{(C-9)}$$

and:

$$\dot{Z} = E\,E^{T}[\dot{H}\,E^{T}]^{-1} \qquad \text{(C-10)}$$

$$= \begin{bmatrix} E_1\cdot E_1 & E_1\cdot E_2 \\ E_2\cdot E_1 & E_2\cdot E_2 \end{bmatrix} \begin{bmatrix} \dot{H}_1\cdot E_1 & \dot{H}_1\cdot E_2 \\ \dot{H}_2\cdot E_1 & \dot{H}_2\cdot E_2 \end{bmatrix}^{-1}$$

Here noise in E is additive in the auto products with the result that the estimates of $\dot{Z}$ are biased upward. Note also that if the E fields are close to being linearly polarized, the inverse $[\dot{H}E^{T}]$ in (10) can become singular which also tends to bias the estimate of $\dot{Z}$ upward.

Thus we see that in the presence of noise the actual $\dot{Z}$ tensor lies somewhere between the estimates of equations (8) and (10). Because of the strong tendency of low frequency E fields to be coherent and high E field coherencies to upward bias the impedance estimates. we feel that in most cases the actual $\dot{Z}$ is closer to the estimates of equation (8) (no $\dot{H}$ noise) than those of (10) (no E noise). Accordingly. we choose an intermediate model for the stochastic inverse as a coherency weighted geometric mean of the two impedance estimates. Let us consider now. the details associated with applying stochastic constraints on the two impedance estimating procedures.

In the application of the stochastic inverse to $\dot{Z}$ in equation (8). which is biased by noise in $\dot{H}$. we seek simultaneously to minimize the following quantities with respect to changes in $\dot{Z}$.

$$\frac{1}{\sigma_\ell^2}\left\{E-\dot{Z}\dot{H}\right\}^2+\frac{1}{\sigma_m^2}\left(\dot{Z}-\dot{Z}_0\right)^2 \tag{C-11}$$

where σ_ℓ^2 and σ_m^2 are respectively noise in the data and uncertainties in the model for $\dot{Z}$,and $\dot{Z}_0$ is a coherency weighted average of estimates of $\dot{Z}$ from equations (8) and (10).

The resulting stochastic estimation of $\dot{Z}$ is of the form:

$$\dot{Z}^T=\left[\dot{H}\dot{H}^T+\frac{\sigma_\ell^2}{\sigma_m^2}I\right]^{-1}\left[\dot{H}E^T+\frac{\sigma_\ell^2}{\sigma_m^2}\dot{Z}_0^T\right] \tag{C-12}$$

and similarly for equation (10) we seek to minimize:

$$\frac{1}{\sigma_\ell^2}\left(\dot{H}-E\dot{Y}\right)^2+\frac{1}{\sigma_m^2}\left(\dot{Y}-\dot{Y}_0\right)^2 \tag{C-13}$$

which results in the stochastic inverse

$$\dot{Y}^T = \left[E E^T + \frac{\sigma_e^2}{\sigma_m^2} I \right]^{-1} \left[E H^T + \frac{\sigma_e^2}{\sigma_m^2} \dot{Y}_0^T \right] \qquad (C\text{-}14)$$

where $\dot{Z} = [\dot{Y}^T]^{-1}$, σ_e^2 and σ_m^2 are respectively estimates of the noise in the E field and the uncertainty in the model of $\dot{Y}$ and $\dot{Y}_0$ is the inverse of $\dot{Z}_0$ the intermediate model estimate.

Usually a signal to noise ratio of three was assumed and an intermediate $\dot{Z}_0$ was determined using a coherency weighted geometric mean of the estimates of $\dot{Z}$ from the least squares solutions of equations (8) and (10). If a particular choise of $\dot{Z}$ and signal to noise ratio resulted in significant change in the E, $\dot{H}$ coherencies, a new intermediate model was chosen. Thus with equations 8-14 we have a procedure for estimating a modified form of the impedance relating E and $\dot{H}$. Although the above analysis is based on the assumption of a real impedance tensor. a similar approach can be used for a complex impedance tensor by modifying our digital filtering of the data to include a quadrature output time series as well as an in phase time series (Swift. 1967). Then the addition of dot products of the in phase and quadrature time series is equivalent to complex arithmetic in the frequency domain. For example. following Swift (1967). let the subscript (i) represent in phase and

(q) represent quadrature. Then the equivalence between the frequency domain and time domain auto power is of the form:

$$E_x \overline{E}_x = E_{x_i}^2 + E_{x_q}^2 = (E_x \cdot E_x)_i + (E_x \cdot E_x)_q \tag{C-15}$$

and the cross powers have the equivalent forms:

$$\begin{aligned} \mathrm{Re}\left\{ E_x \overline{H}_y \right\} &= E_{x_i} \cdot H_{y_i} + E_{x_q} \cdot H_{y_q} \\ \mathrm{Im}\left\{ E_x \overline{H}_y \right\} &= E_{x_q} \cdot H_{y_i} - E_{x_i} \cdot H_{y_q} \end{aligned} \tag{C-16}$$

where $\overline{(\;)}$ represents complex conjugate and A•B represents vector dot products. We note that this time series approach requires more computer time than does the fast Fourier Transform approach. However. we use the time domain approach because we have found the task of noise discrimination simpler in the time domain. especially for signals which exhibit no relative frequency dependence.

To conclude this appendix let us consider two examples of the inference of the impedance tensor from time series and the determination of the principal axes of the impedance tensor using the eigenstate analysis described in Appendix B.

Our data are bandlimited (50 to 150 seconds) MT measurements from the region of the San Andreas fault system near Palmdale. CA. This data was taken before we had developed a digital recording system requiring the use of Analog Rustrak recorders. The ignominious task of digitization was accomplished with an HP plotter/digitizer coupled to an HP9825 desk computer. Although time correspondence between hand digitized data can produce errors in the analysis. coherencies of up to .996 between E field measurements were found and typically $E,\dot{H}$ coherencies were .5 to .8. Another potential source of error is that considerable energy exists in the 30-50 second band near the low pass poles of our analog circuit filters. Fortunately, however. our filters were well enough matched to allow us to use this data.

Our first example is from a rattlesnake infested butte north of Lake Hughes in the Mojave Desert. The electric fields are nearly linearly polarized and our estimate of $\dot{Z}$ based on equation (10) (no noise in E) is much larger than that based on equation (8) (no noise in $\dot{H}$). Using an intermediate model near the geometric mean between the two estimates we find a more consistent set of impedance estimates without a major degradation of the $E,\dot{H}$ coherences as shown in Figure C-1. As Figure C-1. we present the analysis for the coherencies and impedance elements calculated to predict the E fields from the $\dot{H}$ fields. The least squares analyses based on equations (8) and (10) are included with the stochastic estimates based on equations (12) and (14). $\dot{Z}_0$ is the intermediate model

LEAST SQUARES

MTstat
LH2001
band = 100 to 150 sec

E1/E2 coh
-.82 0.996

E1 = aH1+bH2

a	b
0.53	0.37

coh=0.634

a	b
1.25	0.97

coh=0.525

E2 = aH2+bH1

a	b
-0.48	-0.60

coh=0.631

a	b
-1.34	-1.23

coh=0.546

MTstat
LH2001
band = 60 to 100 sec

E1/E2 coh
-.82 0.989

E1 = aH1+bH2

a	b
0.44	0.34

coh=0.713

a	b
1.66	0.43

coh=0.371

E2 = aH2+bH1

a	b
-.43	-0.52

coh=0.723

a	b
-.77	-1.15

coh=0.623

STOCHASTIC INVERSE

MTstat
LH2001
sig/noise = 3
band = 100 to 150 sec

E1/E2
-.82 0.996

E1 = aH1+bH2

a	b
0.55	0.37

coh=0.634

a	b
1.12	0.78

con=0.525

E2 = aH2+bH1

a	b
-0.50	-.0.60

coh=0.631

a	b
-1.08	-1.18

coh=0.540

$$\dot{Z}_0 = \begin{matrix} 0.8 & 0.6 \\ -0.8 & -0.6 \end{matrix}$$

MTstat
LH2001
sig/noise = 3
band = 60 to 100 sec

E1/E2 coh
-.82 0.989

E1 = aH1+bH2

a	b
0.51	0.34

coh=0.712

a	b
0.88	0.57

coh=0.329

E2 + aH2+bH1

a	b
-0.45	-0.55

coh=0.723

a	b
-0.79	-0.84

cch-0.600

FIGURE C-1 IMPEDANCE ESTIMATES FOR LH2

for $\dot{Z}$ used in the stochastic estimates. The top sets of estimates of E1 and E2 are determined from equations (8) or (12) and are biased by noise in $\dot{H}$. The bottom sets of estimates of E1 and E2 are determined from equations (10) or (14) and are biased by noise in E and high coherency between the E field components. As noted before. more consistent sets of estimates of the elements of $\dot{Z}$ are found with the stochastic inverse without appreciable degradation of the E, $\dot{H}$ coherencies. Even though large amplitude differences exist between the two stochastic weighted estimates of $\dot{Z}$. the directions of the principal axes of the impedance tensor are quite consistent between estimates as shown in Figure C-2.

In Figure C-2 we have plotted two ellipses for the E fields. the principal axes of which are the directions of maximum and minimum resistivities for the corresponding unit $\dot{H}$ field eigenvectors also plotted in Figure C-2. The outer ellipse corresponds to the assumption of no noise in E (equation 14) and the inner ellipse corresponds to the assumption of no noise in $\dot{H}$ (equation 12). We infer that the high degree of correspondence between the principal axis directions and the large variation in amplitudes are for the same reason. the nearly linear polarization of the electric fields (coherency .996). The electric field direction is well constrained and the impedance estimates are nearly singular. The raw data associated with this example is

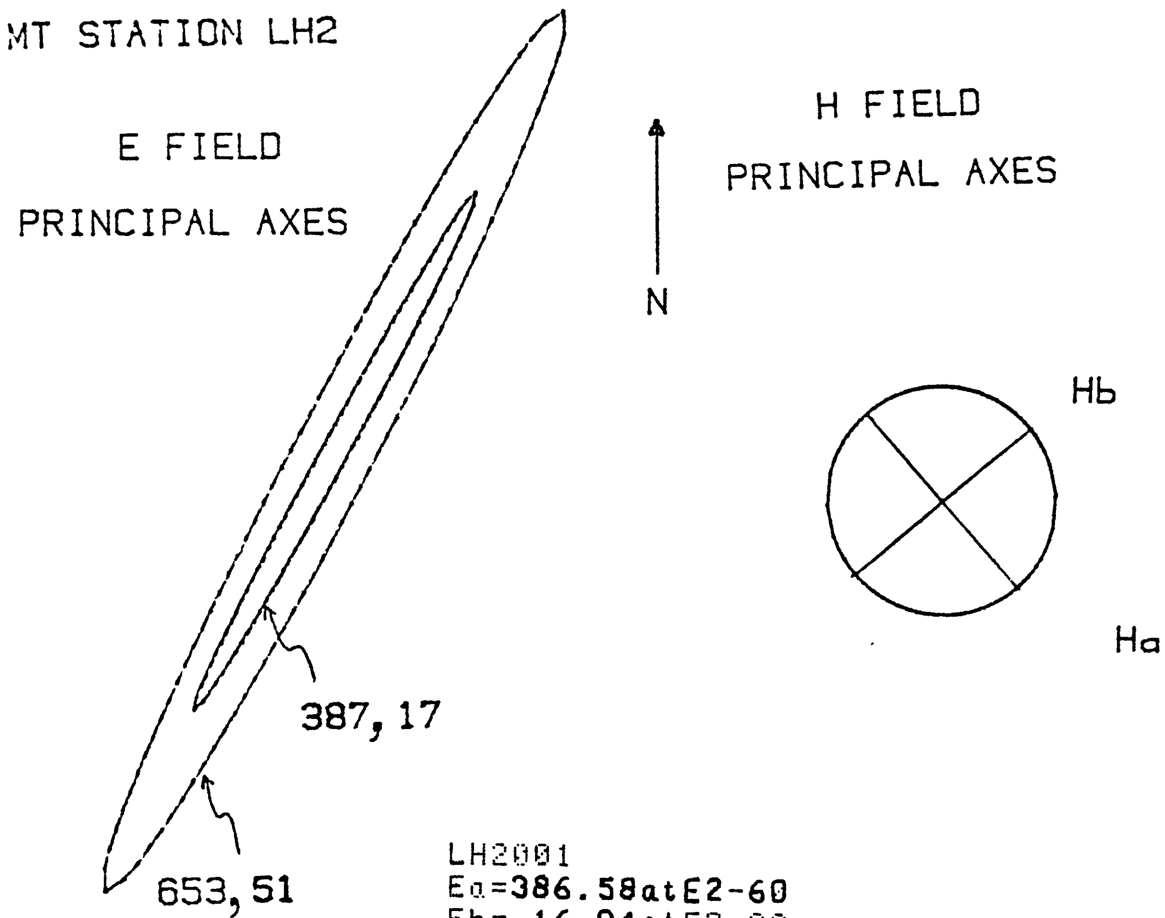

LH2001
Ea=386.58atE2-60
Eb= 16.94atE2 30
Ha at H2 43
Hb at H2-47

LH2001
Ea=653.20atE2-61
Eb= 51.05atE2 29
Ha at H2 43
Hb at H2-47

FIGURE C-2 MT EIGENSTATES FOR LH2

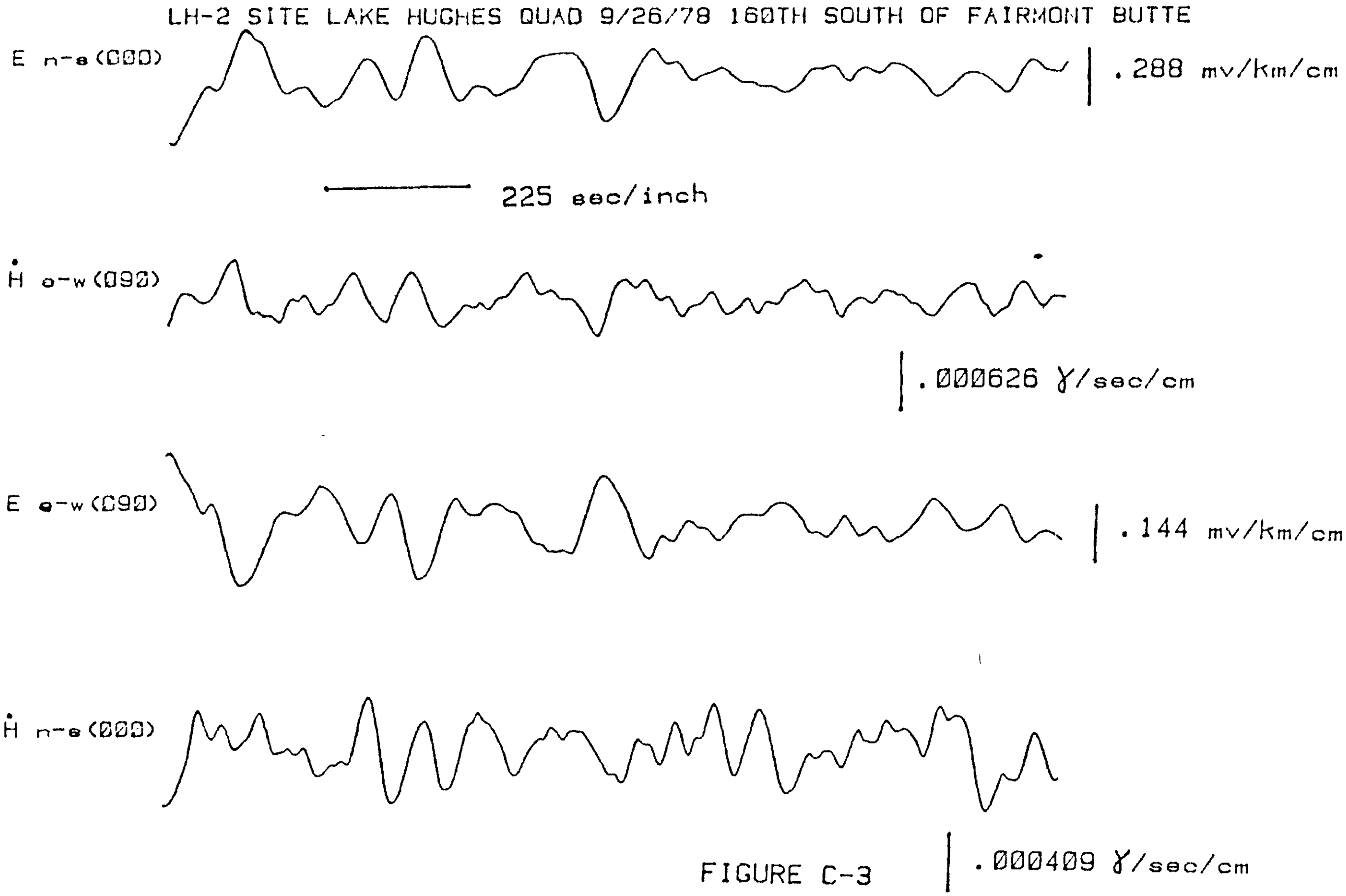
LH-2 SITE LAKE HUGHES QUAD 9/26/78 160TH SOUTH OF FAIRMONT BUTTE
E n-s (000)
.288 mv/km/cm
225 sec/inch
$\dot{H}$ e-w (090)
.000626 γ/sec/cm
E e-w (090)
.144 mv/km/cm
$\dot{H}$ n-s (000)
.000409 γ/sec/cm

FIGURE C-3

presented as Figure C-3.

For our second example. we present data from an MT site near Phelan, CA in the Mojave Desert. Here the impedance is nearly isotropic. As predicted from the eigenstate analysis of Appendix B. the orientation of the principal axes becomes indeterminate. As we did for the first example. we present the least squares and stochastic analyses of $\dot{Z}$ as Figure 4. the eigenstate of $\dot{Z}$ as Figure C-5 and the raw data as Figure C-6. We observe that the spread of values for $\dot{Z}$ is less pronounced than in example one but the principal directions of the impedance eigenstates are poorly resolved.

The procedures outlined in this appendix are used to analyze MT data from southern California between Frazier Park and Wrightwood. The interpretation of these results is used to provide constraints on the thin sheet modelling of southern California described in Chapter 3. Similar procedures can be used to relate telluric fields where E1. the horizontal electric field at site 1. is related to E2. the field at site 2 through the telluric tensor T e.g.

$$E_1 = T\,E_2 \qquad \text{(C-17)}$$

For the assumption of no noise in E2. T is of the form

$$T = \left[E_1 E_2^T\right]\left[E_2 E_2^T\right]^{-1} \qquad \text{(C-18)}$$

LEAST SQUARES ANALYSIS

MTstat
PH1001
band = 80 to 120 sec

E_1/E_2	coh
1.31	0.449

$E_1 = a H_1 + b H_2$

a	b
0.57	0.05

coh = .414

a	b
3.28	0.08

coh = .410

$E_2 = a H_2 + b H_1$

a	b
-0.30	0.10

coh = .576

a	b
-0.75	1.06

coh = .626

band = 30 to 50 sec

E_1/E_2	coh
-1.03	0.078

$E_1 = a H_1 + b H_2$

a	b
0.72	0.18

coh = .656

a	b
2.01	0.18

coh = .573

$E_2 = a H_2 + b H_1$

a	b
-0.39	0.05

coh = .823

a	b
-0.54	0.58

coh = .856

STOCHASTIC INVERSE

sig/noise = 3

E_1/E_2	coh
1.31	0.449

$E_1 = a H_1 + b H_2$

a	b
0.82	0.19

coh = .414

a	b
2.46	0.13

coh = .410

$E_2 = a H_2 + b H_1$

a	b
-0.32	0.12

coh = .576

a	b
-0.61	0.74

coh = .625

$$\dot{Z}_0 = \begin{bmatrix} 1.2 & .18 \\ -.46 & .17 \end{bmatrix}$$

sig/noise = 3

E_1/E_2	coh
-1.01	0.113

$E_1 = a H_1 + b H_2$

a	b
0.93	0.19

coh = .674

a	b
1.62	0.19

coh = .591

$E_2 = a H_2 + b H_1$

a	b
-0.40	0.11

coh = .832

a	b
-0.51	0.40

coh = .864

FIGURE C-4 Impedance Estimates for PH1

MT STATION PH1

E FIELD
PRINCIPAL AXES

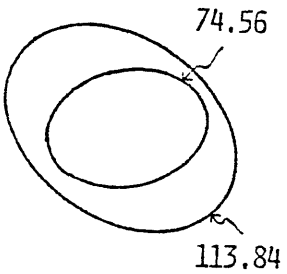

H FIELD
PRINCIPAL AXES

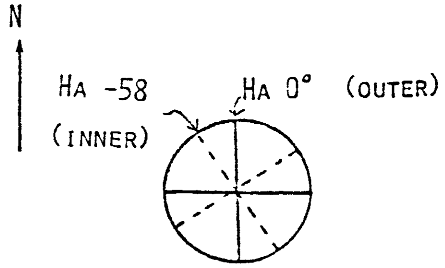

E2 AT 90 WRT NORTH
H2 AT 0 WRT NORTH

PH1001
E_A=73.80 AT E2-14
E_B=55.84 AT E2 76
H_A AT H2 0
H_B AT H2-90

PH1001
E_A=113.18 AT E2 39
E_B= 83.61 AT E2-51
H_A AT H2 58
H_B AT H2 32

FIGURE C - 5 MT EIGENSTATES FOR PH1

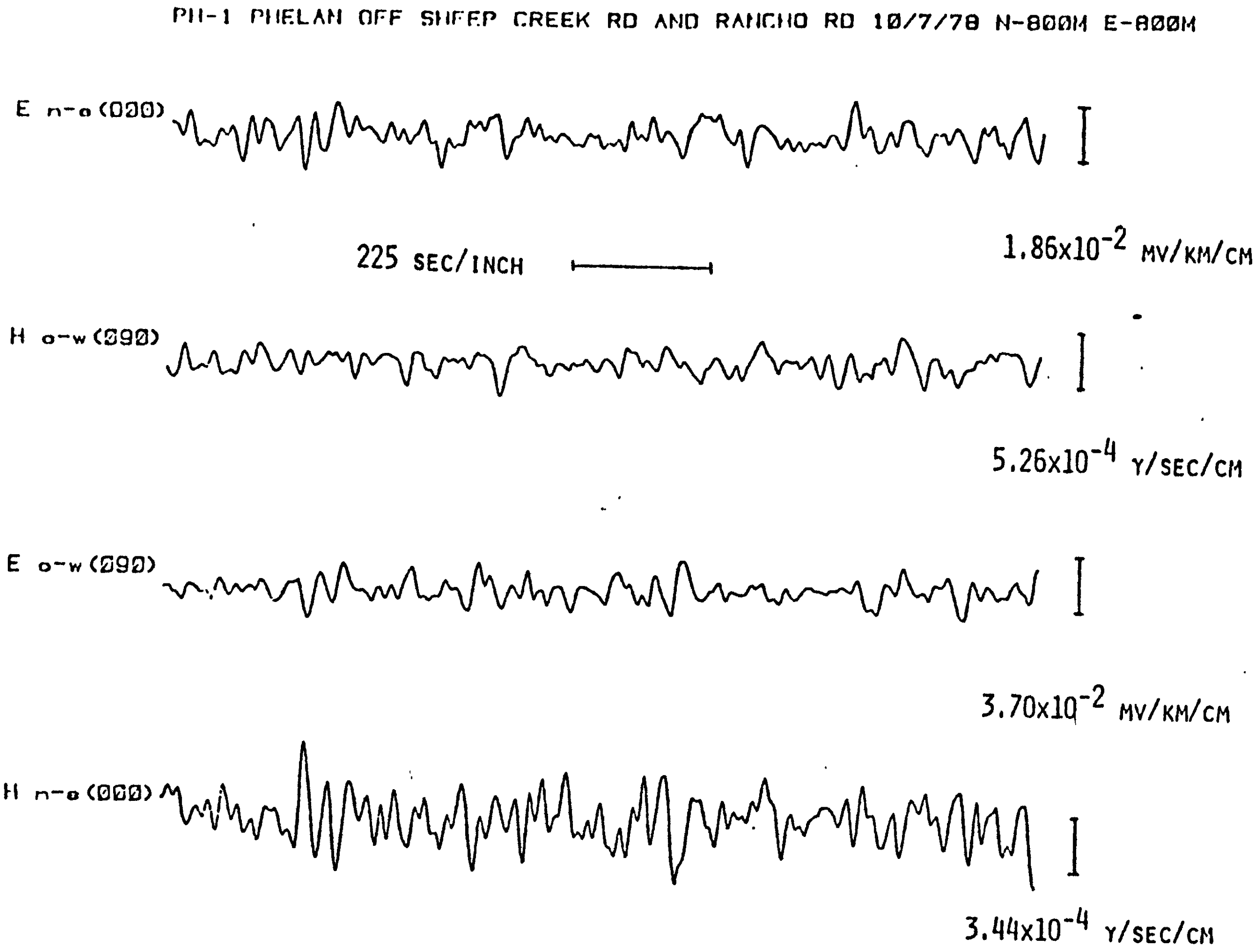
PH-1 PHELAN OFF SHEEP CREEK RD AND RANCHO RD 10/7/78 N-800M E-800M
E n-o (000)
225 SEC/INCH
1.86x10^{-2} MV/KM/CM
H o-w (090)
5.26x10^{-4} Y/SEC/CM
E o-w (090)
3.70x10^{-2} MV/KM/CM
H n-o (000)
3.44x10^{-4} Y/SEC/CM

FIGURE C - 6

and for the assumption of no noise in E1, T is of the form

$$T = \left[E_1 E_1^T \right] \left[E_2 E_1^T \right]^{-1} \qquad \text{(C-19)}$$

Similar to the noise corruption of the impedance estimates. noise in E2 will bias the telluric tensor estimates downward while noise in E1 and/or high correlation between E2 and E1 will bias the estimates of (19) upward.

Appendix D

Poloidal mode response to embedded ellipsoids

D.0 Introduction

The purpose of this appendix is to provide the necessary background material for modelling the telluric field response to an embedded 3D induced polarization target. We present the eigenstates of the electric field tensor relating static fields inside and outside of a conducting ellipsoid of revolution embedded in a conducting earth. We extend these static field solutions to the low frequency telluric field response to a buried ellipsoid. Also. we discuss the effects of current saturation on the sensitivity of the eigenstates to changes in ellipsoid conductivity with frequency.

The telluric field is distorted locally by the presence of three dimensional heterogeneities in the resistivity structure. The current systems associated with these distortions can be classified as poloidal and toroidal. The poloidal currents are the large scale currents induced in the earth by similarly large scale particle motions outside the earth's atmosphere. These currents are largely horizontal. The scale of the induction vortices or current loops is the order of continents (Berdichevskii,1960). Because of the resistive lower crust. even at low frequencies the poloidal currents and outside as:

$$V_2 = V_0 + (\epsilon-1)\left\{ \frac{A_\ell E_{ox} X}{1 + A_0(\epsilon-1)} + \frac{B_\ell E_{oy} Y}{1 + B_0(\epsilon-1)} \right. \tag{D-4}$$

where the conductivity contrast is represented as:

$$\epsilon = \sigma_1 / \sigma_2 \tag{D-5}$$

and the geometric coefficients (A_ℓ and B_ℓ) are determined from:

$$A_\ell = \frac{abc}{2} \int_\ell^\infty \frac{du}{(a^2+u)\,\Delta(u)}$$

$$B_\ell = \frac{abc}{2} \int_\ell^\infty \frac{du}{(b^2+u)\,\Delta(u)} \tag{D-6}$$

$$\Delta(u) = \left\{ (a^2+u)(b^2+u)(c^2+u) \right\}^{1/2}$$

where l is the positive root of:

$$\frac{x^2}{a^2+\ell} + \frac{y^2}{b^2+\ell} + \frac{z^2}{c^2+\ell} \tag{D-7}$$

A_o and B_o represent the geometric coefficients for l=0. The electric field is derived from the gradient of the potential and is represented as:

are confined mostly to the upper crust (Ranganayaki and Madden,1979). Similar to electrostatic currents, the poloidal currents pass through and around local heterogeneities. The distortions of the surface field are thereby coupled resistively with buried heterogeneities.

The toroidal current system consists of local current loops confined largely to conductive heterogeneities. The existence of current loops distorts the surface field inductively.

As long as the skin depth in the overburden is small enough for telluric currents to penetrate to the heterogeneity, the surface field will be affected locally through the poloidal mode. At low frequencies and small measurement separations, the poloidal current system is equivalent approximately to an electrostatic current system Berdichevskii (1960). The frequency dependence of the toroidal current system is associated with the conductivity, dimensions, and shape of the conducting body (Kaufmann,1978a). In general both modes contribute to the surface field. However, at low frequencies the poloidal mode is the dominant contributor.

Here we consider source frequencies low enough and telluric line lengths short enough that the toroidal mode can be ignored and we analyze the approximate poloidal response to heterogeneities in the form of ellipsoids of revolution (circular crossection).

When the low frequency poloidal mode of the telluric field is essentially equivalent to a DC field, the wave solutions of the Helmholtz equation can be approximated by electrostatic solutions of Laplace's equation in the boundary value study of buried or embedded heterogeneities (Lee,1977). A mathematically simple, yet useful model of an embedded heterogeneity is an ellipsoid of revolution (spheroid). The range of shapes that can be considered with ellipsoids of revolution varies from that of a thin disk (oblate spheroid) through a sphere to a long cigar (prolate spheroid). Solutions for the electrostatic response of a conducting ellipsoid embedded in a conducting medium are well known (Stratton,1941, Sommerfeld,1952,Carslaw and Jaeger,1952,and Lee,1977). These electric field solutions provide us with insights into the expected telluric fields and telluric relationships in and near buried heterogeneities in the resistivity structure. Let us first present the mathematical formalism and then consider the effects on the local electrical fields of a perturbation in the ellipsoid conductivity consistent with the frequency dependent conductivity of an IP target.

D.1 Telluric tensors near a conducting spheroid

We formulate the electric fields in and near an embedded conducting ellipsoid using the analysis of Lee(1977). We place an ellipsoid of conductivity (σ_1) in a homogeneous medium of conductivity (σ_2). The axes of the ellipse (a.b and c) are aligned respectively with the X.Y. and Z directions and the fields in and near the ellipsoid are formulated in terms of a distant source field in the X and Y directions. Two cases are considered, first the prolate ellipsoid where a>b=c and then the oblate ellipsoid where a<b=c.

General Solution

The equation at the point (X.Y.Z) on the surface of an ellipsoid whose axes are aligned with a Cartesian coordinate system is:

$$\left(\frac{x}{a}\right)^2+\left(\frac{y}{b}\right)^2+\left(\frac{z}{c}\right)^2=1 \qquad \text{(D-1)}$$

Let the potential far from the ellipsoid be represented as:

$$V_0=-E_{0x}X-E_{0y}Y \qquad \text{(D-2)}$$

Then the potential inside the ellipsoid for z=0 is represented as:

$$V_1=-E_{0x}\frac{X}{1+A_0(\epsilon-1)}-E_{0y}\frac{Y}{1+B_0(\epsilon-1)} \qquad \text{(D-3)}$$

$$E_i = -\nabla V_i \qquad i = 0,1,2 \tag{D-8}$$

Inside the ellipsoid. the electric field is:

$$E_1 = \frac{E_{ox}}{1 + A_o(\epsilon - 1)} \hat{i}_x + \frac{E_{oy}}{1 + B_o(\epsilon - 1)} \hat{i}_y \tag{D-9}$$

while outside the ellipsoid. the electric field is:

$$E_2 = E_{2x} \hat{i}_x + E_{2y} \hat{i}_y \tag{D-10}$$

where:

$$\begin{aligned} E_{2x} = &\left\{ \frac{1 + \left\{ (A_o - A_\ell) - x \frac{\partial A_\ell}{\partial x} \right\} (\epsilon - 1)}{1 + A_o(\epsilon - 1)} \right\} E_{ox} \\ &- \left\{ \frac{y(\epsilon - 1)}{1 + B_o(\epsilon - 1)} \frac{\partial B_\ell}{\partial x} \right\} E_{oy} \end{aligned} \tag{D-11}$$

$$\begin{aligned} E_{2y} = &\left\{ \frac{1 + \left[(B_o - B_\ell) - y \frac{\partial B_\ell}{\partial y} \right] (\epsilon - 1)}{1 + B_o(\epsilon - 1)} \right\} E_{oy} \\ &- \left\{ \frac{x(\epsilon - 1)}{1 + A_o(\epsilon - 1)} \frac{\partial A_\ell}{\partial y} \right\} E_{ox} \end{aligned}$$

As a consequence of (9) the tensor relationship between the field at infinity and the field within the ellipsoid is:

$$E_1 = \begin{bmatrix} E_{x_1} \\ E_{y_1} \end{bmatrix} = \begin{bmatrix} \frac{1}{1+A_0(\epsilon-1)} & \\ & \frac{1}{1+B_0(\epsilon-1)} \end{bmatrix} \begin{bmatrix} E_{0x} \\ E_{0y} \end{bmatrix} = \vec{T}_1 E_0 \qquad \text{(D-12)}$$

and from (12) the tensor relationship between the field at infinity and the field near the ellipsoid is:

$$E_2 = \begin{bmatrix} E_{x_2} \\ E_{y_2} \end{bmatrix} \begin{bmatrix} \frac{1+(\epsilon-1)(A_0 - A_\ell - \frac{\partial A_\ell}{\partial x} x}{1+A_0(\epsilon-1)} & \frac{-(\epsilon-1) y \frac{\partial B_\ell}{\partial x}}{1+B_0(\epsilon-1)} \\ \frac{-(\epsilon-1) x \frac{\partial A_\ell}{\partial y}}{1+A_0(\epsilon-1)} & \frac{1+(\epsilon-1)(B_0 - B_\ell - y \frac{\partial B_\ell}{\partial y})}{1+B_0(\epsilon-1)} \end{bmatrix} \begin{bmatrix} E_{0x} \\ E_{0y} \end{bmatrix} \qquad \text{(D-13)}$$

Combining (13) and (14) we find the tensor relationship between the field inside and out to be:

$$E_2 = T_2 T_1^{-1} E_1 = T\ E_1 \qquad \text{(D-14)}$$

where:

$$T = \begin{bmatrix} 1+(\epsilon-1)\left(A_0-A_\ell-x\frac{\partial A_\ell}{\partial x}\right) & -(\epsilon-1)\,y\frac{\partial B_\ell}{\partial x} \\ -(\epsilon-1)\,x\frac{\partial A_\ell}{\partial y} & 1+(\epsilon-1)\left(B_0-B_\ell-y\frac{\partial B_\ell}{\partial y}\right) \end{bmatrix} \qquad \text{(D-15)}$$

As we shall show in Section D.3:

$$x\frac{\partial A_\ell}{\partial y} = y\frac{\partial B_\ell}{\partial x} \qquad \text{(D-16)}$$

with the result that T is a symmetric tensor. Another characteristic of T. which we shall show in Section D.2. is that the principal axis directions are the same inside and outside the ellipsoid and independent of conductivity contrast. In fact, we find that for tensors relating fields inside to those outside the ellipsoid, the principal axis directions are always perpendicular and parallel to the surface of the ellipsoidal conductor.

Equations (1) through (16) are applicable to the electrostatic responses of both the prolate and oblate spheroids. The calculation of the elements of T for the prolate and oblate spheroids is described in Section D.3.

D.2 Tensor eigenstates

In this section, we use the analysis of Chapter 2 to establish the eigenstates of the Hermitian tensor T which relates the electric fields inside and outside of an embedded ellipsoid. We show that the principal axis directions of the eigenvectors are always perpendicular and parallel to the ellipsoid boundaries.

Because T is Hermitian, its rows and columns have the same eigenvectors. Thus, the eigenvector matrix representing the eigenvectors inside the ellipsoid is parallel to the external eigenvector matrix. The combined eigenstates of T can be expressed as:

$$T = U^{\textcircled{2}} \Lambda \tilde{U}^{\textcircled{1}} \qquad \text{(D-17)}$$

The $U^{\textcircled{1}}$ eigenvector matrix contains the eigenvectors within the ellipsoid and the parallel eigenvector matrix $U^{\textcircled{2}}$ contains the eigenvectors at some point P external to the ellipsoid as depicted in Figure D.1. The matrix product $U^{(2)}\Lambda$ represents the electric fields at point P produced by the unit eigenvector fields $U^{\textcircled{1}}$. Consistent with the impedance formulation, the components of $U^{\textcircled{2}}\Lambda$, $\lambda_1 u_1$ and $\lambda_2 u_2$, represent respectively the maximum and minimum electric fields that can be produced at point P by unit electric fields within the ellipsoid.

The eigenvalues of T can be written as:

$$\lambda_i = 1 + (\epsilon - 1)\left\{ F + (-1)^{i-1} G \right\} \qquad i = 1, 2 \tag{D-18}$$

and the ratios of the eigenvector components which define the principal axis directions can be expressed as:

$$\frac{u_{1y}}{u_{1x}} = \frac{F + (-1)^{i-1} G - D}{E} \qquad i=1.2 \tag{D-19}$$

where:

$$F = \left\{ (A_0 + B_0) - (A_\ell + B_\ell) - \left(x \frac{\partial A_\ell}{\partial x} + y \frac{\partial B_\ell}{\partial y} \right) \right\} / 2$$

$$G = \left\{ \left[\frac{(A_0 - B_0) - (A_\ell - B_\ell) - \left(x \frac{\partial A_\ell}{\partial x} - y \frac{\partial B_\ell}{\partial y} \right)}{2} \right]^2 + \left(x \frac{\partial A_\ell}{\partial y} \right)^2 \right\}^{\frac{1}{2}}$$

$$D = A_0 - A_\ell - x \frac{\partial A_\ell}{\partial x} \tag{D-20}$$

$$E = -x \frac{\partial A_\ell}{\partial y} = -y \frac{\partial B_\ell}{\partial x}$$

We notice from equations 19 and 20 that the principal axis directions are, as stated initially, independent of the conductivity contrast (ϵ) and are functions only of position (X,Y) and ellipsoid geometry. In order to show that the principal axis directions are perpendicular and parallel to the ellipsoid boundary, we shall make use of this insensitivity of the principal axes to the conductivity contrast and the fact at any external point the principal axes are aligned with the maximum and minimum electric field directions.

If we let the conductivity of the ellipsoid tend toward infinity. we see from equations 18-20 that the eigenvalues will tend toward infinity but the principal axis directions will be unaffected. Near the ellipsoid boundary the maximum external electric field must be normal to the boundary and the minimum electric parallel to the boundary to satisfy continuity of normal current density and continuity of parallel electric field. Thus, the maximum electric field. $\lambda_1 u_1^{\textcircled{2}}$ for a unit internal electric field must be normal to the ellipsoid boundary and the minimum electric field $\lambda_2 u_2^{\textcircled{2}}$ must be parallel to the ellipsoid boundary. Because the principal axis directions have been shown to be independent of conductivity contrast (equation 19), the principal axes must in general be aligned normal and parallel to the ellipsoid boundary. The significance of this result is that electric field measurements near the boundaries of ellipsoidal heterogeneities can be used to infer the shape of the heterogeneity. Additionally. as we show in Section D.4. the effects of current saturation in prolate spheroids can be relegated to the eigenstates parallel to the ellipsoid surface and perpendicular to their minor axes.

D.3 Prolate and oblate spheroid calculations

In this section, we present the equations necessary to calculate the telluric tensor elements for embedded prolate and oblate spheroids. For a prolate spheroid with its long axis (a) parallel to the X axis:

$$a > b = c$$

and introducing the ellipticity terms (e) and (e') such that:

$$e = (a^2-c^2)/a^2 \tag{D-21}$$

and

$$e' = (a^2-c^2)/(a^2+1) \tag{D-22}$$

we find that the geometric coefficients can be written in terms of the ellipticities such that:

$$A_l = \frac{1-e^2}{e^3}\left\{\frac{1}{2}\ln\left(\frac{1+e'}{1-e'}\right) - e'\right\}$$

$$B_l = \frac{1-e^2}{2e^3}\left\{\frac{e'}{1+e'^2} - \frac{1}{2}\ln\left(\frac{1+e'}{1-e'}\right)\right\} \tag{D-23}$$

and the spatial derivatives of the geometric coefficients become:

$$\frac{\partial A_\ell}{\partial x} = - \frac{x}{D_\ell} \left(\frac{1-e^2}{e^3} \right) e'^3$$

$$\frac{\partial A_\ell}{\partial y} = - \frac{y}{D_\ell} \left(\frac{1-e^2}{e^3} \right) \left(\frac{e'^3}{1-e'^2} \right)$$

$$\frac{\partial B_\ell}{\partial x} = - \frac{x}{D_\ell} \left(\frac{1-e^2}{e^3} \right) \left(\frac{e'^3}{1-e'^2} \right) \tag{D-24}$$

$$\frac{\partial B_\ell}{\partial y} = - \frac{y}{D_\ell} \left(\frac{1-e^2}{e^3} \right) \left(\frac{e'^3}{(1-e'^2)^2} \right)$$

where:

$$D_\ell = 21 + a^2 + c^2 - (x^2 + y^2 + z^2) \tag{D-25}$$

From inspection of (24). we see that:

$$x \frac{\partial A_\ell}{\partial y} = y \frac{\partial B_\ell}{\partial x} \tag{D-16}$$

and $T_{12} = T_{21}$ in (15) as indicated earlier. Finally, by using equations (22) through (25) in equations (12) through (15) we have the electrostatic tensor relationships between the E fields associated with a conducting prolate ellipsoid imbedded in a conducting earth. We present now a similar analysis for the oblate ellipsoid of revolution.

For an oblate spheroid with its short axis parallel to the X direction:

$$a < b = c \tag{D-26}$$

Defining the ellipticity terms (e) and (e') as:

$$e = (b^2-a^2)/b^2$$

$$e' = (b^2-a^2)/(b^2+1) \tag{D-27}$$

we find that the geometric coefficients can be written in terms of the oblate spheroid ellipticities as:

$$A_\ell = \frac{(1-e^2)^{\frac{1}{2}}}{e^3}\left\{\frac{e'}{(1-e'^2)^{\frac{1}{2}}} - \sin^{-1} e'\right\}$$

$$B_\ell = \frac{(1-e^2)^{\frac{1}{2}}}{2e^3}\left\{\sin^{-1} e' - e'(1-e'^2)^{\frac{1}{2}}\right\} \tag{D-28}$$

and the spatial derivatives of the geometric coefficients become:

$$\frac{\partial A_\ell}{\partial x} = -\frac{x}{D_\ell}\left(\frac{(1-e'^2)^{\frac{1}{2}}}{e^3}\right)\left(\frac{e'^3}{(1-e'^2)^{3/2}}\right)$$

$$\frac{\partial A_\ell}{\partial y} = -\frac{y}{D_\ell}\left(\frac{(1-e^2)^{\frac{1}{2}}}{e^3}\right)\left(\frac{e'^3}{(1-e'^2)^{\frac{1}{2}}}\right)$$

$$\frac{\partial B_\ell}{\partial x} = -\frac{x}{D_\ell}\left(\frac{(1-e^2)^{\frac{1}{2}}}{e^3}\right)\left(\frac{e'^3}{(1-e'^2)^{\frac{1}{2}}}\right) \tag{D-29}$$

$$\frac{\partial B_\ell}{\partial y} = -\frac{y}{D_\ell}\left(\frac{(1-e^2)^{\frac{1}{2}}}{e^3}\right)\left(\frac{e'^3}{(1-e'^2)^{\frac{1}{2}}}\right)$$

where:

$$D_{\ell} = 2l + a^2 + b^2 - (x^2 + y^2 + z^2) \qquad \text{(D-30)}$$

Equations (28) and (29) can be used directly in (14) and (15) to determine the tensor relating the electric fields inside and outside of an embedded oblate ellipsoid. In the limit of zero ellipticity both the oblate and prolate spheroids become spheres and exhibit the same electrostatic responses. Consistent with the prolate solutions, the tensor for the oblate spheroid is symmetric, the u and v spaces are the same and the eigenvectors inside the ellipsoid are parallel to their external counterparts. With these sets of solutions now we can calculate the anisotropic field response of embedded ellipsoids. In the next section, we relate the anisotropic character of these solutions to the sensitivity of the telluric tensor eigenstates to changes in the conductivity of the ellipsoid.

D.4 The current saturation condition

For a constant source field, the electrostatic current system in and near an ellipsoid is determined by its ellipticity and by the contrast in conductivity of the ellipsoid with its surroundings. Current is funnelled in the long direction of prolate ellipsoids in order to satisfy the continuity of parallel electric field whereas perpendicular to the long direction no funneling is necessary to satisfy the continuity of the normal current density J. Similarly, current is funnelled perpendicular to the minor axis of an oblate ellipsoid in order to satisfy the continuity of the tangential electric field but no current enhancement is required for the continuity of J parallel to the minor axis. Thus. the electric field tensor T_j relating fields inside to those outside the ellipsoid, will be generally anisotropic with the anisotropy dependent on position, conductivity contrast and ellipsoid shape. Additionally, when the current in a particular direction does not increase as the conductivity of the ellipsoid is increased that direction is said to be saturated (Ness.1959). Conversely, when the current in a particular direction changes with a variation in conductivity, that direction is said to be unsaturated. To illustrate the saturation condition we have calculated the electric fields over a wide range of ellipticities and conductivity contrasts. As Tables D.1 and D.2. we present the calculated electric fields inside of prolate and oblate spheroids for a source field of magnitude one in both the X and Y directions.

For the prolate spheroid (Table D.1) the X direction is parallel to the major (long) axis and for the oblate spheroid (Table D.2), the X direction is parallel to the minor axis. From Table D.1. we notice that as the ratio of major to minor axis is increased, a higher conductivity contrast is needed to drive the parallel field Ex into saturation. On the other hand the

TABLE D.1 PROLATE SPHEROID

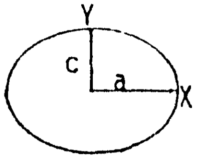

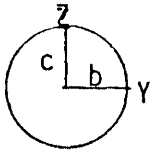

(a/c) →

$\left(\frac{\sigma_1}{\sigma_2}\right)$ ↓	3		10		30		100	
	E_X	E_Y	E_X	E_Y	E_X	E_Y	E_X	E_Y
1.3	.8214	.5287	.9610	.5051	.9932	.5009	.9991	.5001
10	.5055	.1996	.8456	.1848	.9699	.1823	.9961	.1819
30	.2408	.0718	.6296	.0650	.9092	.0647	.9877	.0645
100	.0850	.0222	.3324	.0202	.7457	.0199	.9592	.0198

TABLE D.2 OBLATE SPHEROID

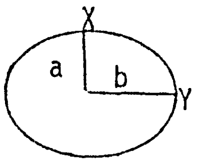

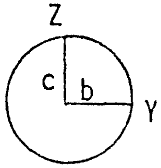

(a/b) →

$\left(\frac{\sigma_1}{\sigma_2}\right)$ ↓	3		10		30		100	
	E_X	E_Y	E_X	E_Y	E_X	E_Y	E_X	E_Y
3	.4404	.7328	.3674	.8778	.3449	.9522	.3368	.9847
10	.1488	.3787	.1143	.6149	.1047	.8157	.1014	.9348
30	.0515	.1591	.0385	.3313	.0350	.5786	.0338	.8164
100	.0156	.0525	.0116	.1267	.0105	.2869	.0102	.5657

perpendicular field Ey is easily saturated and is a very weak function of the ratio of major to minor axes. Similarly from Table D.2. we notice that the field parallel to the minor axis is easily saturated whereas saturation of the field parallel to either of the major axes is dependent on the conductivity contrast and ratio of major to minor axes of the ellipsoid. Thus. a saturation condition contrast within an ellipsoid will result in an anisotropy in the sensitivity of the elements of T to changes in the ellipsoid conductivity.

The anisotropic response of the electrostatic field to a variation in the conductivity of an embedded ellipsoid has an important implication for the search for IP targets with the poloidal mode of the telluric field. As described in Chapter 4. the conductivity of an IP target is a function of frequency varying roughly 1-100% per decade of frequency in the range of 0.01 to 10 Hertz (Cantwell and Madden.1967). Because of the approximate equivalence between the electrostatic and poloidal mode responses to an embedded heterogeneity. we can relate the frequency dependence of the telluric tensor elements to the sensitivity of the electrostatic tensor to changes in conductivity. Additionally, a saturation condition contrast within the ellipsoid results in an anisotropic frequency dependence of the telluric tensor eigenstates.

In Section D.2. we showed that the eigenstates consist of a pair of colinear eigenvectors normal to the ellipsoid surface and related through a single eigenvalue and a pair of eigenvectors parallel to the ellipsoid boundary and related by a single eigenvalue. Because the eigenvectors are insensitive to conductivity contrasts. their corresponding principal axis directions are insensitive to conductivity variations with frequency. The eigenvalue for the colinear eigenstate is always sensitive to changes in the ellipsoid conductivity but the parallel eigenstate can be insensitive to conductivity variations when its eigenvectors are aligned with an unsaturated current direction.

The essential points of this section can be summarized as follows. The relative frequency responses of telluric fields near an ellipsoidal IP target depend on the shape of the ellipsoid and the orientation and position of the telluric measurements. The eigenstates of the telluric tensor relating fields inside and outside the ellipsoid are directed parallel and perpendicular to the surface of the ellipsoid. The perpendicular eigenstates are always sensitive to the frequency dependence of the ellipsoid whereas the frequency dependence of the parallel eigenstates is a function of the saturation condition. In Chapter 4. we apply these concepts to the field study of a pyrite bearing schist which has been shown to exhibit an IP response.

Appendix E

E.0 Introduction

In this appendix, we present methods for determining the apparent conductance of heterogeneous blocks (E.1) used in the thin sheet models of Chapter 3. Additionally, we describe in E.2 our procedures for relating changes in block conductances to uniaxial stress perturbations.

E.1 Block Conductance Calculations

Consider the block geometries drawn as Figure E.1.

Figure E.1 Block Geometries

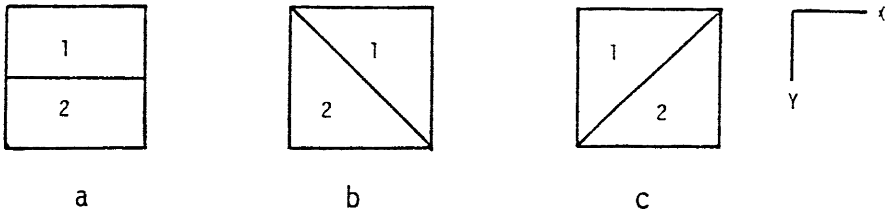

Examples (a). (b), and (c) are blocks spanning a mountain and a valley where the valley alluvium, sub block 2, is more conductive than the mountain, sub block 1. In general the relationship between the horizontal electric field E and the current density J is:

$$\begin{bmatrix} J_X \\ J_Y \end{bmatrix} = \begin{bmatrix} \sigma_{XX} & \sigma_{XY} \\ \sigma_{YX} & \sigma_{YY} \end{bmatrix} \begin{bmatrix} E_X \\ E_Y \end{bmatrix} \qquad (E-1)$$

The conductance tensor is Hermitian for each block model used. Using the the eigenstate analysis of Chapter 2,we can find principal axes for which the the current density J is related to the electric field E by a diagonal tensor.

For model (a) the sub block contact is parallel to the X axis and the principal axes of the conductivity tensor are aligned with our coordinate axes X and Y. In the Y direction. sub block conductances 1 and 2 combine in series such that (σ_{yy}) the average conductance in the Y direction associated with a Y directed E field is:

$$\sigma_{yy} = \sigma_{\perp} = \frac{2\,\sigma_1\,\sigma_2}{\sigma_1 + \sigma_2} \qquad (E-2)$$

and in the X direction. the sub block conductances combine in parallel such that:

$$\sigma_{xx} = \frac{\sigma_1 + \sigma_2}{2} \qquad (E-3)$$

As indicated previously, for the geometry of model (a) no coupling occurs between the X and Y currents and:

$$\sigma_{xy} = \sigma_{yx} = 0 \qquad (E-4)$$

For model (b), the sub block contact is at 45 degrees with respect to the X and Y axes. Consequently, the principal axes of the conductance tensor which are parallel and perpendicular to the contact are rotated from the X and Y axes. To determine the elements of the resultant full conductance tensor, we find the conductances perpendicular and parallel to the sub block contact as we did for model (a) .Then we find the perpendicular and parallel E and J fields in terms of their X and Y components. Finally, we combine the component expressions for J and E to determine the full conductance tensor in our X and Y coordinate system.

Perpendicular to the sub block contact the conductance is:

$$\sigma_{\perp} = \frac{2\,\sigma_1\,\sigma_2}{\sigma_1 + \sigma_2} \qquad (E-5)$$

and parallel to the sub block contact:

$$\sigma_{/\!/} = \frac{\sigma_1 + \sigma_2}{2} \qquad (E-6)$$

The perpendicular and parallel E and J fields are expressed in terms of their X and Y components as:

$$J_{\perp} = \frac{\sqrt{2}}{2}(J_x + J_y) \qquad J_{/\!/} = \frac{\sqrt{2}}{2}(J_y - J_x)$$

$$E_{\perp} = \frac{\sqrt{2}}{2}(E_x + E_y) \qquad E_{/\!/} = \frac{\sqrt{2}}{2}(E_y - E_x) \qquad (E-7)$$

where:

$$J_{\perp} = \sigma_{\perp} E_{\perp} \qquad J_{/\!/} = \sigma_{/\!/} E_{/\!/} \qquad (E-8)$$

and in the X and Y directions the tensor relating E and J is:

$$\underline{\underline{\sigma}} = \begin{bmatrix} \dfrac{\sigma_{\parallel} + \sigma_{\perp}}{2} & \dfrac{\sigma_{\parallel} - \sigma_{\perp}}{2} \\ \\ \dfrac{\sigma_{\parallel} - \sigma_{\perp}}{2} & \dfrac{\sigma_{\parallel} + \sigma_{\perp}}{2} \end{bmatrix} \qquad (E-9)$$

Following the same procedure for model (c), we find a similar tensor, but the off diagonal elements have a change in sign.

$$\underline{\underline{\sigma}} = \begin{bmatrix} \dfrac{\sigma_{\parallel} + \sigma_{\perp}}{2} & \dfrac{\sigma_{\perp} - \sigma_{\parallel}}{2} \\ \\ \dfrac{\sigma_{\perp} - \sigma_{\parallel}}{2} & \dfrac{\sigma_{\parallel} + \sigma_{\perp}}{2} \end{bmatrix} \qquad (E-10)$$

Thus, with combinations of and variations in the blocks shown in Figure E.1, we can account for heterogeneity within the smallest scale of our numerical model of the electrical conductivity thickness product of the upper crust.

E.2 Block Conductance versus Stress

We relate changes in stress to changes in conductivity in the following manner. Consider the horizontal compressive change in stress indicated in Figure E.2. The maximum stress is in the Y direction and the minimum stress in the X direction. Along Y cracks will tend to open and along X cracks will tend to close as depicted in Figure E.3. Accordingly, in regions where the

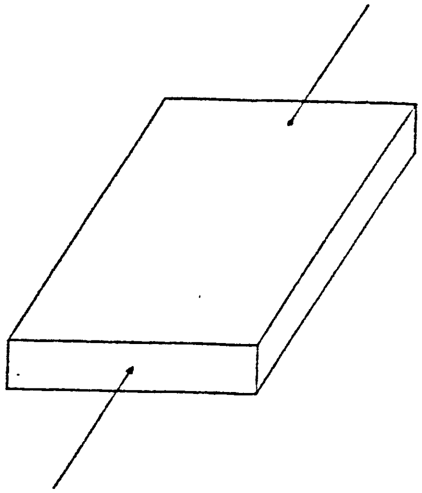

FIGURE E.2 Stressed Block

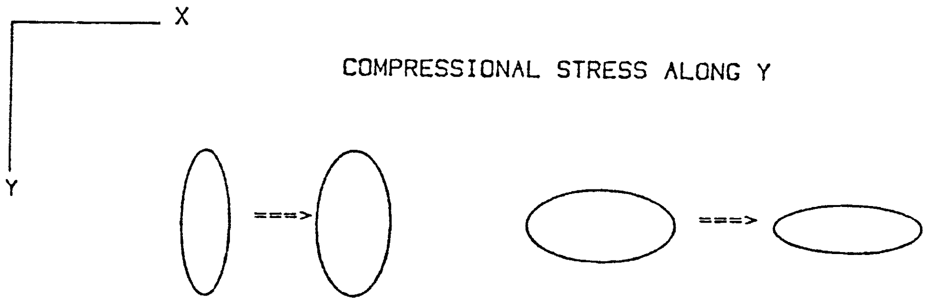

FIGURE E.3 Crack Response to Stress

electrical properties are crack controlled Madden(1978), the conductivity in the Y direction will increase while the conductivity in the X direction will decrease. The conductance tensor for an initially isotropic block then takes the form:

$$\underline{\underline{\sigma}} = \begin{bmatrix} \sigma + \delta\sigma_{\perp} & 0 \\ 0 & \sigma + \delta\sigma_{//} \end{bmatrix} \tag{E-11}$$

Similarly, for a tensile change in stress along Y, cracks along X will tend to open and cracks along Y will tend to close.

Figure E.3 represents the simple case of a single homogeneous block subjected to a compressive change in stress. In general, each block is heterogeneous and the axis of maximum change in stress is not aligned with the principal axis of the block conductivity tensor. To find the stress perturbed conductance for a heterogeneous block, first we find the sub block conductance tensors oriented along the maximum change in stress direction; we rotate these tensors to directions perpendicular and parallel to the sub block interface; combine the sub block conductances with the condition of current continuity; and, finally, we rotate the combined tensor to the X and Y directions. With this procedure. then. we can establish the effects of stress induced changes at the sub block level on the conductance tensor of the full block, our minimum computational scale. At the regional level. we follow the same procedure for the individual blocks but have no further need to combine the block tensors to accomodate the scale requirements of the thin sheet program.

As an illustration. let us consider now a heterogeneous block subjected to a stress perturbation directed at an angle of 45 degrees to the sub block contact as shown in Figure E.4.

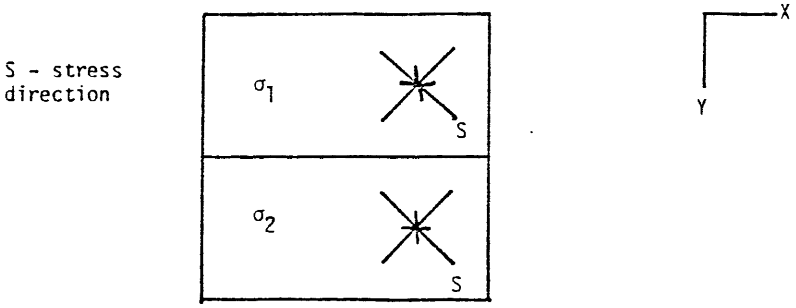

Figure E.4 Sub Block Stress

In both sub blocks we find the perturbed conductivities perpendicular and parallel to the maximum stress direction such that:

$$\begin{aligned} \sigma_{\perp i} &= \sigma_i + \delta\sigma_{\perp i} \\ \sigma_{\parallel i} &= \sigma_i + \delta\sigma_{\parallel i} \end{aligned} \qquad (E-12)$$

Rotating the sub block conductivity tensors to directions parallel and perpendicular to the sub block contact we find:

$$\sigma_{xxi} = \sigma_{yyi} = \frac{\sigma_{\perp i} + \sigma_{/\!/ i}}{2} = \sigma_i + \frac{\delta\sigma_{\perp i} + \delta\sigma_{/\!/ i}}{2} \qquad \text{(E-13)}$$

$$\sigma_{xyi} = \sigma_{yxi} = \frac{\sigma_{\perp i} - \sigma_{/\!/ i}}{2} = \sigma_i + \frac{\delta\sigma_{\perp i} - \delta\sigma_{/\!/ i}}{2}$$

Finally, we apply boundary conditions on the sub blocks with the result:

$$\sigma_{xx} = \frac{\sigma_{xx1} + \sigma_{xx2}}{2} \qquad \sigma_{xy} = \frac{\sigma_{xy1}\sigma_{yy2} + \sigma_{xy2}\sigma_{yy1}}{\sigma_{yy1} + \sigma_{yy2}} = \sigma_{yx}$$

$$\sigma_{yy} = \frac{2\,\sigma_{yy1}\,\sigma_{yy2}}{\sigma_{yy1} + \sigma_{yy2}}$$

(E-14)

The new block conductance tensor equals the old tensor plus a perturbation. The perturbed portion is of the form:

$$\frac{\delta\sigma_{xx}}{\sigma_{xx}} = \frac{\delta\sigma_{xx1} + \delta\sigma_{xx2}}{\sigma_{xx1} + \sigma_{xx2}}$$

$$\frac{\delta\sigma_{yy}}{\sigma_{yy}} = \frac{\delta\sigma_{yy1}}{\sigma_{yy1}} + \frac{\delta\sigma_{yy2}}{\sigma_{yy2}} \qquad (E\text{-}15)$$

$$\frac{\delta\sigma_{xy}}{\sigma_{xy}} = \frac{\delta\sigma_{yx}}{\sigma_{yx}} = \frac{\sigma_{xy1}\,\delta\sigma_{yy2} + \sigma_{yy2}\,\delta\sigma_{xy1} + \sigma_{xy2}\,\delta\sigma_{yy1} + \sigma_{yy1}\,\delta\sigma_{xy2}}{\sigma_{xy1}\,\sigma_{yy2} + \sigma_{xy2}\,\sigma_{yy1}}$$

Thus, we have a simple procedure for calculating the perturbation of the conductance of crustal blocks subjected to a homogeneous deformation.

BIOGRAPHY

The author was born in Boston on July 13, 1942 and attended Boston public schools graduating from Boston Latin School in 1960. He attended Northeastern University in Boston graduating in 1965. In 1961 he started as a student technician at the Instrumentation Laboratory at MIT and remained as an engineer after graduation. Between 1969 and 1974, he worked for Prof. Simmons of the Dept. of Earth and Planetary Sciences. In 1972 he obtained a Masters degree in Aeronautics and Astronautics at MIT and became interested in Geophysics enrolling in the Dept. of Earth and Planetary Sciences in 1975. After defending his thesis, he will commence work with Chevron Oil Field Research Co. in La Habra, California.